THE GEOLOGICAL SOCIETY OF AMERICA®

THEMED ISSUE: Reporting and Interpretation of Geochronologic Data

Interpreting and reporting $^{40}Ar/^{39}Ar$ geochronologic data

Allen J. Schaen[1,†], Brian R. Jicha[1], Kip V. Hodges[2], Pieter Vermeesch[3], Mark E. Stelten[4], Cameron M. Mercer[5], David Phillips[6], Tiffany A. Rivera[7], Fred Jourdan[8], Erin L. Matchan[6], Sidney R. Hemming[9], Leah E. Morgan[10], Simon P. Kelley[11], William S. Cassata[12], Matt T. Heizler[13], Paulo M. Vasconcelos[14], Jeff A. Benowitz[15], Anthony A.P. Koppers[16], Darren F. Mark[17,18], Elizabeth M. Niespolo[19,20], Courtney J. Sprain[21], Willis E. Hames[22], Klaudia F. Kuiper[23], Brent D. Turrin[24], Paul R. Renne[18,19], Jake Ross[13], Sebastien Nomade[25], Hervé Guillou[25], Laura E. Webb[26], Barbara A. Cohen[5], Andrew T. Calvert[4], Nancy Joyce[27], Morgan Ganerød[28], Jan Wijbrans[23], Osamu Ishizuka[29,30], Huaiyu He[31], Adán Ramirez[32], Jörg A. Pfänder[33], Margarita Lopez-Martínez[34], Huaning Qiu[35], and Brad S. Singer[1]

[1]*Department of Geoscience, University of Wisconsin–Madison, Madison, Wisconsin 53706, USA*
[2]*School of Earth and Space Exploration, Arizona State University, Tempe, Arizona 85287, USA*
[3]*Department of Earth Science, University College London, London WC1E 6BT, UK*
[4]*U.S. Geological Survey, 345 Middlefield Road, Menlo Park, California 94025, USA*
[5]*Solar System Exploration Division, National Aeronautics and Space Administration (NASA) Goddard Space Flight Center, Greenbelt, Maryland 20771, USA*
[6]*School of Earth Sciences, The University of Melbourne, Parkville, VIC 3010, Australia*
[7]*Department of Geology, Westminster College, Salt Lake City, Utah 84105, USA*
[8]*Western Australian Argon Isotope Facility, John de Laeter Centre & Applied Geology, Curtin University, Perth, WA 6845, Australia*
[9]*Lamont-Doherty Earth Observatory, Columbia University, Palisades, New York 10964, USA*
[10]*U.S. Geological Survey, Denver Federal Center, MS 963, Denver, Colorado 80225, USA*
[11]*School of Geosciences, University of Edinburgh, Edinburgh EH8 9XP, UK*
[12]*Nuclear & Chemical Sciences Division, Lawrence Livermore National Laboratory, Livermore, California 94550, USA*
[13]*New Mexico Bureau of Geology and Mineral Resources, New Mexico Tech, Socorro, New Mexico 87801, USA*
[14]*School of Earth and Environmental Sciences, The University of Queensland, Brisbane, QLD 4072, Australia*
[15]*Geophysical Institute and Geochronology Laboratory, University of Alaska–Fairbanks, Fairbanks, Alaska 99775, USA*
[16]*College of Earth, Ocean, and Atmospheric Science, Oregon State University, Corvallis, Oregon 97331, USA*
[17]*Isotope Geoscience Unit, Scottish Universities Environmental Research Centre (SUERC), East Kilbride G75 0QF, UK*
[18]*Department of Earth & Environmental Science, University of St. Andrews, St. Andrews KY16 9AJ, UK*
[19]*Berkeley Geochronology Center (BGC), 2455 Ridge Road, Berkeley, California 94709, USA*
[20]*Department of Earth and Planetary Science, University of California, Berkeley, California 94720, USA*
[21]*Department of Geological Sciences, University of Florida, Gainesville, Florida 32611, USA*
[22]*Department of Geosciences, Auburn University, Auburn, Alabama 36849, USA*
[23]*Faculty of Earth and Life Sciences, VU University Amsterdam, De Boelelaan 1085, 1081HV, Amsterdam, The Netherlands*
[24]*Wright-Rieman Labs, Department of Earth and Planetary Sciences, Rutgers—State University of New Jersey, Piscataway, New Jersey 08854, USA*
[25]*Laboratoire des Sciences du Climat et de l'Environnement (LSCE), Institut Pierre Simon Laplace (IPSL), UMR8212, Commissariat à l'Énergie Atomique (CEA)–Centre National de la Recherche Scientifique (CNRS)–University of Versailles Saint-Quentin-en-Yvelines (UVSQ), and Sciences de la Planète et de l'Univers (SPU), Université Paris-Saclay, 91190 Gif-Sur-Yvette, France*
[26]*Department of Geology, University of Vermont, Burlington, Vermont 05401, USA*
[27]*Geological Survey of Canada, 601 Booth Street, Ottawa, Ontario K1A 0E8, Canada*
[28]*Geological Survey of Norway, Leiv Erikssonsvei 39, 7040 Trondheim, Norway*
[29]*Geological Survey of Japan, National Institute of Advanced Industrial Science and Technology (AIST), Ibaraki 305-8567, Japan*
[30]*Japan Agency for Marine-Earth Science and Technology, Yokosuka, Kanagawa 237-0061, Japan*
[31]*College of Earth Sciences, Chinese Academy of Sciences, Beijing 100029, China*
[32]*SERNAGEOMIN Servicio National de Geología y Minería, Anexo 3101, Til Til 1993, Nunoa, Santiago, Chile*
[33]*Institut für Geologie, Technische Universität Freiberg, Gustav-Zeuner-Strasse 12, 09599 Freiberg, Germany*
[34]*Departamento de Geología, Centro de Investigación Científica y de Educación Superior de Ensenada (CICESE), Carretera Ensenada-Tijuana No. 3918, Ensenada 22860, Baja California, Mexico*
[35]*Key Laboratory of Tectonics and Petroleum Resources, China University of Geosciences, Ministry of Education, Wuhan 430074, China*

[†]Present address: Department of Geosciences, University of Arizona, Tucson, Arizona 85716, USA; ajschaen@arizona.edu.

GSA Bulletin; https://doi.org/10.1130/B35560.1; 11 figures; 5 tables; 1 supplemental file.

ABSTRACT

The $^{40}Ar/^{39}Ar$ dating method is among the most versatile of geochronometers, having the potential to date a broad variety of K-bearing materials spanning from the time of Earth's formation into the historical realm. Measurements using modern noble-gas mass spectrometers are now producing $^{40}Ar/^{39}Ar$ dates with analytical uncertainties of ~0.1%, thereby providing precise time constraints for a wide range of geologic and extraterrestrial processes. Analyses of increasingly smaller subsamples have revealed age dispersion in many materials, including some minerals used as neutron fluence monitors. Accordingly, interpretive strategies are evolving to address observed dispersion in dates from a single sample. Moreover, inferring a geologically meaningful "age" from a measured "date" or set of dates is dependent on the geological problem being addressed and the salient assumptions associated with each set of data. We highlight requirements for collateral information that will better constrain the interpretation of $^{40}Ar/^{39}Ar$ data sets, including those associated with single-crystal fusion analyses, incremental heating experiments, and in situ analyses of microsampled domains. To ensure the utility and viability of published results, we emphasize previous recommendations for reporting $^{40}Ar/^{39}Ar$ data and the related essential metadata, with the amendment that data conform to evolving standards of being findable, accessible, interoperable, and reusable (FAIR) by both humans and computers. Our examples provide guidance for the presentation and interpretation of $^{40}Ar/^{39}Ar$ dates to maximize their interdisciplinary usage, reproducibility, and longevity.

INTRODUCTION

Since 2003, the international EARTHTIME Initiative (www.earth-time.org) has focused on enhancing the precision and accuracy of commonly used geochronologic methods, which has resulted in community-wide improvements in metrologic traceability, interlaboratory reproducibility, precision, accuracy, and intercalibration between the $^{40}Ar/^{39}Ar$ method and other dating methods (e.g., U-Pb zircon ages, astronomical time scale). These advances have enabled the expansion of opportunities for $^{40}Ar/^{39}Ar$ dating to provide useful constraints for many geologic processes spanning a wide range of time periods. However, the level of analytical uncertainty (~0.1%) for dates obtained from a new generation of mass spectrometers—as well as the high spatial resolution afforded by excimer laser microsampling techniques—has led to increasingly dispersed data sets for individual minerals or hand samples, including fluence monitors (Phillips and Matchan, 2013; Mercer et al., 2015; Rivera et al., 2016; Andersen et al., 2017; Yancey et al., 2018). Identification of this complexity, in turn, demands a deeper consideration of the processes (e.g., geologic, analytical, reactor-induced) responsible. Here, we provide example $^{40}Ar/^{39}Ar$ interpretations from a variety of geologic environments and rock types to illustrate possible complexities to nonspecialists. We bolster previous recommendations for minimum reporting requirements for $^{40}Ar/^{39}Ar$ metadata (Renne et al., 2009), along with added criteria, including the requirement that metadata files are made machine-readable to facilitate automated archiving and interdisciplinary usage of data.

$^{40}Ar/^{39}Ar$ GEOCHRONOLOGY OVERVIEW

The $^{40}Ar/^{39}Ar$ dating method is a variant of conventional K-Ar geochronology (Merrihue and Turner, 1966), whereby the radioactive parent isotope ^{40}K ($t_{1/2} \approx 1.25$ Ga) undergoes branched decay to two stable daughter products, ^{40}Ca (~89%) and ^{40}Ar (~11%), via beta emission and electron capture, respectively (Beckinsale and Gale, 1969; Steiger and Jäger, 1977; Min et al., 2000). The decay branch of interest for $^{40}Ar/^{39}Ar$ geochronology is the production of stable radiogenic Ar ($^{40}Ar^*$). $^{40}Ar^*$ can be measured in K-bearing materials with ages that range from historical to beyond the Archean. K-Ar geochronology is a first-order dating technique that relies on the quantitative isotopic analysis of separate sample aliquots for potassium and argon using different instruments/techniques. Potassium analyses (assuming a constant $^{40}K/^{39}K$ ratio of 0.01167; Garner et al., 1975) are conducted by flame photometry, X-ray fluorescence (XRF), or isotope dilution, whereas Ar analyses are performed by isotope-dilution noble-gas mass spectrometry. Comparatively, the $^{40}Ar/^{39}Ar$ dating technique is a relative geochronometer that requires the neutron irradiation of samples along with a "known age" fluence monitor. Typically, the five isotopes of argon (^{40}Ar, ^{39}Ar, ^{38}Ar, ^{37}Ar, and ^{36}Ar) are measured by noble-gas mass spectrometry (for a more detailed discussion, see Dalyrmple et al., 1981; McDougall and Harrison, 1999; Kelley, 2002; Reiners et al., 2018). The data produced by the $^{40}Ar/^{39}Ar$ method can then be evaluated using the age-spectrum plot, isotope correlation diagrams, Ar diffusion using Arrhenius plots of the Ar isotopes, and direct observation of possible intracrystalline variations in $^{40}Ar^*$ through laser-ablation microprobe mapping.

$^{40}Ar/^{39}Ar$ dates commonly represent the time since a sample last became closed to isotope exchange of ^{40}K and ^{40}Ar loss, be it due to crystallization, retrogression, alteration, deformation, or thermal diffusion. In rapidly cooled, unaltered volcanic rocks, $^{40}Ar/^{39}Ar$ dates are commonly interpreted as the eruption age. In metamorphosed, metasomatized, or retrogressed samples, they often represent the age of reaction in a chemically open system. For samples precipitated from sedimentary or weathering solutions, $^{40}Ar/^{39}Ar$ dates record the ages of low-temperature chemical reactions. In samples that preserve petrologic equilibrium achieved at high temperatures, the $^{40}Ar/^{39}Ar$ dates reflect cessation of thermally induced diffusion as the sample cooled. The validity of the closed system of a sample is typically evaluated by conducting an incremental heating experiment, whereby Ar is degassed in a stepwise fashion from low to higher temperatures. The subsequent $^{40}Ar/^{39}Ar$ dates from each step are then plotted on an age spectrum diagram, which allows for the statistical evaluation of concordance, known as an age plateau. An alternative approach to step heating is total fusion of single minerals, for which individual $^{40}Ar/^{39}Ar$ dates are then compiled to determine a potentially meaningful geologic age. These are model ages because a common assumption in the interpretation of $^{40}Ar/^{39}Ar$ dates as eruption or crystallization ages for terrestrial samples is that the trapped or "initial" Ar has an atmospheric composition ($^{40}Ar/^{36}Ar$ ratio of ~300; Nier, 1950; Lee et al., 2006; Renne et al., 2009; Valkiers et al., 2010; Mark et al., 2011), and that samples have retained all $^{40}Ar^*$ derived from in situ ^{40}K radioactive decay. These assumptions must be tested for each sample, because: (1) $^{40}Ar^*$ may diffuse out of crystal structures during cooling or prograde reheating events; (2) K and $^{40}Ar^*$ can be removed or added from glasses or minerals by aqueous alteration or metasomatism (e.g., weathering; Cerling et al., 1985); and (3) nonradiogenic ^{40}Ar may be incorporated into minerals and glasses during their formation (i.e., trapped Ar). Trapped Ar with $^{40}Ar/^{36}Ar$ greater than the modern atmospheric composition is termed "extraneous Ar" (e.g., Lanphere and Dalrymple, 1976) and may be sequestered in melt or fluid inclusions from the mantle, magmas, or deep crustal fluids. However, even if it is nonatmospheric, the initial $^{40}Ar/^{36}Ar$ ratio of a sample may be evaluated by the isochron method. For example, plutonic and volcanic rocks may (1) contain inherited Ar in antecrysts (e.g., Andersen et al., 2017) or xenocrysts (e.g., Chen et al., 1996; Singer et al., 1998; Renne et al., 2012), which reflect the pre-eruptive/pre-intrusive history of radioisotopic decay, and (2)

have incorporated trapped Ar with a $^{40}Ar/^{36}Ar$ ratio lower than the current atmospheric ratio due to kinetic fractionation upon emplacement (Matsumoto and Kobayashi, 1995; Renne et al., 2009; Morgan et al., 2009). The power of the $^{40}Ar/^{39}Ar$ method lies in the ability to evaluate all assumptions within the context of a sample's geologic history and to identify nonideal behavior (K and Ar gain or loss) by identifying the carrier phases of Ar by their Cl/Ca/K signatures (e.g., Kelley and Turner, 1991).

The $^{40}Ar/^{39}Ar$ method involves placing K-bearing samples in a nuclear reactor for irradiation with thermal and fast neutrons, where nucleogenic ^{39}Ar ($^{39}Ar_K$; $t_{1/2} = 269$ yr) is produced from ^{39}K, ^{37}Ar is produced from Ca, and ^{38}Ar is produced from Cl (Merrihue and Turner, 1966). The neutron flux is quantified by co-irradiating fluence monitors of known age with the samples (Merrihue and Turner, 1966), defining the irradiation parameter J (i.e., the production factor of ^{39}Ar from ^{39}K). After irradiation, the samples and associated fluence monitors are loaded into an ultrahigh-vacuum system, where gases (including Ar) are extracted from the sample using furnace, laser, or crushing techniques, some of which are discussed below. After extraction, the gases are purified to remove reactive species (e.g., H_2O, CO_2, Cl) using a combination of cold traps and/or getter pumps. The remaining gases, including argon and other noble gases, are introduced into a static gas-source mass spectrometer for isotopic analysis.

Acquisition of $^{40}Ar/^{39}Ar$ data is time- and labor-intensive, with the main time-limiting step being the irradiation process (2–6 mo; Fig. 1), which depends on the irradiation duration as well as the reactor queue (Fig. 1). For a comprehensive list of commonly used nuclear reactors, see table 3-3 (p. 56) of McDougall and Harrison (1999). The optimal duration of the irradiation process is determined by the neutron flux, which is related to reactor power, proximity to the reactor core, and local shielding, as well as the age of the samples, where longer irradiations are required for older samples to achieve optimal $^{40}Ar^*/^{39}Ar$ ratios (typically 1–10; Fig. 1).

ANALYTICAL ADVANCES

Until the 1990s, the most widely used approach to extracting Ar from silicate samples for dating involved incremental heating or total fusion of samples in vacuo using a double-vacuum resistance furnace, followed by the separation of reactive species from the evolved gases using zirconium metal-alloy getter pumps and/or cryogenic devices prior to analysis. The gas purification techniques for $^{40}Ar/^{39}Ar$ analytical systems have changed little over the years, but both the gas extraction and mass spectrometry subsystems have advanced substantially.

Laser Technologies

Lasers have been used to extract gases from samples for $^{40}Ar/^{39}Ar$ analyses since the 1970s (e.g., Megrue, 1973; York et al., 1981), but they were not widely used until the late 1980s and early 1990s. The variety of lasers used has evolved to address the needs of several distinct Ar extraction techniques. Pulsed lasers (micro- to nanosecond pulses) are typically used for spot analysis, whereas continuous lasers dominate heating and fusion of samples over several seconds to minutes. The range of wavelengths utilizes the variation in laser/sample interaction and variations of absorption with wavelength. The various lasers include: (1) CO_2 lasers, which produce energy in the infrared spectrum at a wavelength of 10.6 µm; (2) infrared Nd:YAG lasers (1.06 µm); (3) infrared diode lasers (typically between 800 nm and 1.0 µm); (4) Ar and visible diode lasers (typically around 530 nm); (5) ultraviolet, frequency-quadrupled (266 nm) or quintupled (213 nm) Nd:YAG lasers; and (6) ultraviolet KrF (248 nm) and ArF excimer lasers (193 nm). The use of lasers producing energy across such a broad segment of the electromagnetic spectrum relates to the different light-matter interactions for specific types of analyses.

Of all the lasers used in $^{40}Ar/^{39}Ar$ laboratories, CO_2 lasers are the most versatile, due to the high absorption of 10.6 µm energy by all miner-

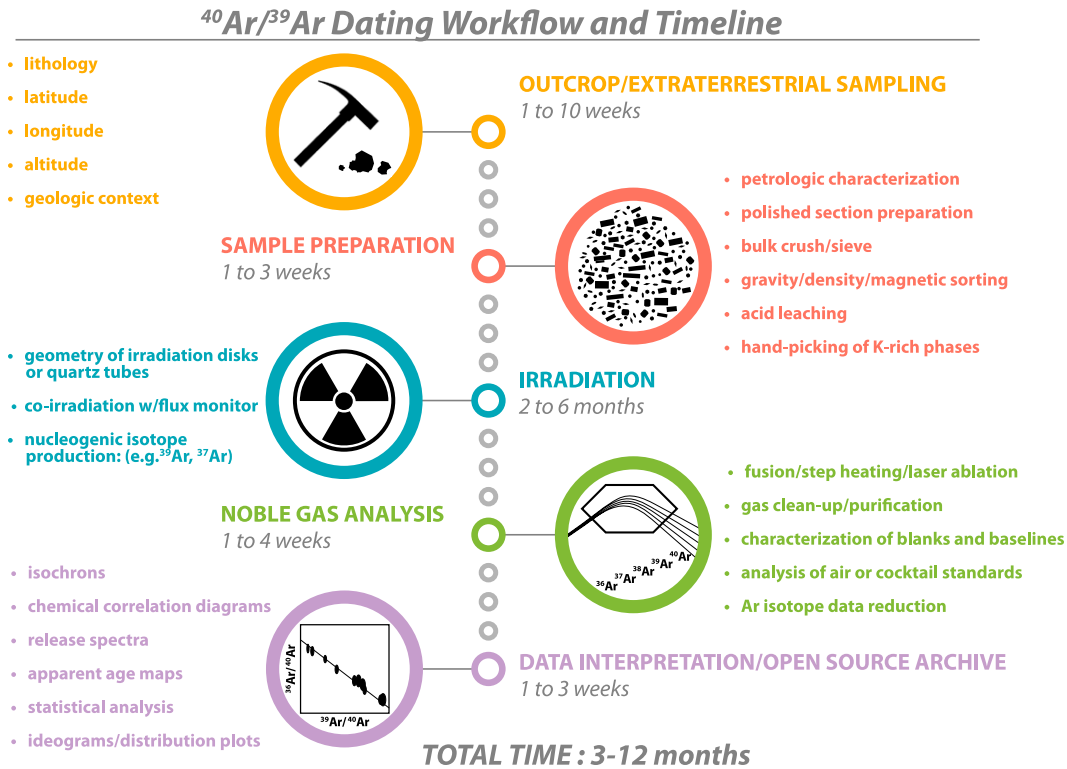

Figure 1. Summary of steps required to complete an $^{40}Ar/^{39}Ar$ analysis with selected metadata and considerations associated with each stage. Duration of each step is estimated and varies based on number of samples, sample quality, reactor turnaround time, and machine time.

als and glasses of interest. However, minimum focused beam diameters for CO_2 beams are relatively large compared to other commonly available lasers (minimum diameters attainable are generally 5–10 times the laser wavelength). As a consequence, they are typically used for incremental heating or total fusion experiments.

The energy of other infrared lasers (the 1064 nm Nd:YAG and various diode lasers) is much less effectively absorbed by transparent to subtransparent minerals, including muscovite and feldspar, which may require micro-encapsulation in a metal such as niobium (e.g., Jourdan et al., 2014). Both 1064 nm Nd:YAG lasers and infrared diode lasers are typically used to extract Ar at lower irradiances by heating or melting by expanding the beam focal point or lowering the laser power.

For very high-spatial-resolution studies of individual mineral grains or for in situ targeting, ultraviolet lasers are preferred (e.g., Kelley et al., 1994). The growing availability of ArF excimer lasers in $^{40}Ar/^{39}Ar$ laboratories has spawned great interest in microanalytical studies of rock thin sections and mineral grain mounts using ultraviolet laser-ablation microprobes (UVLAMPs). In particular, the near-complete absorption of 193 nm energy by almost all minerals of interest and the high energy and short pulse duration of ArF excimers result in extremely well-formed ablation pits, minimal redeposition of ablated material, full extraction of gases of interest from the ablated material, and minimal heating of the surrounding sample (Gunther et al., 1997; van Soest et al., 2011). The limiting factor for the optimum size of the laser pit is the necessity to detect the five Ar isotopes and measure their concentrations with a precision deemed sufficient for the intended purpose. UVLAMP technology has been used to constrain ^{40}Ar exchange by diffusion and alteration in natural samples (Pickles et al., 1997; Kelley and Wartho, 2000; Smith et al., 2005), the role of deformation and recrystallization in ^{40}Ar loss (Cosca et al., 2011; Mulch and Cosca, 2004; Mulch et al., 2002), as well as the ages of multiple fabric-forming events in polymetamorphic tectonites (Chan et al., 2000; Janak et al., 2001; Mulch et al., 2005), pseudotachylytes in fault zones (Condon et al., 2006; Cosca et al., 2005; Fornash et al., 2016; Muller et al., 2002), authigenic K-feldspar growth in sedimentary rocks (Sherlock et al., 2005), and multiple impact-melting events in lunar breccias (Mercer et al., 2015, 2019).

Gas Extraction and Purification Techniques

Most $^{40}Ar/^{39}Ar$ data currently produced involve the extraction of gases from single crystals or whole-rock/groundmass aliquots. Some laboratories focus only on the evolving Ar isotopic characteristics during incremental heating when interpreting the geologic significance of dates, and they extract gas stepwise by applying progressively higher laser powers for each increment, using power level as a rough proxy for sample temperature. A more quantitative approach, especially for thermochronologic or diffusion-based studies, is to use a well-calibrated optical pyrometer and use the laser to heat a sample that is encapsulated in a nonreactive (e.g., platinum or tantalum) metal jacket in order to obtain a robust estimation of the temperature (e.g., Jourdan, 2014).

Once the gas is extracted from the sample, it is purified by a Ti sublimation pump or by a series of nonevaporable getters. Getter pumps use high field strength element (e.g., titanium, zirconium, vanadium) alloys to remove active gases, like O_2, H_2, and N_2, and break down hydrocarbon volatiles while not reacting with noble gases such as Ar. Trapping of water and carbon dioxide is often accomplished using a cryogenic trap or cold finger operated at a temperature slightly above the freezing point of Ar (83.8 K). The introduction of "clean" gas into the mass spectrometer is key to (1) ionization efficiency, (2) avoiding measurement of argon plus isobarically interfering species, and (3) preventing "memory" effects in the mass spectrometer/extraction system, all of which could lead to an inaccurate $^{40}Ar/^{39}Ar$ date.

Modern Magnetic Sector Mass Spectrometry

$^{40}Ar/^{39}Ar$ measurements depend on magnetic sector mass spectrometers to determine isotopic abundances. Commercially available mass spectrometers today are ubiquitously the multicollector type but are quite diverse in other respects. Multicollector analysis allows for significantly more data to be acquired per unit time than peak-hopping with a single collector but carries the disadvantage of requiring intercalibration of sensitivity and mass bias between detectors. Some multicollector instruments have greater mass resolution compared to older mass spectrometers, whereas others offer improved sensitivity or the ability to measure very small signals. By far the most significant development associated with the newer instruments is the more stable electronics, which translates to less noise and improved ion beam and amplifier stability during analysis. This technological improvement, along with the reduction of blanks and isobaric interferences ($H^{35}Cl$ and $3{\cdot}^{12}C$), has led to more precise dates and is expanding the applicability of the already versatile $^{40}Ar/^{39}Ar$ chronometer (Fig. 2). In addition, the rapid multicollection of Ar isotopes has resulted in shorter data acquisition times per analysis, thereby increasing sample throughput in laboratories.

The use of lasers for sample heating coupled with the development of low-volume gas extraction lines has, in most cases, resulted in a drastic reduction in the amount of sample required for analysis. Previously, incremental heating experiments of Pliocene–Pleistocene lavas consisted of a small number of steps (average 8–12) and required several hundred milligrams of sample (e.g., Singer and Pringle, 1996). Now, these experiments can be conducted on as little as 10–30 mg of sample (e.g., Singer et al., 2019), and they can be broken up into many more incremental heating steps (Fig. 2). Moreover, analyses of low-K phases such as latest Pleistocene plagioclase phenocrysts (e.g., Carrasco-Nuñez et al., 2018) and Cenozoic pyroxene (e.g., Ware and Jourdan, 2018; Konrad et al., 2019) are now feasible. Higher precision on smaller and younger detrital grains is improving our understanding of progressive, grain size–specific detrital signal dilution in rivers, and our ability to provide robust provenance signals obtained for sediments located many hundreds of kilometers away from their source rocks (e.g., Blewett et al., 2019; Gemignani et al., 2019; Hereford et al., 2016).

DATA REPORTING

To compute an $^{40}Ar/^{39}Ar$ date for a sample of unknown age, the following parameters and their estimated uncertainties are required:

(1) the corrected relative abundances of Ar isotopes measured for the unknown (see "Data Corrections and Factors Contributing to Uncertainties" section later herein);
(2) the corrected relative abundances of Ar isotopes measured for a co-irradiated fluence monitor used to calculate a *J* value;
(3) the assumed age, or the $^{40}Ar^*/^{40}K$ ratio of the co-irradiated fluence monitor; and
(4) the values of the ^{40}K decay constants (Table 1).

While the first two data items are measured experimentally during each $^{40}Ar/^{39}Ar$ study, the latter two are typically based on the results of dedicated studies published in the literature. Items 2, 3, and 4 are used to compute the irradiation parameter *J*, which is then combined with items 1 and 4 to compute a date for a sample of unknown age. As the $^{40}Ar/^{39}Ar$ geochronology technique has evolved, so too has documentation of heterogeneities in the chemical composition of irradiation monitor minerals and their atmospheric-corrected $^{40}Ar^*/^{40}K$ or apparent ages, along with variation of the estimates of the ^{40}K decay constants. In other words, the monitor ages and decay constant values used in $^{40}Ar/^{39}Ar$ studies may differ amongst publications from different times

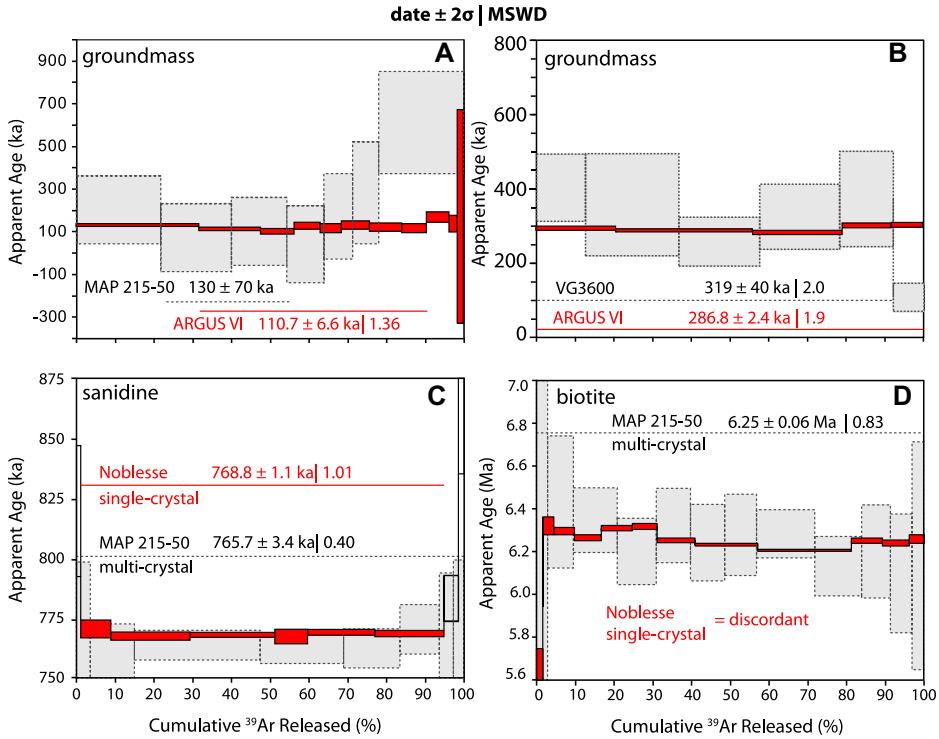

Figure 2. Comparison of $^{40}Ar/^{39}Ar$ incremental heating experiments on the same material using either a single-collector (MAP 215-50, VG3600) or multicollector (ARGUS VI, Noblesse) noble-gas mass spectrometer. (A) Groundmass from lava at Trinchera Pass, New Mexico (Zimmerer, 2019). (B) Basaltic groundmass (sample V21c) from Mount Rouse volcano, NE Australia (Matchan and Phillips, 2011, 2014). (C) Single-crystal sanidine experiment using multicollection from the Bishop tuff (Andersen et al., 2017) vs. multicrystal, single-collector experiment (Mark, 2017). (D) Concordant multicrystal single-collector experiment of biotite from the Risco-Bayo Huemul plutonic complex (Schaen et al., 2017, 2018) masks discordance observed in more precise single-crystal data obtained via multicollection. Ages are reported with 2σ analytical uncertainty followed by the mean square of weighted deviates (MSWD).

TABLE 1. ^{40}K DECAY CONSTANTS

Constant	Steiger and Jäger (1977)	Min et al. (2000)	Renne et al. (2011)
λ_{EC}	0.581×10^{-10} yr^{-1}	$0.580 \pm 0.007 \times 10^{-10}$ yr^{-1}	$0.5757 \pm 0.016 \times 10^{-10}$ yr^{-1}
λ_{β^-}	4.962×10^{-10} yr^{-1}	$4.884 \pm 0.049 \times 10^{-10}$ yr^{-1}	$4.9548 \pm 0.0134 \times 10^{-10}$ yr^{-1}
λ_{Total}	5.543×10^{-10} yr^{-1}	$5.463 \pm 0.107 \times 10^{-10}$ yr^{-1}	$5.531 \pm 0.0135 \times 10^{-10}$ yr^{-1}

Note: λ_{EC} = decay due to electron capture, λ_{β^-} = decay due to beta emission.

TABLE 2. INTERCALIBRATION FACTORS (*R*) BETWEEN ALDER CREEK (AC) AND FISH CANYON (FC) SANIDINE STANDARDS THAT INCLUDE DATA FROM MULTICOLLECTOR MASS SPECTROMETERS

Reference	$R^{ACs}_{FCs} \pm 2\sigma$
Coble et al. (2011)	0.041805 ± 0.000420
Rivera et al. (2013)	0.041754 ± 0.000030
Phillips and Matchan (2013)	0.041686 ± 0.000049
Jicha et al. (2016)	0.041760 ± 0.000047
Niespolo et al. (2017)	0.041702 ± 0.000028
Phillips et al. (2017)	0.041692 ± 0.000026
Fleck et al. (2019)	0.041714 ± 0.000170
Weighted mean:	**0.041715 ± 0.000029 (0.069%) MSWD = 2.7**

Note: $R^{ACs}_{FCs} = (e^{\lambda ACs} - 1)/(e^{\lambda FCs} - 1)$, where ACs—Alder Creek sanidine and FCs—Fish Canyon sanidine. R^{ACs}_{FCs} of Phillips et al. (2017) in Table 2 is different than was reported due to a calculation error in the original publication (Phillips et al., 2020). MSWD—mean square of weighted deviates.

and/or laboratory groups. Therefore, when comparing different $^{40}Ar/^{39}Ar$ data sets, it is important that researchers account for these differences. It is also critical to understand the intercalibration histories of the monitor minerals and the set of ^{40}K decay constants used (Tables 1, 2, and 3).

Fluence Monitors and Decay Constants

The ages or $^{40}Ar^*/^{40}K$ ratios of the fluence monitor minerals are generally determined by: (1) the K-Ar method, (2) intercalibration with one or more different co-irradiated mineral fluence monitors, the age(s) of which has(have) been determined independently (e.g., Alexander and Davis, 1974; Renne et al., 1998), or (3) evaluation against astronomically dated cyclical sedimentary sequences (e.g., Kuiper et al., 2008). It is relatively straightforward to recompute the monitor mineral age to accommodate different or updated ^{40}K decay constants and/or relative K isotope abundances (e.g., Dalrymple, 1979; Min et al., 2000; Mercer and Hodges, 2016). Changes to these parameters (e.g., age, $^{40}Ar^*/^{40}K$, decay constants, etc.) for the selected fluence monitor (and any intermediate-derived fluence monitors) will compound nonlinearly to affect the calibration of a given monitor mineral.

The decay constants of long-lived radioactive nuclides have generally been determined by: (1) directly counting the emission of α, β, and γ particles produced by the decay of a known quantity of a radioactive nuclide, (2) measuring the radiogenic ingrowth of daughter products that accumulate from the decay of a well-known quantity of a radioactive nuclide over a prolonged time period (e.g., decades), and (3) intercalibration of multiple mineral isotopic chronometers (where the well-known decay constant for ^{238}U is commonly taken as the "gold standard") in a rock that formed "instantaneously" and lacks evidence of any secondary processes (Begemann et al., 2001). The exact nature of the branched decay of ^{40}K into ^{40}Ar and ^{40}Ca has been debated due to numerous natural and experimental challenges associated with the use of the above approaches to determine the total decay constant, λ_{tot}, and the branching ratios (Begemann et al., 2001; Naumenko-Dèzes et al., 2017). As our understanding of the ^{40}K decay constants continues to evolve, researchers using published $^{40}Ar/^{39}Ar$ data sets will need to recalculate both the apparent ages of common monitor minerals (if the $^{40}Ar^*/^{40}K$ ratios of the monitors were not reported) and the apparent ages of unknowns as newer values are adopted by the geochronology community. The ^{40}K decay constants and $^{40}Ar^*/^{40}K$ ratio reported by Renne et al. (2010, 2011) for the Fish Canyon sanidine (FCs) monitor mineral were determined using data sets that depended

TABLE 3. AGES FOR COMMONLY UTILIZED $^{40}Ar/^{39}Ar$ FLUENCE MONITORS IN THE GEOLOGIC TIME SCALE (GTS2020; GRADSTEIN ET AL., 2020)

Standard name	Mineral	Apparent age (Ma ± 2σ)	References
ACs	Sanidine	1.1851 ± 0.0004	This paper (from Table 2 *R*-value mean)
FCs/FCT-3	Sandine/biotite	28.201 ± 0.046	Kuiper et al. (2008)
TCs	Sanidine	28.447 ± 0.025	Fleck et al. (2019)
GA-1550	Biotite	99.44 ± 0.17	Jourdan and Renne (2007)
Hb3gr	Hornblende	1081.5 ± 2.4	Jourdan and Renne (2007)

Note: ACs—Alder Creek rhyolite, FCs/FCT-3—Fish Canyon Tuff, and TCs—Taylor Creek rhyolite. All fluence monitor ages here were calculated relative to 28.201 Ma FC sanidine and are shown with 2σ analytical uncertainties. Fluence monitor ages are from Gradstein et al. (2020).

on the ^{238}U decay constant, which requires that error correlations among the parameter values they reported be accounted for when recomputing $^{40}Ar/^{39}Ar$ data sets. Similar care is required for error correlations that arise in the course of other efforts to constrain the ^{40}K decay constants by comparing results from multiple mineral isotopic chronometers.

It is common to encounter $^{40}Ar/^{39}Ar$ dates in the literature calibrated using different ^{40}K decay constants and ages for the same mineral monitors, reflecting the evolution of our knowledge of these parameters (Tables 1, 2, and 3). To compare $^{40}Ar/^{39}Ar$ dates from different studies directly, they must be recalculated to an internally consistent parameter set (decay constant and monitor age). Convenient open-source software tools for straightforward recalibration of published $^{40}Ar/^{39}Ar$ dates include ArArCALIBRATIONS (Koppers, 2002) and the Java-based ArAR (Mercer and Hodges, 2016). In addition to these recalibration tools, other free and open-source software packages like IsoplotR provide user-friendly plotting and statistical analysis of geochronologic data (Vermeesch, 2018). As an example, Figure 3 shows $^{40}Ar/^{39}Ar$ dates published for sanidine from the IrZ-coal layer in the Hell Creek area of NE Montana (Swisher et al., 1993; Renne et al., 2013) and the C-1 melt rock from the Chicxulub impact crater in Yucatán, Mexico (Swisher et al., 1993). The dates of Swisher et al. (1993) were originally reported using a monitor age of 27.84 Ma and the ^{40}K decay constants of Steiger and Jäger (1977), whereas Renne et al. (2013) used the parameter values reported in Renne et al. (2011). Figure 3 shows how these data sets—which represent samples from two of the key deposits used to define the Cretaceous-Paleogene boundary—compare after recalculation to the FCs age recommended by Kuiper et al. (2008) and the ^{40}K decay constants of Min et al. (2000).

While shifts in apparent ages reported by Renne et al. (2013) are within 1σ uncertainties, the shifts in apparent ages reported by Swisher et al. (1993) exceed the stated 1σ uncertainties (Fig. 3). This emphasizes the importance of using an internally consistent set of monitor mineral ages and ^{40}K decay constants when comparing and making interpretations of geologic significance from multiple $^{40}Ar/^{39}Ar$ data sets. In this regard, the geochronology community is actively working to refine knowledge of these critical parameters to improve the overall precision and accuracy that can be achieved with the $^{40}Ar/^{39}Ar$ method.

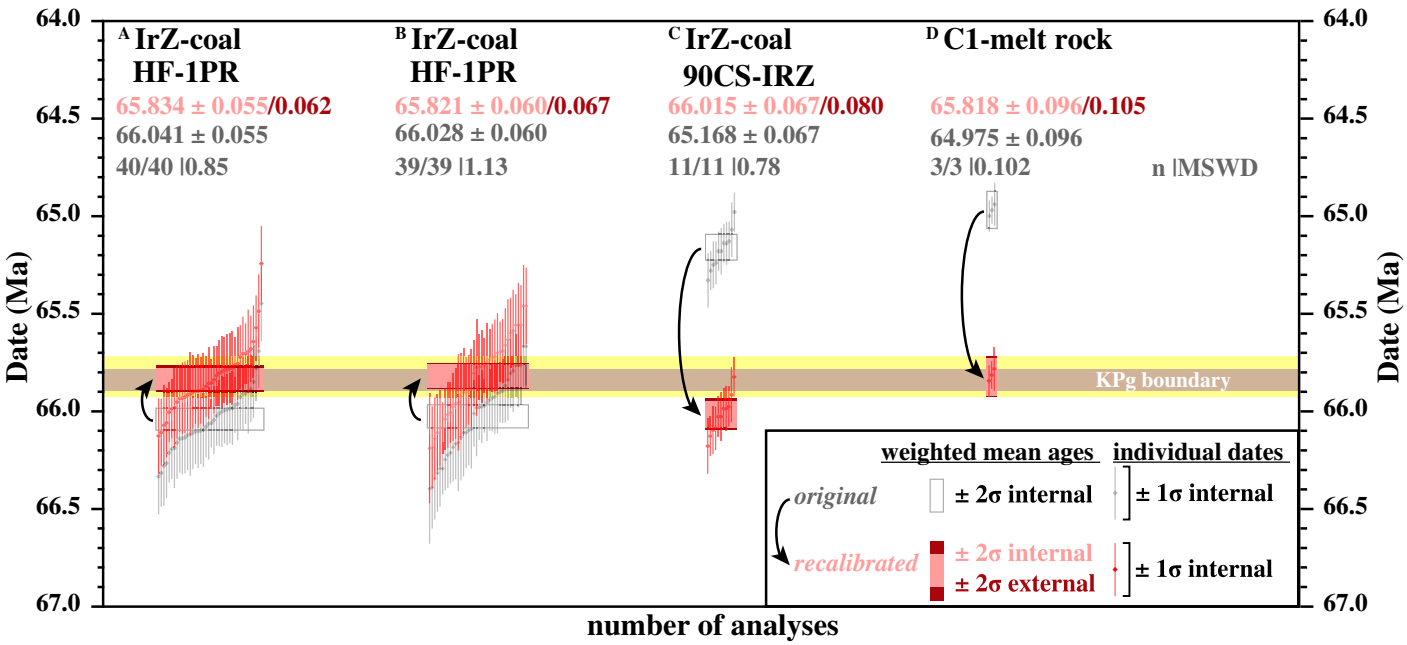

Figure 3. Ranked order summary of $^{40}Ar/^{39}Ar$ dates including single-crystal sanidine fusions from the IrZ-coal layer of the Hell Creek area in NE Montana, United States (Sprain et al., 2018; Renne et al., 2013; Swisher et al., 1993) and incremental heating plateau dates from the C-1 melt rock of the Chicxulub crater in Yucatán, Mexico (Swisher et al., 1992), the latter of which defines the Geologic Time Scale 2012 (GTS2012) Cretaceous-Paleogene boundary (yellow box; Schmitz, 2012). Original data (gray symbols) were calibrated using either the decay constants and Fish Canyon (FC) sanidine monitor age of Renne et al. (2011) (data sets A, B), or the decay constants of Steiger and Jäger (1977) and FC sanidine standard age of 27.84 (Swisher et al., 1992, 1993) (datasets C, D). These original data were recalibrated (red symbols) with the ArAR recalculator software (Mercer and Hodges, 2016) using the decay constants of Min et al. (2000) and the FC sanidine standard age of 28.201 Ma (Kuiper et al., 2008) following the GTS2012. Also displayed is a more recent estimate for the Cretaceous-Paleogene (KPg) boundary of 65.845 ± 0.053 Ma (brown box; Sprain et al., 2018). Dates are reported with 1σ internal uncertainties, weighted means are reported with both 2σ internal and 2σ external uncertainties, and mean square of weighted deviates (MSWD) is shown only for original data.

Required Data and Metadata

For decades, many K-Ar and $^{40}Ar/^{39}Ar$ dates were published without enough supporting metadata, thereby precluding detailed assessment of the dates, recalculation of the data, or recalibration using different monitors or decay constant values. To improve transparency for readers, reviewers, and journal editors and facilitate complete evaluation of dates, Renne et al. (2009) suggested minimum $^{40}Ar/^{39}Ar$ data reporting criteria for publication of $^{40}Ar/^{39}Ar$ dates. The longevity and utility of $^{40}Ar/^{39}Ar$ data sets will be significantly improved by following the recommendations for $^{40}Ar/^{39}Ar$ data reporting first set out by Renne et al. (2009). These reporting norms were acknowledged to be minimum information that would allow recalculations by others, and they were established prior to the implementation of multicollector noble-gas mass spectrometers and modern open data-sharing protocols (see "Announcement: FAIR data in Earth science," Nature, 2019). Data collection for Ar isotopes with multiple detectors requires methods for calibrating the various detectors and therefore involves laboratory-specific instrument procedures, which introduces additional analytical complexity. Here, we expand upon the initial data reporting guidelines of Renne et al. (2009) and suggest additional metadata be reported when publishing $^{40}Ar/^{39}Ar$ data in peer-reviewed journals (Table 4).

Cyberinfrastructure for data archiving and sharing guided by the principles of findability, accessibility, interoperability, and reusability (FAIR; Wilkinson, 2016) has been improved over the last decade. The FAIR ideals are widely agreed upon as beneficial by scientists, but they carry practical challenges and concerns (e.g., maintenance, copyrights, poaching, misuse, time commitments; Nelson, 2009). To avoid the problem of time-consuming and high-impact dates turning into "dark data"—data not carefully indexed, stored, or visible to the outside scientific community that have a strong potential to be lost (Heidorn, 2008)—the future of geochronology is FAIR data that are easily readable by both humans and computers. Full $^{40}Ar/^{39}Ar$ data sets must be published in consistent, well-documented tabular formats (e.g., CSV, XLS) or structured machine-readable formats (e.g., JSON/XML); it is inadvisable to publish these data sets in supplements as a nonstructured PDF file, which greatly inhibit indexing and reuse. For two examples of appropriately formatted $^{40}Ar/^{39}Ar$ metadata files (J. Ross, 2020, personal commun.; Rose and Koppers, 2019) archived via FAIR principles, see the Supplemental Materials.[1] Another alternative to publishing the full suite of $^{40}Ar/^{39}Ar$ metadata in the supplements of papers is to make that data open source and freely available via an online repository (e.g., github.com/NMGRL-Data/KvAges).

[1]Supplemental Material. Fillable PDF checklist of minimum and recommended data to report with $^{40}Ar/^{39}Ar$ dates for author, reviewer, and editor guidance. Two examples (XLS and JSON) of $^{40}Ar/^{39}Ar$ data sets archived via FAIR data principles. Please visit https://doi.org/10.1130/GSAB.S.12302417 to access the supplemental material, and contact editing@geosociety.org with any questions.

TABLE 4. CHECKLIST OF MINIMUM AND RECOMMENDED DATA TO REPORT FOR $^{40}Ar/^{39}Ar$ DATES

Minimum required data (✓)	
☐	Report uncertainties for all parameters (e.g., 95% confidence interval, 1σ, 2σ)
☐	Explicitly state whether uncertainties on ages include decay constant uncertainties
☐	Report sample identifier (ideally unique, e.g., International Geo Sample Number [IGSN])
☐	Report sample location (e.g., latitude, longitude, elevation)
☐	Report sample lithology
☐	Specify material analyzed (e.g., single vs. multicrystal aliquot, weight, phase type)
☐	Report relative isotope abundances† for ^{40}Ar, ^{39}Ar, ^{38}Ar, ^{37}Ar, and ^{36}Ar
☐	Describe step-heating schedule and/or laser power/wattage per analysis
☐	Identify reactor and port used for irradiation (and if Cd shielding or rotation was used)
☐	Describe fluence monitor details (e.g., name, age assumed, reference, calculated *J* value)
☐	Report decay constants used (e.g., ^{40}K, ^{39}Ar, ^{37}Ar, ^{36}Cl), references cited
☐	Identify interfering isotope production ratios (e.g., Ar produced from K, Ca, Cl), references cited
☐	Report ratios used for trapped§ argon correction ($^{40}Ar/^{36}Ar$, $^{40}Ar/^{38}Ar$), reference cited
☐	Indicate time interval used in decay corrections (e.g., days from end of irradiation to start of analysis)
☐	Report proportion radiogenic ^{40}Ar ($\%^{40}Ar^*$)
☐	Provide model age and unit of each analysis (e.g., a, ka, Ma, Ga)
☐	List *F* value ($^{40}Ar^*/^{39}Ar_K$) and its uncertainty
☐	Distinguish which steps are included in the age spectrum/isochron
☐	Report statistics to evaluate robustness of data (e.g., mean square of weighted deviates [MSWD], *p* value)
☐	Publish data tables in tabular (e.g., CSV, XLS) or machine-readable (e.g., JSON/XML) file formats
Recommended data	
☐	Describe sample treatment (e.g., mineral separation techniques, acid treatment used)
☐	Identify data reduction software used (e.g., Mass Spec, ArArCALC, Pychron, in-house)
☐	List grain size of material analyzed
☐	Report representative blank measurements
☐	Report frequency of blank/air/cocktail measurements

†Corrected for baseline, background, mass discrimination, and/or detector intercalibration, reactor interferences, and radioactive decay.

§For terrestrial samples, this is commonly the composition of atmospheric argon.

A key barrier to the widespread adoption of FAIR practices in geochronology is the lack of cyberinfrastructure to support this new emphasis on consistent, interoperable, and discoverable data products. Community-wide discoverability is crucial for data reuse; it is a precondition for envisioned large-scale, data-mining efforts, which can or plan to build aggregate age models from geochronology measurements (e.g., Macrostrat; Peters et al., 2018; MagIC; EarthRef.org Digital Archive [ERDA]; Paleobiology Database [PBDB]). However, geochronologic data often end up stored on local laboratory hard drives and only exposed to the scientific community through publication. The National Science Foundation–funded community archive for geochronologic data, the Geochron database (http://www.geochron.org/),was created as an effort to improve to the availability and interdisciplinary usage of geochronologic data. Yet, the centralized architecture of Geochron (and most traditional databases) relies on researchers themselves to manually import data in a strict format for it to be used and discoverable, a significant workflow hurdle that has caused the resource to remain underutilized. New tools are needed to ensure that laboratories can make their data available without adding additional steps to already complex workflows. The public availability of machine-readable data products can be supported by forward-looking and automated laboratory data management practices. Laboratory analytical software is most useful when supplemented with components to handle management, discoverability, and interoperability; modern data management software such as ArArSUITE (http://geochronology.coas.oregonstate.edu/software/#ArArSUITE), Pychron (Ross, 2019), or Sparrow (https://sparrow-data.org/; Quinn et al., 2019) can assist with the automation of these processes. A limiting factor in the success of $^{40}Ar/^{39}Ar$ data sets to achieve FAIR ideals relies on a scientist's willingness to follow the requirements set forth in Table 4. Unfortunately, a decade after the introduction of the data reporting norms of Renne et al. (2009), there continue to be widespread examples of published $^{40}Ar/^{39}Ar$ data sets that ignore these requirements. We strongly emphasize the importance of including the full suite of metadata in Table 4 within supplements to complement $^{40}Ar/^{39}Ar$ data within publications. As such, we strongly recommend that editors and reviewers use Table 4 as a checklist to ensure that future $^{40}Ar/^{39}Ar$ data sets contain this required information prior to publication (Supplemental Material, see footnote 1).

The suggestion to reclassify some values previously regarded as nonessential to required items in Table 4 follows the FAIR initiative.

The most notable example is the final model $^{40}Ar/^{39}Ar$ date. Although Renne et al. (2009) suggested that providing $^{40}Ar/^{39}Ar$ dates is optional because they can be derived from relative abundances, we recommend that the calculated model dates be required within $^{40}Ar/^{39}Ar$ tables to greatly increase convenience and improve interpretation of published data. Thus, the burden of calculating model dates need not be placed on the consumer but instead rests with the geochronologist or laboratory that generated them. Reporting final model dates at the 2σ level (or 95% confidence) is common practice among other geochronologic communities, most notably U-Th-Pb (Horstwood et al., 2016; Dutton et al., 2017). With respect to $^{40}Ar/^{39}Ar$ data, it is common practice to report analytical uncertainties for individual analyses at the 1σ level and the final interpreted dates at the 2σ level (e.g., Fig. 2). When reported date uncertainties include decay constant uncertainties, they can be directly compared to results from different isotope systems (e.g., Schmitz, 2012).

Data Corrections and Factors Contributing to Uncertainties

During noble-gas mass spectrometry, Ar isotope ion currents are measured over regular time intervals for a duration of a few minutes. The signal intensity changes systematically during the analysis due to the competing effects of gas consumption by the filament and degassing of additional Ar from the internal surfaces of the instrument (the "memory" effect). By convention, all calculations use the isotopic values and associated uncertainties of the intercepts that are determined via regression to "time zero" (t_0). The definition of t_0 varies amongst laboratories and software packages; the most common is the time of gas introduction into the mass spectrometer, but some laboratories use two thirds of the gas-equilibration time. In the following section, we describe each of the factors contributing to $^{40}Ar/^{39}Ar$ age uncertainties:

(1) Baseline measurement and correction: Voltage or current measurements on Faraday collectors have two parts: a baseline and an "on-peak" measurement. The thermal noise of the amplifier that is associated with a Faraday detector, referred to as the Johnson-Nyquist noise, is determined via a baseline measurement of the signal intensity "off-peak," typically at the "half-mass" position, e.g., halfway between two peaks. For $^{40}Ar/^{39}Ar$ analyses, baselines are measured either just before or after the sample/blank/air analysis. The optimal duration of the baseline versus on-peak measurements depends on the size of the ion beam and the size of the amplifier's resistor. The uncertainty in the baseline-subtracted intensity measurement is the quadratic sum of the baseline and on-peak uncertainties. Similarly, for signals measured in an ion-counting detector, a baseline measurement, often referred to as "zero" or "dark noise" measurement, is required. The source of the ion-counting detector noise is primarily related to the discriminator settings or implantation of radioactive isotopes. The uncertainty in the "zero" or "dark noise" measurements is propagated with the on-peak uncertainty in quadrature.

(2) Blank correction: The gas extraction system and mass spectrometer will register a detectable background signal that is measured during a separate "blank" run and subtracted from the measured sample signal. This blank incorporates the backgrounds and rise rates of both the mass spectrometer and extraction line measured over some interval. This presents a challenge for making the best estimation of the blank correction because the blank is not measured at the same time as the sample. Finding the best pattern of measurement of samples, monitors, and blanks is thus a key element of making the best-quality age determinations, and the pattern chosen is not the same in all laboratories. However, it is critical that uncertainty arising from the blank correction reflects the variability of blanks rather than the precision with which the blank can be measured.

(3) Detector calibration: Early noble-gas mass spectrometers had a single ion collector, and Ar isotopic measurements were performed by "peak hopping," where the magnetic field strength of the mass spectrometer was varied to alternate between isotopic masses. In recent years, a new generation of multicollector noble-gas mass spectrometers has been developed, which allow multiple isotopes to be analyzed simultaneously (e.g., Mark et al., 2009). However, the different ion detectors in a multicollector mass spectrometer do not necessarily respond equally to ion beams of equal mass and size. Because many different instruments with different collector configurations exist, detector calibrations are often specific to each laboratory. Some, but not all, mass spectrometers have a stable voltage supply to intercalibrate gains electronically. Collectors can also be calibrated by applying an ion beam of known size across the detectors and monitoring the response relative to the other resistor circuits (e.g., Mark et al., 2009; Turrin et al., 2010), or measuring a "gas cocktail" with an independently known Ar isotope composition (e.g., Coble et al., 2011; Jicha et al., 2016).

(4) Mass fractionation (i.e., instrumental mass bias or mass discrimination): The mass spectrometer itself causes changes to the measured isotope abundances and thus the expected ratios (i.e., Ireland, 2013). Specifically, mass fractionation is partly due to extraction efficiency from the source following ionization (see discussions in Turrin et al., 2010; Mark et al., 2011). Mass bias can also be imposed by detectors, and so the bias is a composite of effects imposed by both source and detector. These effects in general cannot be deconvolved, and thus the relationship between mass difference and bias (e.g., linear, power law, exponential) must be determined empirically (e.g., Renne et al., 2009). The mass fractionation correction can be significant, especially for samples with low radiogenic ^{40}Ar signals (i.e., Turrin et al., 2010), and significant errors can result if mass fractionation and its associated uncertainty are not accounted for properly. The mass fractionation factor can be quantified by comparing the measured $^{40}Ar/^{36}Ar$ signal ratio of an air aliquot on several detectors or that of an artificial gas cocktail with known Ar isotopic ratios and associated uncertainties.

(5) Trapped Ar correction: Despite the incompatibility of noble gases within the crystal structure of most minerals (e.g., Kelley, 2002; Jackson et al., 2015; Krantz et al., 2019), nonradiogenic ^{40}Ar, co-located with ^{38}Ar and ^{36}Ar, is hosted in mineral and melt inclusions, found in trace quantities in crystal lattices, and adsorbed on mineral surfaces. On Earth and Mars, Ar is a major constituent of the atmosphere, and atmospheric Ar is often observed during sample degassing (e.g., Bogard and Johnson, 1983; Walton et al., 2007). On the Moon, the trapped gas composition reflects implanted parentless ^{40}Ar and solar wind Ar (e.g., Eberhardt et al., 1970; Yaniv and Heymann, 1972). On Earth, magmatic minerals that crystallize under a high partial pressure of Ar may incorporate mantle or crustal Ar. Isochron regressions can sometimes be used to deconvolve the isotopic composition of the trapped Ar component from the $^{40}Ar^*/^{39}Ar_K$ ratio of a sample, such that an age can be calculated after appropriately correcting for excess argon (Heaton and Koppers, 2019).

(6) Cosmogenic Ar correction: Samples that have resided within meters of planetary surfaces accumulate ^{40}Ar, ^{38}Ar, and ^{36}Ar through spallation reactions between cosmic rays, secondary reaction products, and heavier target nuclei of K, Ca, Cl, Fe, Mn, Ni, Cr, and Ti. Thus, most lunar, Martian, and asteroidal samples found on Earth contain cosmogenic Ar because they were exposed to cosmic rays during transit through space. On Earth, the production rate is sufficiently low due to shielding of cosmic rays by the magnetic field and atmosphere such that cosmogenic corrections can be neglected. Although the cosmogenic correction to ^{40}Ar is generally insignificant, the correction to ^{36}Ar, which in turn is used to deconvolve trapped and radiogenic ^{40}Ar on isochron diagrams, is often significant (e.g., Bogard and Garrison, 1999).

Therefore, assumptions and uncertainties in the application of the cosmogenic correction (for a review, see Cassata and Borg, 2016) can hinder attempts to obtain per mil uncertainties on some extraterrestrial samples.

(7) Interference correction: The $^{40}Ar/^{39}Ar$ method pairs the natural radioactive decay of ^{40}K to ^{40}Ar with synthetic activation of ^{39}K to ^{39}Ar. Neutron activation also produces not only ^{39}Ar but also a host of other Ar isotopes. For example, some ^{40}Ar is produced by neutron activation of ^{40}K, which is added to that produced from natural radioactive decay of ^{40}K; additional ^{39}Ar is produced from ^{42}Ca; and ^{36}Ar is produced from ^{40}Ca and ^{35}Cl. Corrections for interfering reactions are achieved by co-irradiating K-doped glass and fluorite and analyzing the full suite of (^{36}Ar, ^{37}Ar, ^{38}Ar, ^{39}Ar, ^{40}Ar) isotopic compositions in both the monitors and samples.

(8) Decay correction: Two of the five measured Ar isotopes are radioactive nuclides produced during irradiation: ^{37}Ar ($t_{1/2} = 34.95 \pm 0.08$ d; Renne and Norman, 2001) and ^{39}Ar ($t_{1/2} = 269 \pm 3$ yr; Stoenner, 1965). A correction is required for the decay of these isotopes during the time elapsed between irradiation and analysis. Also, ^{36}Cl decays to ^{36}Ar with a half-life of ~300 k.y. and can be a significant correction for young, Cl-rich samples that are analyzed many months following irradiation.

(9) Irradiation parameter (J): The parameter J, which quantifies the production of ^{39}Ar from ^{39}K in the age equation, is determined by analyzing a co-irradiated fluence monitor with accurately known age. The J value varies horizontally and vertically in an irradiation stack due to neutron flux gradients in the reactor (e.g., Rutte et al., 2015), which can be quantified by analyzing numerous fluence monitors interspersed with the samples at known positions relative to each other.

(10) K isotope effects: The $^{40}Ar/^{39}Ar$ system assumes that $^{40}K/K$ values are equivalent for samples, monitors, and materials used for decay constant determinations. Although potassium stable isotopes are typically assumed to be constant in nature due to the lack of variability found by Humayun and Clayton (1995), more recent work (e.g., Morgan et al., 2018) has identified terrestrial variability in $\delta^{41}K$ (defined as variations in $^{41}K/^{39}K$ relative to a standard). The effects of this variability are likely negligible for many samples, and $\delta^{41}K$ is not routinely measured on samples undergoing $^{40}Ar/^{39}Ar$ analysis, but for some samples, the effect on ages could exceed 1‰. Unless ^{40}K measurements are also made, the apparent effect on $^{40}K/K$ requires an assumption that mass-independent effects are not in play.

Most igneous rocks have a limited range in $\delta^{41}K$ values (±0.2‰), as shown by the work of Wang and Jacobsen (2016), Li et al. (2019), Morgan et al. (2018), and Tuller-Ross (2019). The exceptions to this limited range in $\delta^{41}K$ are pegmatites and some hyperalkaline volcanic rocks (e.g., the Alban Hills of Italy) that have a 2.5‰ range in $\delta^{41}K$ values (Morgan et al., 2018). Another factor that affects most $^{40}Ar/^{39}Ar$ ages is the ~0.5‰ difference in $\delta^{41}K$ between silicates and evaporites, and the relatively minor (0.26‰) differences found between commonly used fluence monitors. Based on $\delta^{41}K$ measurements from Morgan et al. (2018), the most likely effect of K isotope variability is that the age of fluence monitors GA1550 and FCs is underestimated by 35 k.y. and 7 k.y., respectively. As the precision and accuracy of the $^{40}Ar/^{39}Ar$ system improve, correcting for variable $\delta^{41}K$ on monitors may become routine, and $\delta^{41}K$ measurements on samples may be important in some cases.

(11) Sample averaging: The J parameters and $^{40}Ar/^{39}Ar$ ratios obtained from the previous steps provide all the elements needed to calculate a single $^{40}Ar/^{39}Ar$ date. However, it is usually beneficial to combine multiple analyses together to improve the precision of the dates and assess their reproducibility. These analyses may be total fusion dates or heating steps in an incremental heating experiment. In order to assess the reproducibility of sample or fluence monitor analyses, repeated measurements are recommended whenever possible. The resulting data can be averaged by taking a weighted mean, or by forming a combined isochron from the replicate analyses.

Each step in the $^{40}Ar/^{39}Ar$ data-processing chain involves statistical uncertainty. The effect of the uncertainties from each Ar isotope measurement and the subsequent corrections to it will vary significantly in materials of different ages and compositions. Figure 4 shows

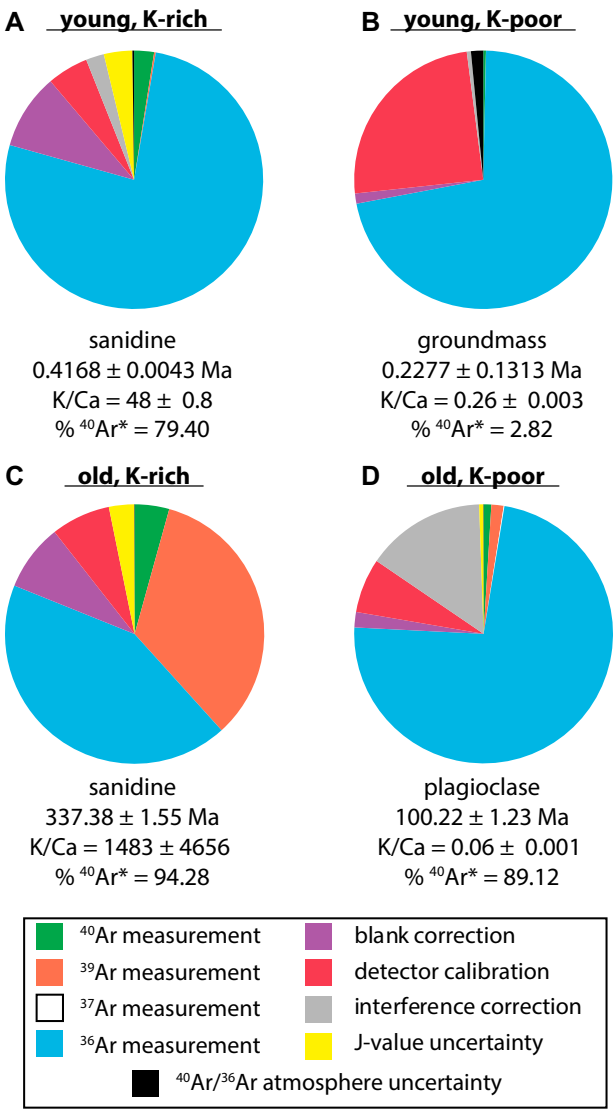

Figure 4. $^{40}Ar/^{39}Ar$ uncertainty budget (without uncertainties in decay constants) for a single analysis from four samples analyzed at the WiscAr geochronology laboratory at the University of Wisconsin–Madison. Data were reduced using Pychron software (Ross, 2019), which propagates and tracks uncertainties using the Python uncertainties package 3.0.1. For this example, the detector calibration incorporates the mass fractionation correction. All uncertainties are 2σ.

the results of a sensitivity analysis performed at the WiscAr geochronology laboratory at the University of Wisconsin–Madison. Measurements were performed using a Nu Instruments Noblesse multicollector mass spectrometer, and data were reduced using the Pychron software package (Ross, 2019). The ^{36}Ar abundance is typically several orders of magnitude smaller than that of ^{40}Ar or ^{39}Ar and dominates the uncertainty budget for most materials (Fig. 4). This measurement is critically important for the correction of trapped atmospheric argon. The duration for which a material is irradiated is typically optimized as a function of its presumed age and composition (Turner, 1971) and the power of the reactor, with the goal of producing enough ^{39}Ar such that a $^{40}Ar/^{39}Ar$ ratio of 1 to 50 is achieved (Dalrymple et al., 1981). Consequently, Quaternary samples require relatively short irradiation times, <1 h (at a 1 MWh reactor), whereas Paleogene and older samples might be irradiated for 1 to >50 h (at a 1 MWh reactor). In the case of older sanidine samples, the uncertainty of the ^{39}Ar measurement is more important in the uncertainty budget (Fig. 4C) compared to a young sanidine (Fig. 4A) that spent little time in the reactor. Composition is also relevant, as the sanidine in both examples in Figure 4 (Fig. 4A and Fig. 4C) contained very little Ca, resulting in negligible contributions by the interference corrections to the overall uncertainty budget. Conversely, for a Ca-rich material like plagioclase, the $(^{36}Ar/^{37}Ar)_{Ca}$ and $(^{39}Ar/^{37}Ar)_{Ca}$ interference corrections contribute much more to the uncertainty of old samples, which spend tens of hours in the reactor (Fig. 4D). It is important to note that these uncertainty budgets are only examples from a single laboratory and are highly dependent on the type of detectors (in this case, ion counters), and hence instrument, used for analysis, along with irradiation parameters and reactor conditions. However, Figure 4 illustrates that careful optimization of the irradiation duration is required prior to analysis.

Random vs. Systematic Uncertainties

Statistical uncertainties are classified into random and systematic components (Renne et al., 1998). Random (or internal) errors originate from electronic noise in the ion detectors, counting statistics, and temporal variability of the blank as a result of changes in the laboratory environment. The uncertainty associated with random errors can be quantified by taking replicate measurements. The standard error of these measurements ($\sigma/\sqrt{n}$, where σ is the standard deviation of n replicate measurements) is a measure of their precision. The standard error can be reduced to arbitrarily low levels by simply averaging more measurements. Systematic (or external) errors are those caused by uncertainty in the assumptions made to calculate a $^{40}Ar/^{39}Ar$ date from analytical data. These include the systematic effects of decay constant uncertainty, the age of the monitor, and the air ratio. In contrast with the random uncertainties, the systematic uncertainties cannot be characterized by repeat measurements, and they cannot be reduced by simple averaging.

Care must be taken when deciding which sources of uncertainty are included in the error propagation. Intersample comparisons of $^{40}Ar/^{39}Ar$ data may legitimately ignore systematic uncertainties as well as those of intercalibration factors. However, when comparing a $^{40}Ar/^{39}Ar$ date with a U/Pb, astrochronologic date, or ^{14}C date, both random and systematic uncertainties must be considered. The conventional way to tackle both types of comparison is called "hierarchical" error propagation (Renne et al., 1998; Min et al., 2000, Koppers, 2002). Under this paradigm, the random uncertainties are processed first, and the systematic uncertainties are processed afterwards. Vermeesch (2015) showed that the internal and external errors can also be processed jointly, in matrix form. This algorithm solves the problem with hybrid error models, but it has not yet been widely adopted by the $^{40}Ar/^{39}Ar$ community.

STRATEGIES FOR INTERPRETING $^{40}Ar/^{39}Ar$ DATA

To facilitate interpretation of $^{40}Ar/^{39}Ar$ data, we first discuss common statistical tools utilized in $^{40}Ar/^{39}Ar$ geochronology for evaluating dates and data sets. We then focus on some typical approaches for the interpretation of $^{40}Ar/^{39}Ar$ data from: (1) single-crystal fusion data sets, (2) incremental heating data sets for volcanic rocks, (3) incremental heating data sets for plutonic or metamorphic rocks, (4) provenance studies using detrital minerals, and (5) low-temperature processes. This discussion is intended to serve as a guide for the interpretation and understanding of the complexities associated with individual $^{40}Ar/^{39}Ar$ data sets.

Common Statistical Tools: Pitfalls and Opportunities

MSWDs and Evaluation of Under- versus Overdispersed Data

The random scatter of the data about an isochron or weighted mean fit can be assessed using the mean square of the weighted deviates (MSWD; McIntyre et al., 1966). This statistic is more generally known as the "reduced chi-square statistic" outside geology. The MSWD is defined as the sum of the squared differences between the observed and the expected values, normalized by the analytical uncertainties and divided by the degrees of freedom (*df*) of the fit. In the context of the weighted mean age, the MSWD of n values is given by:

$$MSWD = \frac{1}{df}\sum_{i=1}^{n}\frac{\left(x_i - \overline{x}\right)^2}{\sigma_i^2}, \qquad (1)$$

where x_i is the i^{th} (out of n) dates, σ_i is the corresponding analytical uncertainty, *df* is the number of degrees of freedom, defined as $df = n - 1$, and $\overline{x}$ is the weighted mean of all n dates. The definition for the MSWD of an isochron is similar but has one fewer degree of freedom ($df = n - 2$) and involves a few more terms to account for correlated uncertainties between the x and y variables. The following are general MSWD considerations:

(1) If the analytical uncertainties (σ_i) are the only source of scatter between the n aliquots, and *df* is reasonably large (for example, $n > 20$), then MSWD ≈ 1 (Figs. 5A and 5B). For smaller sample sizes, the MSWD has a much wider distribution with an expected value of less than one (Wendt and Carl, 1991; Mahon 1996). The remainder of this section will assume $n > 20$.

(2) MSWD values <<1 indicate that analytical uncertainties have been overestimated or have not been propagated correctly (Figs. 5C and 5D). Assigning ages to samples based on underdispersed data must be done with caution.

(3) MSWD values considerably greater than one indicate that there is some excess scatter in the data, which cannot be explained by the assumed analytical uncertainties alone. This may reflect underestimation of analytical uncertainties, but it usually reflects the presence of some geological overdispersion affecting the data set and/or neutron fluence gradients. Possible causes of such dispersion may include the protracted crystallization history of a sample, variable degrees of inheritance, or partial loss of radiogenic ^{40}Ar by retrograde reactions, thermally activated volume diffusion, deformation, or chemical alteration (Figs. 5E and 5F).

The upper 95% confidence limit of the MSWD (i.e., the critical MSWD) can be calculated as below, following Wendt and Carl (1991).

$$critical\ MSWD = 1 + 2\left(\frac{2}{f}\right)^{\frac{1}{2}}, \qquad (2)$$

where f is the degrees of freedom. Critical MSWD values were also reported in Mahon (1996). Wendt and Carl (1991) demonstrated that the expectation (or mean) value of MSWD is 1, and this is not a function of f; however, the standard deviation of the expectation value

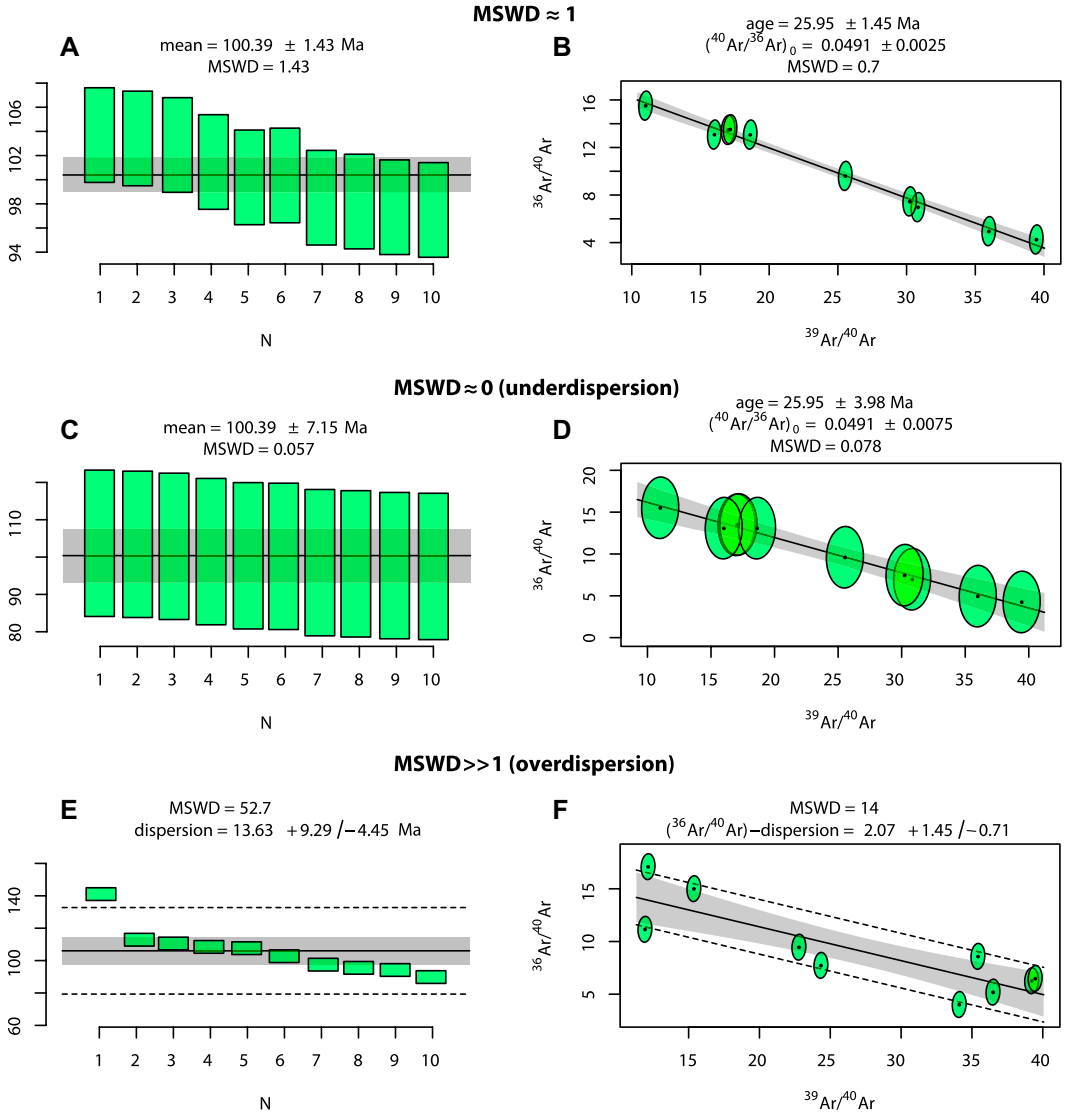

Figure 5. Six different synthetic $^{40}Ar/^{39}Ar$ data sets shown as rank order plots with weighted means and inverse isochron plots. The analytical uncertainties are shown as 95% error bars and error ellipses, respectively. Each of the data sets consists of 10 aliquots that are affected by a combination of analytical and geological dispersion. The relative importance of these two sources of scatter can be assessed using the mean square of weighted deviates (MSWD). (A, B) If the analytical uncertainties alone explain the total scatter around the true mean, then the MSWD is expected to take on a value of ~1. (C, D) Data sets that exhibit MSWD values close to zero are said to be "underdispersed" with respect to the analytical uncertainties. This indicates some problem with the error propagation, which is often due to undetected systematic effects. (E, F) Finally, MSWD values >1 can often be attributed to some form of geological dispersion. This overdispersion carries geological significance. All uncertainties are reported at 95% confidence. The two age uncertainties in panels E and F are without and with overdispersion, respectively.

for the MSWD decreases with increasing *f*. A MSWD value for a data set that is greater than the critical MSWD value, calculated as above, indicates with >95% probability that there is more scatter in the data than can be accounted for by the reported uncertainties.

Data sets with MSWD ≈ 1 are not the only data suitable for publication. Trimming an overdispersed data set by selectively rejecting outliers until achieving a MSWD ≈ 1 is also ill-advised because this risks the loss of geologically valuable information and biasing the results. Outlier identification and rejection must always be accompanied by full disclosure of the specific criteria used for such evaluation, and not simply to improve the statistics of a data set. MSWD values >>1 do not necessarily indicate poor data and may simply reflect high analytical precision of the data or underestimation of analytical uncertainties. Increasingly dispersed data sets are likely to become even more prevalent in the future, as a result of the ever-increasing improvements of mass spectrometers with the potential to further increase precision of measurements. In this case, the excess dispersion can be formally assessed with a chi-square test for homogeneity, and its associated *p* value. However, unpowered statistical hypothesis tests (e.g., *p* values) have come under criticism in recent years, and scientists are increasingly advised not use them (Wasserstein and Lazar, 2016; Amrhein et al., 2019).

Dispersed data sets need to be evaluated carefully on a case by case basis, and any conclusions based on dispersed data must be made with caution. It is important to consider the potential causes (geologic, analytical, mineralogic, etc.) of the data dispersion (e.g., Verati and Jourdan, 2014; Phillips et al., 2017). In some cases, a subset of a dispersed data set can be used to assign an age for a sample given sufficient geologic context. For example, single-crystal fusion dates from a volcaniclastic layer intercalated within a fluvio-lacustrine succession along the Tiber River, Italy, showed significant dispersion (MSWD = 603; Marra et al., 2019). The volcaniclastic layer has lithologic and mineralogic characteristics that are nearly identical to another volcaniclastic layer located ~6 km to the northwest that was dated at 327.5 ± 3.5 ka. The youngest six $^{40}Ar/^{39}Ar$ dates of the dispersed data set give a weighted mean age of 328.7 ± 1.6 ka, which led Marra et al. (2019) to conclude that the two dated volcaniclastic layers are indeed identical and have been tectonically displaced by 50 m.

When no potential sources of data dispersion can be confidently identified, it can be assumed that the excess dispersion is multiplicative and scales in proportion to the analytical uncertainty. In this case, the standard error of the weighted mean or isochron intercept may be augmented by

multiplying it with the square root of the MSWD. A second option is to parameterize the overdispersion as an additive term and estimate it as a separate parameter (Vermeesch, 2018). Finally, the validity of using the MSWD value to monitor excess scatter relative to the 95% confidence interval is a function of *n* (Mahon, 1996). That is, for small data sets, there can be significant deviation from MSWD = 1 for data that are normally distributed at the 95% confidence interval.

Probability Density Plots and Kernel Density Estimations

Isochrons and weighted mean plots are useful for data sets that contain a relatively small number of tightly clustered dates. However, these plots are ill suited for evaluation of distributions, where ages span large time intervals (e.g., detrital or weathering geochronology). In this case, it is not so much the individual dates that contain the geologically meaningful information, but rather the full distribution of the dates. Histograms are one way to visualize such data sets. This visualization requires binning, and the number of apparent age components may vary significantly depending on the size and placement of the bins.

To address this issue, geochronologists introduced the probability density plot (PDP) as a continuous alternative to the histogram. PDPs are also referred to as a type of ideogram in the context of $^{40}Ar/^{39}Ar$ geochronology (Deino and Potts, 1991). They are generated by ranking the dates from youngest to oldest, stacking a Gaussian bell curve on each date, where the standard deviation corresponds to the analytical precision, and summing all the bell curves together to form a single continuous distribution.

We note that when the analytical uncertainty becomes very small compared to the range of dates, the PDP resembles a number of "spikes." This trend is likely to become ever more prevalent if the trend towards increasing analytical precision continues.

An alternative to PDPs is a kernel density estimation (KDE), which uses a procedure that is broadly similar in construction to PDPs. Like PDPs, KDEs are also constructed by (1) ranking the dates in increasing order, (2) assigning a bell curve (or any other symmetric shape or "kernel") to each date, and (3) summing all these curves to form one continuous line. However, where PDPs use the analytical precision to set the width of the kernels, KDEs do so using independent statistical means (Fig. 6; Vermeesch, 2015).

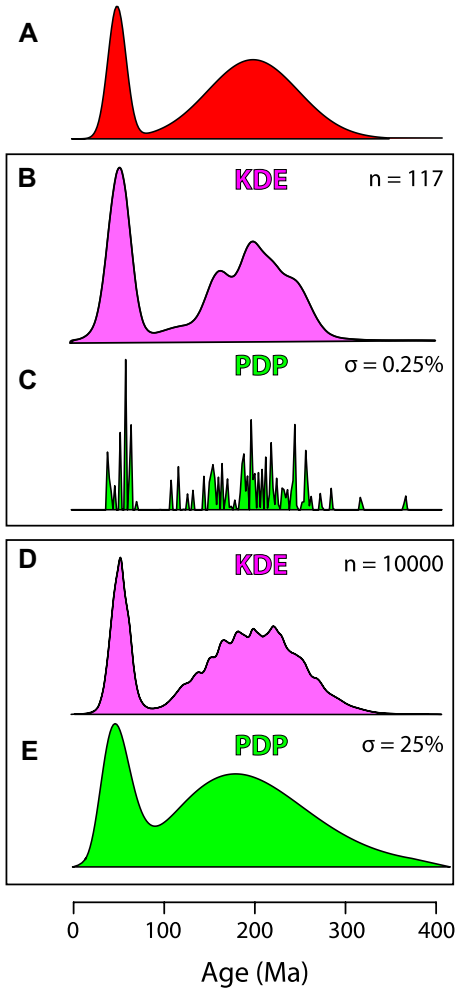

Figure 6. Comparison between probability density plots (PDPs) and kernel density estimation (KDEs) using a synthetic bimodal data set consisting of two normal distributions. (A) True distribution of the dates is shown in red. (B) KDE of a representative sample of randomly selected grains from this distribution. (C) Corresponding PDP of the same sample in B, assuming an analytical uncertainty of 0.25%, which is readily achievable with modern noble-gas mass spectrometers. Due to the high precision, the PDP breaks down into a sequence of spikes that bears little resemblance to the true distribution. (D) KDE of a large sample of (*n* = 10,000) analyses from the true distribution. Due to the large sample size, the KDE has converged closely to the true distribution. (E) Corresponding PDP of the same sample in D, assuming large (25%) analytical uncertainties. In this case, the PDP oversmooths the distribution of the dates.

Interpreting Single-Crystal Data Sets for Volcanic Rocks

$^{40}Ar/^{39}Ar$ dating of single minerals hosted in volcanic rocks, either by total fusion or incremental heating, is one way to estimate the eruption age. Single-crystal analyses are typically performed on K-rich mineral phases such as sanidine, anorthoclase, micas, or hornblende, but analysis of plagioclase or other low-K phases is possible. For pyroclastic deposits, analyses of single crystals are preferred because the crystal cargo may consist of minerals with different crystallization and/or alteration/thermal histories. For this reason, multicrystal analyses must be avoided whenever possible.

A first step toward the interpretation of a collection of single-crystal dates from a volcanic rock or tephra is to decide what value to assume for the $^{40}Ar/^{36}Ar$ initial ratio. In many cases, analysts begin with the assumption of a ratio equivalent to that of modern atmosphere and calculate what are commonly referred to as $^{40}Ar/^{39}Ar$ model dates. It is also common practice to plot all of the data on a normal or inverse isotope correlation diagram (Fig. 5) and, if the data define a robust linear relationship (as indicated by the MSWD for the isochron fit), to use the intercept to estimate an initial trapped $^{40}Ar/^{36}Ar$ ratio to use in (re)calculating model dates. The dates can then be plotted on a diagram such as that shown in Figure 7A, and a preliminary inverse-variance-weighted mean for all of the dates—as well as the MSWD for the weighted mean—can be calculated. In an ideal system, all crystals hosted in a volcanic rock will have incorporated no radiogenic or excess Ar prior to eruption due to storage at high temperatures. Therefore, the dispersion in the single-crystal $^{40}Ar/^{39}Ar$ dates for a volcanic sample is expected to reflect solely the analytical uncertainty of the mass spectrometer analyses (assuming no reactor fluence gradients, self-shielding, etc.). In this case, the weighted mean date can be calculated from the entire single-crystal data set, and its MSWD will be lower than the MSWD value deemed acceptable for the total number of analyses at 95% confidence (i.e., critical MSWD, Eq. 2).

In cases where the MSWD is less than the critical MSWD, it is reasonable to interpret the weighted mean date and its uncertainty as representative of the eruption age of the volcanic rock. However, with improved precision in $^{40}Ar/^{39}Ar$ geochronology (e.g., Fig. 2), it has become increasingly commonplace to observe more variability in single-crystal $^{40}Ar/^{39}Ar$ dates from a sample than can be explained by analytical uncertainty alone (e.g., Andersen et al., 2017; Ellis et al., 2017; Stelten et al., 2015; Rivera et al., 2016, 2018; see Figs. 7B and 7C). Under such circumstances, the MSWD calculated for the complete data set will exceed its critical threshold, and the mean for all crystals cannot be interpreted as the eruption age.

In many cases, such data sets will have distributions such as those shown in Figure 7A, with a dominant mode and a tail towards older and/or younger dates. The older single-crystal dates

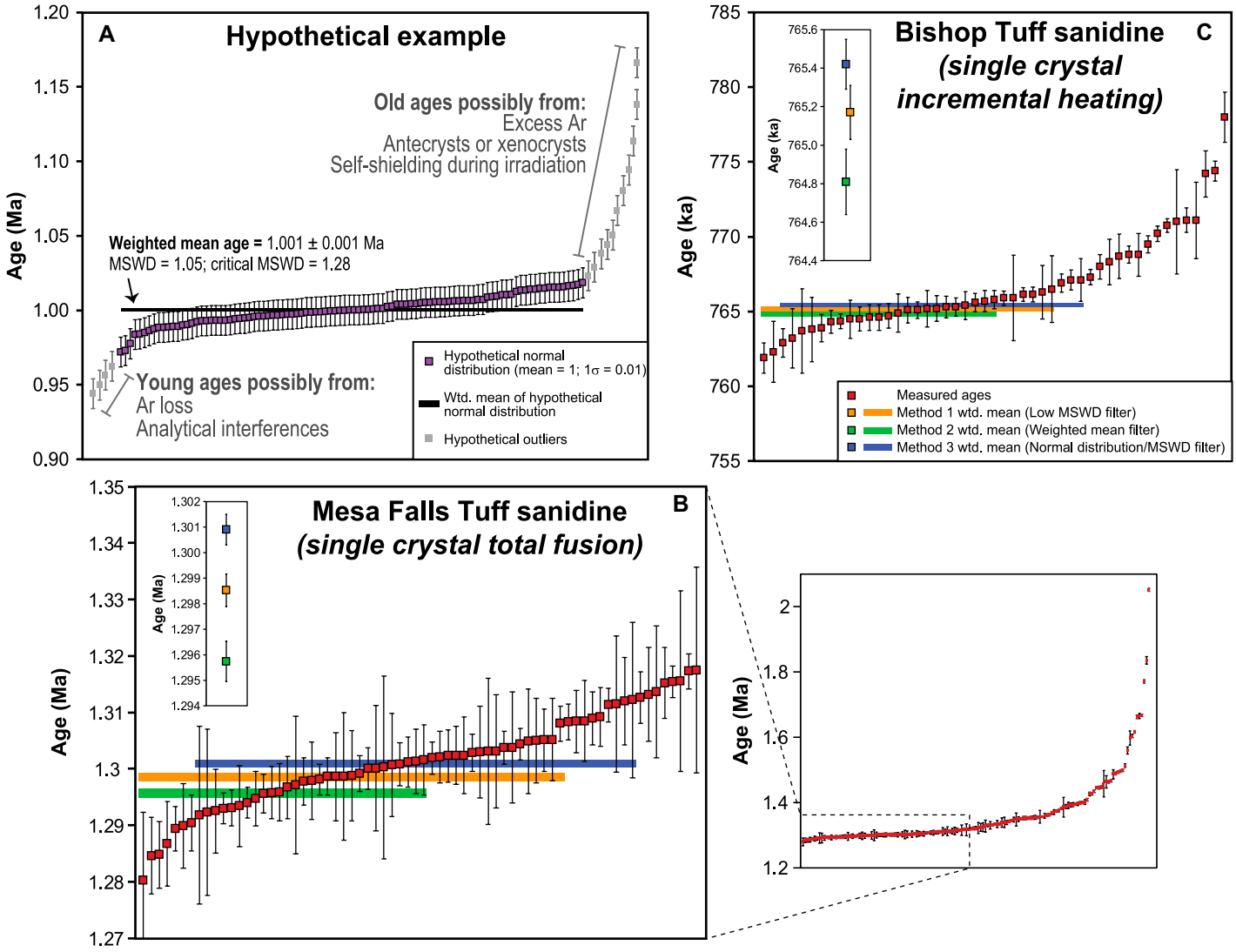

Figure 7. Interpretation of single-crystal $^{40}Ar/^{39}Ar$ age data. All uncertainties in this diagram are 1σ. (A) Hypothetical age data randomly sampled from a normal distribution with a mean age of 1 Ma and 1σ of 0.01 Ma (purple data points); all analytical errors are assumed to be 0.01 Ma. The weighted mean for this population is within error of the true age and yields a mean square of weighted deviates (MSWD) less than the critical MSWD (Wendt and Carl, 1991). Gray data points represent anomalously young and old ages commonly observed in single-crystal data sets. (B) Single-crystal total fusion data for Mesa Falls Tuff sanidine from Ellis et al. (2017). (C) Single-crystal incremental heating data for Bishop Tuff sanidine from Andersen et al. (2017). In panels B and C, the horizontal colored bars represent the weighted mean age and 1σ error calculated using the different filtering methods. The data included in each weighted mean are indicated by the horizontal extent of the colored bars. Insets in panels B and C show the average ages calculated using the different filtering methods. The smaller image outside of panel B shows the entire range of single-crystal $^{40}Ar/^{39}Ar$ ages for the Mesa Falls Tuff, and the dashed box shows the region of data displayed in panel B.

are most commonly interpreted to reflect excess Ar trapped within the crystals (e.g., Ellis et al., 2017) and/or the presence of antecrysts or xenocrysts (routinely diagnosed by mineral chemistry) that have not been fully degassed (e.g., Andersen et al., 2017; Rivera et al., 2016, 2018). A tail towards younger ages may represent variable partial Ar loss from the crystals or the presence of an unrecognized interference during the mass spectrometer analyses (e.g., a hydrocarbon interference may lead to anomalously high ^{36}Ar signal size and therefore a younger date; Fig. 7A). In general, greater dispersion in single-crystal dates is observed in total-fusion experiments relative to incremental heating experiments, because the latter provide an independent means of rejecting grains that display evidence for excess Ar or Ar loss, or that otherwise do not yield plateaus (cf. Rivera et al., 2016; Ellis et al., 2017). Some of the dispersion may also be attributed to flux gradients or self-shielding during sample irradiation, but these issues have yet to be fully understood.

Increased recognition of overdispersion in single-crystal data sets due to enhanced analytical precision has made interpreting the best estimate of an eruption age much more challenging than it was when methods were less precise. Approaches that appear in the literature include the following:

Method 1: Low MSWD weighted mean. This method assumes that the eruption age of the sample is best represented by

a group of the youngest single-crystal $^{40}Ar/^{39}Ar$ dates, whereas older dates reflect excess Ar or undegased, inherited crystals. Here, it is assumed that argon loss and young dates due to analytical interferences do not represent significant factors. An inverse-variance-weighted mean date is calculated for the youngest *n* analyses that yield an MSWD below the critical MSWD. This calculation is performed by ordering the single-crystal $^{40}Ar/^{39}Ar$ dates from youngest to oldest and calculating a running weighted mean and MSWD, starting with the youngest date, until the MSWD acceptance criteria fail (e.g., Gansecki et al., 1996; Ton That et al., 2001; Stelten et al., 2015). The final weighted mean date of this young population with an acceptable MSWD is taken to represent the eruption age of the sample. As noted above, MSWD values that approach zero indicate that analytical uncertainties have been overestimated or have not been propagated correctly. Thus, low MSWD weighted mean ages ought to be used with caution unless otherwise corroborated by other geochronologic or geologic evidence.

Method 2: Weighted mean filter. This method makes the same assumptions as in method 1. This calculation is carried out by ordering the single-crystal $^{40}Ar/^{39}Ar$ dates from youngest to oldest and calculating a running weighted mean. The youngest population of $^{40}Ar/^{39}Ar$ dates, which are interpreted to represent the eruption age, is defined as that for which the difference between the weighted mean age of the youngest group and the next oldest date is greater than zero with 95% confidence (Andersen et al., 2017). One problem with methods 1 and 2 is that they produce weighted mean ages that become younger with increasing sample size.

Method 3: Normality test and goodness-of-fit parameter. This method assumes that the population of single-crystal $^{40}Ar/^{39}Ar$ dates that best represents the eruption age of the sample follows a normal distribution and that the scatter about this eruption age is dominated by analytical uncertainty. Unlike methods 1 and 2, this method does not assume that the youngest $^{40}Ar/^{39}Ar$ ages are the best measure of the eruption age. In turn, young dates, as well as old, may be excluded from the preferred weighted mean age. This calculation can be done by ordering the single-crystal $^{40}Ar/^{39}Ar$ ages from youngest to oldest and testing every combination of contiguous data to find the largest population of data that is consistent with a normal distribution and has an acceptable degree of dispersion based on the MSWD or another goodness-of-fit parameter (e.g., Jicha et al., 2016; Ellis et al., 2017). Testing for the normality of a data set can be done using a number of statistical tests (e.g., chi-squared, Shapiro-Wilk test, Kolmogorov-Smirnov test) and may include constraints on the skewness and kurtosis of the population being examined.

For the calculations presented below, we used the MSWD and the Shapiro-Wilks normality test at a probability threshold of 0.0005 and specified that the skewness must be between –0.2 and 0.2 (using the adjusted Fisher-Pearson coefficient of skewness). To illustrate the differences in these data-filtering methods, we applied each method to single-crystal total fusion data for Mesa Falls Tuff sanidine from Ellis et al. (2017) and single-crystal incremental heating data for Bishop Tuff sanidine from Andersen et al. (2017); see Figures 7B and 7C. Single-crystal $^{40}Ar/^{39}Ar$ model dates for the Mesa Falls Tuff sanidine range from 1.280 Ma to 2.052 Ma and show a large tail towards older ages. Application of the filtering methods described above yielded inverse-variance-weighted mean dates of 1.2985 ± 0.0006 Ma ($n = 53/147$) for method 1, 1.2957 ± 0.0008 Ma ($n = 36/147$) for method 2, and 1.3009 ± 0.0006 ($n = 55/147$) for method 3, respectively (Fig. 7B). The older date calculated via method 3 reflects the fact that the seven youngest analyses were rejected due to a non-normal distribution. Methods 1 and 2 yielded younger dates because the youngest single-crystal dates are always included in the weighted mean. In this case, Ellis et al. (2017) noted that the inverse-variance-weighted mean date derived from method 3 (1.3009 ± 0.0006 Ma) agrees well with the zircon U/Pb data for this sample, 1.3004 ± 0.0007 Ma, and suggested that this value represents the best eruption age estimate for this sample. The seven youngest single-crystal ages that were excluded from the weighted mean may have experienced Ar loss, or the analyses may have been affected by isobaric interferences.

Bishop Tuff single-sanidine plateau dates (Andersen et al., 2017) also show a distribution with a tail towards older dates. Application of methods 1, 2, and 3 yielded inverse-variance-weighted mean dates of 765.2 ± 0.14 ka ($n = 31/49$) for method 1, 764.8 ± 0.17 ka ($n = 25/49$) for method 2, and 765.4 ± 0.13 ($n = 32/49$) for method 3 (Fig. 7C). The older date calculated via method 3 is due to the rejection of the two youngest analyses. Andersen et al. (2017) argued that because single-crystal incremental heating provides an independent check on Ar loss and/or young dates resulting from analytical interferences, the use of method 2 provides the most robust estimate of the eruption age for this sample. In both of the example data sets, the use of different filtering methods results in inverse-variance-weighted mean dates that differ outside of their 1σ uncertainties (Figs. 7B and 7C), highlighting the importance of the choice of data-filtering method.

Although there is no a priori way to determine which filtering method is best for a given data set, we suggest that the assumptions behind these data-filtering methods should be carefully considered before applying them. Regardless of the method chosen, we suggest that any data filtering be described in sufficient detail such that it may be reproduced by other researchers. For example, if normality tests are performed during data filtering, then it behooves the author to specify the normality test that was performed and if skewness or kurtosis constraints were employed. Finally, it is important to be consistent when selecting a filtering method for multiple volcanic samples within a single study.

Interpreting Data from Incrementally Heated Volcanic Rocks

Recent improvements in multicollector mass spectrometry for $^{40}Ar/^{39}Ar$ geochronology have led to ever-improving precision on $^{40}Ar/^{39}Ar$ dates and a reduction in the amount of sample required for analysis, thereby leading to the preparation of smaller and likely more homogeneous mineral or groundmass separates. The improved precision, however, has resulted in observation of degassing patterns during incremental heating experiments that are considerably more complicated than the ideal case of a flat (i.e., concordant) age spectrum. For example, a commonly observed age spectrum shape for both individual sanidine crystals and groundmass separates starts at low temperatures with older apparent ages, high K/Ca ratios, and low radiogenic ^{40}Ar content, followed by a decrease to younger ages that sometimes form a plateau (e.g., Fig. 8A). The older apparent ages may be the result of degassing of fluid inclusions, ^{37}Ar and/or ^{39}Ar recoil loss, or redistribution from the fine-grained secondary phases in the groundmass or fine-grained groundmass during irradiation (e.g., Turner and Cadogan, 1974; Huneke and Smith, 1976; Hall, 2014; Koppers et al., 2000; Fleck et al., 2014; Jourdan and Renne, 2013).The low-temperature heating steps likely reflect preferential degassing of potassium-rich alteration phases in groundmass or K-rich melt inclusions in sanidine. The same applies to the Cl/K ratios, provided Cd shielding has not been used during irradiation. A more robust method,

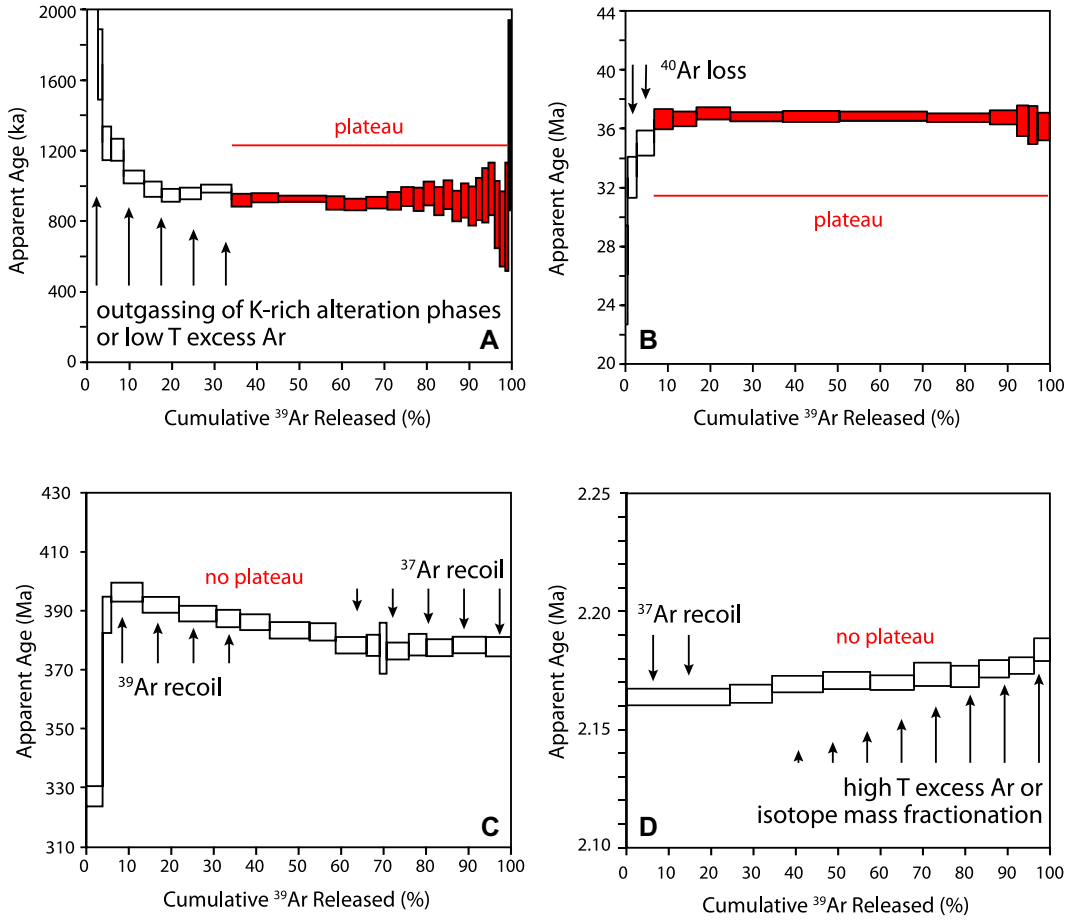

Figure 8. $^{40}Ar/^{39}Ar$ incremental heating experiments showing possible complications in age spectra. (A) Groundmass from a Galapagos lava (13D07373; Balbas et al., 2016). (B) Plagioclase from plutonic rock (AT-12-4) on the Aleutian island of Amatignak (Schaen et al., 2016). (C) Groundmass from a Ca-rich melt rock (Jourdan and Renne, 2013). (D) Anorthoclase megacryst sample (M22031) from the Anakies (east cone) of the Newer Volcanics Province (SE Australia; Matchan et al., 2018).

involving vacuum encapsulation (Villa et al., 1983; Smith et al., 1993; Hall, 2014), allows for precise quantification of recoil losses.

In some samples, the apparent ages calculated for the initial heating steps are younger than the plateau and form a staircase upward pattern towards the plateau (Fig. 8B). This is commonly interpreted to indicate radiogenic ^{40}Ar loss from alteration phases degassed at low temperature, but it may also be the result of ^{37}Ar recoil (e.g., Fleck et al., 2014). If a sample records a history of brittle deformation, younger ages at low-temperature steps could reflect Ar loss associated with deformation-recrystallization. High-temperature heating steps can variously trend towards older and younger apparent ages. Degassing of clinopyroxene and plagioclase microphenocrysts within groundmass generally results in lower K/Ca ratios and younger apparent ages due to the recoil loss of ^{37}Ar from these Ca-bearing phases (Fig. 8C; Koppers et al., 2000, 2004; Singer et al., 2019), and due to shock heating in meteorite samples (Cassata et al., 2010, 2011). Progressively older apparent ages in high-temperature steps are often attributed to excess ^{40}Ar in the groundmass or the mineral being analyzed or recoil artifacts (e.g., Heath et al., 2018; Fig. 8D).

The ability to step heat samples is the most important attribute in $^{40}Ar/^{39}Ar$ geochronology because it can potentially evaluate underlying assumptions of the method and identify nonideal behavior. For many samples that have simple thermal and mineralogical histories, the age spectrum commonly reveals multiple steps that are concordant at 2σ, and this set of ages, deemed a plateau, yields acceptable MSWD values. We emphasize that the term "plateau" should be held in the highest regard, as it has the connotation of simple age systematics. It should only be used in cases where previously defined criteria have been met. Unless specifically stated otherwise, plateau ages are model ages that assume the trapped initial argon has an atmospheric composition or an initial composition determined by the inverse isochron approach. Numerous criteria have been put forth to evaluate age spectrum quality and to identify steps that can be combined to calculate a plateau age (e.g., Fleck et al., 1977; Sharp and Renne, 2005; Jourdan et al., 2004). These previously published plateau criteria were based on incremental heating experiments that often consisted of ~5–10 steps. Given the fact that modern incremental heating experiments now consist of many more steps (~15–40; Fig. 8A), we suggest that a plateau

(1) consist of at least five or more consecutive steps that comprise at least >50% of the ^{39}Ar released;
(2) not have a slope (i.e., the majority of consecutive plateau steps do not have ascending or descending ages; Sharp and Renne, 2005); and
(3) have an isochron regressed through all of the plateau steps with a $(^{40}Ar/^{36}Ar)_i$ that is indistinguishable from the atmospheric value at the 95% confidence level (i.e., for terrestrial samples only).

Most incremental heating experiments now yield age spectra showing some level of complexity (Fig. 8). Alternative terms have been used to define data that comprise <50% of the ^{39}Ar released, such as "pseudo-plateau" or "miniplateau." These terms are misleading and must be abandoned because they are too closely associated with the term plateau. In Figures 8A and 8B, the spectra reveal minor amounts of discordance, but in both cases, a plateau is produced consisting of ~65% and >90% of the ^{39}Ar released,

respectively. In Figures 8C and 8D, the incremental heating experiments yielded sloping plateaus that were likely variably affected by a variety of processes, including recoil, fractionation, excess Ar, and/or thermal or chemical alteration of the mineral phases. Age spectra that do not meet nominal plateau criteria may often still contain geologically meaningful information (e.g., reheating/alteration events) and can still be discussed within the context of other geochronologic or stratigraphic data, but they are simply less reliable than their plateau counterparts. For these types of data, it is more appropriate to discuss the age of a sample with a range of dates or use the integrated age with caution.

It has also become more commonplace to take the trapped $(^{40}Ar/^{36}Ar)_i$ intercept from the isochron diagram and use it to recalculate each heating step in an attempt to rectify a partially disturbed spectrum (e.g., Heizler and Harrison, 1988; Heaton and Koppers, 2019). Heath et al. (2018) observed that basaltic lavas with subatmospheric $(^{40}Ar/^{36}Ar)_i$ isochron intercepts sometimes yield erroneously old apparent isochron ages, but more experiments are needed to assess this hypothesis.

For cases where the isochron has a $(^{40}Ar/^{36}Ar)_i$ value greater than and not within 2σ uncertainty of the atmospheric value, the isochron gives the preferred age in most cases. Alternatively, the heating steps that originally defined a plateau can be recalculated using a supra-atmospheric $(^{40}Ar/^{36}Ar)_i$ value instead of the atmospheric ratio (e.g., Heaton and Koppers, 2019), which, if applied correctly, results in a plateau age that is nearly identical to the isochron age within uncertainty, assuming the uncertainty on the $(^{40}Ar/^{36}Ar)_i$ value is correctly propagated.

Interpreting $^{40}Ar/^{39}Ar$ Data Sets for Plutonic and Metamorphic Rocks

Thermochronology—the use of isotopic dates to trace the temperature-time histories of rocks—has become an important component of many tectonic studies (e.g., Reiners and Brandon, 2006; Hodges, 2014). Researchers have found that an abundance of well-calibrated thermochronometers, including those with moderately high closure temperatures like $^{40}Ar/^{39}Ar$, can be coupled with other lower-temperature thermochronometers, e.g., (U-Th)/He or fission track, to offer expanded temperature-time histories.

Closure Temperature Concept

One basic requirement for the $^{40}Ar/^{39}Ar$ date of a mineral to correspond to the crystallization age of that mineral is that the mineral-isotopic system has been closed to the gain or loss of ^{39}K or ^{40}Ar since the time of crystallization. While this requirement is virtually met when cooling is very rapid after crystallization—as is the case for sanidine in an ash-fall tuff or plagioclase in basaltic flows, for example—it is not the case for minerals in slowly cooled plutonic or metamorphic rocks. One of the principal causes of open-system behavior in minerals is the relatively high diffusivity of Ar at the temperatures encountered in the middle and lower crust. If we assume that the dominant process involved in ^{40}Ar loss is volume diffusion (Crank, 1975; Fechtig and Kalbitzer, 1966), then a mineral residing at high temperatures may lose radiogenic ^{40}Ar as rapidly as it is produced by radioactive decay of ^{40}K, but that radiogenic ^{40}Ar is fully retained after the mineral cools sufficiently. In between fully open-system and fully closed-system behavior, there is a period of cooling during which radiogenic ^{40}Ar is only partly retained (Dodson, 1973). For geochronologists, the date we calculate based on $^{40}Ar/^{39}Ar$ analysis of a slowly cooled mineral is neither the crystallization age nor the time of complete system closure but some time intermediate between the two. Dodson (1973, 1979) developed an equation to estimate the temperature of a slowly cooled mineral at the time recorded by a geochronometer, its closure age. Predicated on a model in which cooling was monotonic and linear in inverse temperature, the bulk closure temperature (T_{cb}) is:

$$T_{cb} = \frac{E}{R\ln\left(AD_o RT_{cb}/a^2\, E\left(dT/dt\right)\right)}. \qquad (3)$$

In this equation, A is a constant dependent on the model geometry assumed to best represent ^{40}Ar diffusion in the mineral and approximately equals 55 for radial diffusion in a sphere, 27 for radial diffusion in a cylinder, and 8.7 for diffusion across a plane sheet. Variables D_o and E are terms from the Arrhenius equation that describes diffusivity (D) as a function of temperature, i.e., $D = D_o\exp(-E/RT)$, where E is the activation energy, D_o is a pre-exponential constant equal to D at infinite temperature (T), and R is the universal gas constant. The parameter a represents the effective dimension over which diffusive loss occurs. Finally, dT/dt is the assumed instantaneous cooling rate at the time recorded by the chronometer. This equation cannot be solved analytically for T_{cb}, but it is easily solved iteratively; from an initial estimate for T_{cb}, the equation typically converges on a final result after only a few iterations. An accessible derivation of a slightly different form of Equation 3—with a negative sign before A to account for their preferred use of a negative cooling rate—may be found in Reiners et al. (2018). Table 5 presents notional bulk closure temperatures for a variety $^{40}Ar/^{39}Ar$ chronometers for which experimental diffusion data have been published as calculated from Equation 3, assuming a cooling rate of 10 °C/m.y. (Hodges, 2014). For this table, all closure temperatures were calculated assuming the same effective diffusion dimension of 100 mm and the same cooling rate of 10 °C/m.y. to facilitate comparisons among chronometers.

Calculated values for T_{cb} are significantly dependent on the choice of a and dT/dt. For example, choosing a value of 500 mm instead of 100 mm for hornblende results in a 12% increase in T_{cb} to 570 °C. The dependence of T_{cb} on different values of dT/dt is somewhat less pronounced in most cases; for hornblende, holding a = 100 mm but increasing dT/dt to 50 °C/m.y. (again a fourfold increase) results in only a 6% increase in T_{cb} to 540 °C. However, the dependence of T_{cb} on dT/dt becomes more significant for cooling rates of a few degrees or less per million years, such as those that apparently prevailed in the lower and middle crust of many cratonic regions during their thermal stabilization (e.g., Blackburn et al., 2011; Hodges et al., 1994).

It is especially important to recognize that the most appropriate value of a to use for a particular dated mineral can be ambiguous. Many He and Ar diffusion studies for minerals and empirical observations suggest that half of the physical grain size is commonly the effective diffusion dimension for samples that are devoid of alteration, microfractures, and other potential fast-diffusion pathways (Anderson et al., 2019; Cassata and Renne, 2013; Flude et al., 2014; Hodges and Bowring, 1995; Kula and Spell, 2012; Skipton et al., 2017; Wartho et al., 1999). However, for deformed crystals that contain internal subgrain boundaries that may define fast-diffusion pathways (Lee, 1995) or structurally complex feldspars, a may be substantially smaller than the physical grain size would suggest (Lovera et al., 1989, 1991; Cassata and Renne, 2013). Step-heating experiments on slowly cooled K-feldspars frequently yield complex apparent $^{40}Ar/^{39}Ar$ age spectra, which can be attributed to low-temperature recrystallization (Villa, 2006) and/or the existence of multiple diffusion domains within individual crystals (Lovera et al., 1989; Zeitler, 1987). Both models imply that the nominal closure temperatures for K-feldspars listed in Table 5 are best used with caution when making geologic inferences. A better approach, provided the assumptions of the multidiffusion domain model (MDD) are fulfilled, is to use the $^{40}Ar/^{39}Ar$ step-heating data for each K-feldspar to determine Arrhenius parameters and, in conjunction with inversion of the age spectrum, to infer cooling histories over the temperature range defined by the kinetic parameters (e.g., Harrison et al., 2005; Harrison and Lovera, 2014; Lovera

TABLE 5. NOMINAL BULK CLOSURE TEMPERATURES FOR COMMONLY USED $^{40}Ar/^{39}Ar$ THERMOCHRONOMETERS

Chronometer	D_o (m^2 s^{-1})	E (kJ mol^{-1})	Geometry*	T_{cb}† (°C)	References
Clinopyroxene	1.4×10^{-4}	379	Spherical	730	Cassata et al. (2011)
Orthopyroxene	5.7×10^{-2}	370	Spherical	600	Cassata et al. (2011)
Osumilite	8.3×10^{4}	461	Spherical	580	Blereau et al. (2019)
Hornblende	2.4×10^{-6}	268	Spherical	510	Harrison (1981)
Muscovite	2.0×10^{-3}	264	Spherical	390	Harrison et al. (2009)
Phlogopite	7.5×10^{-5}	242	Cylindrical	390	Giletti (1974)
K-feldspar (anorthoclase)§	4.4×10^{-3}	400	Plane sheet	380	Cassata and Renne (2013)
K-feldspar (sanidine)#	4.5×10^{-5}	220	Spherical	330	Cassata and Renne (2013)
Biotite ($X_{phl} = 0.29$)**	4.0×10^{-5}	211	Cylindrical	320	Grove and Harrison (1996)
Plagioclase (albite/oligoclase)††	3.1×10^{-5}	209	Spherical	310	Cassata and Renne (2013)
K-feldspar (cryptoperthite)	3.7×10^{-6}	197	Spherical	300	Wartho et al. (1999)
Plagioclase (anorthite)§§	2.2×10^{-6}	196	Spherical	300	Cassata and Renne (2013)
Biotite ($X_{phl} = 0.46$)**	1.5×10^{-6}	186	Cylindrical	290	Grove and Harrison (1996)
K-feldspar (orthoclase)	9.8×10^{-7}	183	Spherical	280	Foland (1994)

*Represents an assumed diffusion geometry, with consequences for the choice of *a*. See text.
†Calculated assuming $a = 100$ µm and $dT/dt = 10$ °C/m.y. and rounded to the nearest 10 °C.
§Easy Chair Crater, Nevada, sample ECCa-3 in Cassata and Renne (2013).
#Fish Canyon Tuff, Colorado, sample FCs-2 in Cassata and Renne (2013).
**X_{phl} refers to the mole fraction of phlogopite in the biotite solid solution.
††Plutonic achondrite GRA 06128, sample GRAp-1 in Cassata and Renne (2013).
§§Lunar anorthosite 76535, sample TROCp-1 in Cassata and Renne (2013).

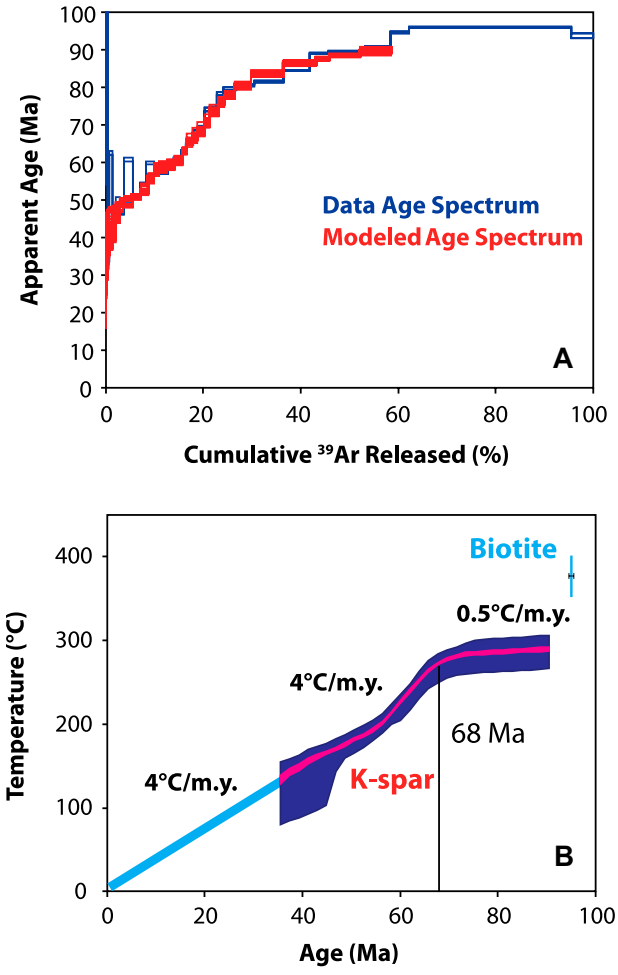

Figure 9. (A) Down-stepping K-feldspar $^{40}Ar/^{39}Ar$ age spectra (blue) from a granitoid sample (01KIM) in the Alaska Range along with modeled age spectra (red) produced using the software of Lovera et al. (2002) indicating a prolonged and complex thermal history. (B) Cooling history of sample 01K1 M from multidiffusion domain model (MDD) thermal models generated from K-feldspar and biotite (94.8 ± 0.5 Ma) using the software of Lovera et al. (2002). The MDD magenta band is the 90% confidence interval of the mean, and the purple band is the 90% confidence of the distribution. The light blue line is a projection of the long-term cooling rate past the closure temperature of K-feldspar to the 0 °C intercept. The MDD thermal model from sample 01KIM demonstrates slow prolonged cooling starting at about 68 Ma at a long-term rate of approximately 6 °C/m.y. until around 52 Ma, when average cooling rate is slightly slower at 3.4 °C/m.y. through Ar closure. Figures and data are from Benowitz et al. (2014).

et al., 1991). MDD K-feldspar thermochronology has proven to be useful for examining a broad range of tectonic questions because of (1) the wide Ar closure-temperature window (~150–350 °C) of the system, and (2) the ability to use computational modeling to understand the rate of rock cooling and/or reheating within this temperature range. Temperature must be monitored during step-heating experiments in order to retrieve the ^{39}Ar diffusion characteristics to apply in the diffusion models and to model thermal histories (Fig. 9; Lovera et al., 1993). Traditionally, diffusion experiments have been performed with a double-vacuum resistance furnace, but recently, step heating of samples has been performed using a laser with a thermocouple or optical pyrometer for temperature control (Idleman et al., 2018). There is ongoing debate on the geologic significance of K-feldspar $^{40}Ar/^{39}Ar$ release patterns (Parsons et al., 1999; Villa and Hanchar, 2013). However, it is clear from numerous applications of MDD K-feldspar thermochronology to structural problems (Batt et al., 2004; Benowitz et al., 2011), including comparisons to other thermochronometers from the same rock sample (McDannell et al., 2019), that MDD results can provide very robust regional thermal constraints. A relatively new finding that appears to show great promise for $^{40}Ar/^{39}Ar$ thermochronometry is to extend MDD-style analyses to muscovite (Harrison and Lovera, 2014; Long et al., 2018). The challenge towards taking advantage of this potential opportunity is to demonstrate that the metastability of muscovite in the temperature range of the laboratory degassing experiment does not impact negatively on determining geologically relevant diffusion parameters. Similarly, determination of diffusion parameters and closure temperatures for hydrothermal and supergene alunite may extend the use of thermochronology to sulfates in hydrothermal systems and metamorphic terrains (Ren et al., 2019).

Geologic Interpretations of Single-Crystal Dates Based on ^{40}Ar Diffusive Behavior in Minerals

While uncertainties regarding the most appropriate values to use for *a* and *dT/dt*, as well as the multiple domain diffusion behavior in certain samples, argue against the rigid assignment of an intrinsic T_{cb} to specific geochronometers, nominal values are useful guides to the interpretation of $^{40}Ar/^{39}Ar$ dates. For example, a $^{40}Ar/^{39}Ar$ date for a muscovite that crystallized as part of a prograde, amphibolite-facies metamorphic assemblage in a schist is not interpreted by this approach as the age of prograde metamorphism but instead as the approximate time of cooling of that crystal through conditions of roughly 390 °C. On the other hand, a $^{40}Ar/^{39}Ar$ date for a muscovite that grew at temperatures of ~390 °C—maximum metamorphic conditions for many greenschist-facies samples—might be reasonably interpreted as the approximate age of muscovite crystallization and, by extension, greenschist-facies metamorphism.

The $^{40}Ar/^{39}Ar$ chronometers in Table 5 are listed in order of descending closure temperature and thus the retentivity of radiogenic ^{40}Ar in several important rock-forming minerals. This order suggests how $^{40}Ar/^{39}Ar$ data for

different minerals might be particularly useful for specific geologic applications. For example, $^{40}Ar/^{39}Ar$ thermochronometers have traditionally been of limited use in studies of the high-temperature cooling paths of granulite-facies metamorphic terranes because the notional closure temperatures of $^{40}Ar/^{39}Ar$ thermochronometers are several hundred degrees lower than peak granulite-facies conditions. However, experimental ^{40}Ar diffusion data for pyroxenes (Cassata et al., 2011) imply high notional closure temperatures: 730 °C for clinopyroxene and 600 °C for orthopyroxene. Thus, as noted by Ware and Jourdan (2018), $^{40}Ar/^{39}Ar$ thermochronometry of pyroxenes may yield improved constraints on the temperature-time evolution of exhumed granulite-facies rocks. The same could be said for $^{40}Ar/^{39}Ar$ thermochronometry of the rare cyclosilicate mineral osumilite (Blereau et al., 2019), which can be found in some Mg-rich, granulite-facies metapelites, given that its closure temperature is similar to that of orthopyroxene. Detailed temperature-time paths for eclogite-facies terranes may also be improved through $^{40}Ar/^{39}Ar$ thermochronometry of pyroxenes found in mafic eclogites. A complication that arises with $^{40}Ar/^{39}Ar$ dates for minerals with high closure temperature such as pyroxene is that they can pass through multiple orogenic heating episodes without being fully outgassed, even though the peak temperature exceeds the nominal closure temperature. This phenomenon is illustrated by ages for the mica phengite in ultrahigh-pressure, low-temperature blueschists. Warren et al. (2012a, 2012b) modelled argon loss during short orogenic cycles at subduction zones, showing that it was unlikely that phengites would yield cooling ages, but they would likely retain mixed ages reflecting both prograde and retrograde paths. The same is likely to be true of pyroxene $^{40}Ar/^{39}Ar$ ages, and attention must be paid to the full thermal history of the rocks.

For many years, the hornblende $^{40}Ar/^{39}Ar$ chronometer has been used extensively to constrain ages of amphibolite-facies metamorphic events due to its relatively high closure temperature. In many studies, $^{40}Ar/^{39}Ar$ dates serve as medium-temperature anchors for low-temperature cooling histories constrained by $^{40}Ar/^{39}Ar$ mica and feldspar data, as well as (U-Th)/He and fission-track accessory mineral data. In principle, having so many $^{40}Ar/^{39}Ar$ chronometers with closure temperature estimates ranging between 300 and 400 °C (Table 5) offers the opportunity to combine their use to develop close constraints on the cooling histories of samples over that temperature interval. However, such "multichronometric" studies using $^{40}Ar/^{39}Ar$ chronometers alone are unlikely to yield satisfactory results; even if we knew values for a and dT/dt a priori, uncertainties in the diffusion parameters D_o and E based on experimental data sets are so large that they propagate into practical uncertainties in T_{cb} values of ±50 °C or more, leading to highly uncertain estimated temperature-time histories across such a narrow temperature interval. Better success comes from the integration of $^{40}Ar/^{39}Ar$ chronometers with (U-Th)/Pb, (U-Th)/He, and fission-track thermochronometers and thus the temperature range of an estimated temperature-time path. For example, a typical granodiorite sample might contain hornblende, biotite, K-feldspar, and plagioclase that can be dated using the $^{40}Ar/^{39}Ar$ method, but also zircon, titanite, and apatite—minerals amenable to (U-Th)/Pb, (U-Th)/He, and fission-track geochronology and thermochronology. Together, these chronometers would permit detailed tracing of the thermal history of a single granodiorite sample from the time of its emplacement to temperature of ~70 °C (Hodges, 2014).

Geologic Insights from Laser Microprobe Dating of Individual Crystals

While many earth scientists understand the utility of $^{40}Ar/^{39}Ar$ dates for thermochronology, fewer appreciate that slowly cooled K-bearing crystals are likely to preserve intracrystalline ^{40}Ar diffusive loss profiles that can be used to model temperature-time paths (Hodges, 2014). Dodson (1986) showed that different positions within a cooling crystal that acts as a single diffusion domain have coordinate-specific closure temperatures different from the bulk closure temperature of the whole crystal. Dodson (1986) went on to derive an equation similar to Equation 3 with which to calculate position-dependent closure temperatures.

Studies such as those by Phillips and Onstott (1988) and Kelley and Turner (1991) have demonstrated the possibility of resolving diffusive loss profiles in minerals using a focused laser. For example, Kelley and Turner (1991) showed that hornblende grains found in the Giants Range Granite of northern Minnesota in the United States had lost Ar as a consequence of reheating due to the intrusion of a much younger gabbro nearby. The existence of "closure profiles" in slowly cooled minerals as predicted by Dodson (1986) was confirmed a few years later through laser spot fusion studies of (001) cleavage surfaces in slowly cooled micas from the New England Appalachians and the Proterozoic orogen of the southwestern United States (Hames and Hodges, 1993; Hodges and Bowring, 1995; Hodges et al., 1994). The results were used to make general inferences about the cooling histories of the micas over the core-to-rim closure interval. However, detailed mapping of intracrystalline ^{40}Ar distributions was not possible with the laser technologies used because of collateral heating of the sample outside the laser target area. A major advancement in spatial resolution accompanied the development of UVLAMP facilities (Kelley et al., 1994). With increasing use of ultraviolet lasers for very high-resolution apparent-age mapping, it is possible to build more detailed models of cooling histories, while also learning the limitations of conventional thermochronology. For example, while classical thermochronology is predicated on the notion that the region surrounding a crystal is essentially an infinite sink for ^{40}Ar lost from a sample by diffusion, many studies—particularly studies of polymetamorphic samples—are now finding clear evidence for inward diffusion of excess ^{40}Ar along crystal margins (e.g., McDonald et al., 2018; Pickles et al., 1997; Warren et al., 2011, 2012b). Laser microprobe studies are confirming that other processes in nature, such as thermally activated volume diffusion, recrystallization due to changing thermal regimes, deformation, partial melting, and hydrothermal alteration, influence dates recorded by individual minerals collected from orogenic systems (e.g., Cosca et al., 2011; McDonald et al., 2016; Mulch et al., 2005; Mulch and Cosca, 2004; Putlitz et al., 2005; Warren et al., 2012a).

$^{40}Ar/^{39}Ar$ Provenance Studies using Detrital Minerals

$^{40}Ar/^{39}Ar$ geochronology and thermochronology method on detrital minerals has been used for decades to constrain maximum deposition ages (MDA), sediment provenance, and sedimentary basin thermal histories (Harrison and Be, 1983; Renne et al., 1990; Copeland and Harrison, 1990; Heizler and Harrison, 1991; Pierce et al., 2014; Mulder et al., 2017; Benowitz et al., 2019). Until recently, data collection for these detrital mineral studies was time- consuming because of the slow data acquisition on single-collector mass spectrometers. With the augmentation of multicollector instruments that provide rapid analyses at high precision, detrital mineral studies using the $^{40}Ar/^{39}Ar$ method now have tremendous potential. For the more widely applied U-Pb detrital zircon chronometer, there are at least 10 different methods used to calculated MDAs, which vary in accuracy depending on age population sample size and the controlling geologic process (e.g., tectonic or sedimentary). For a recent detailed review of MDA determinations, see Coutts et al. (2019).

In general, there is no uniform method to calculate an MDA for all data sets, and thus a

case-by-case approach seems warranted. Multiple individual detrital dates that form discrete age populations are always desirable, but they are not necessarily required. A low *n* population can hold valuable and robust MDA and provenance information and should not be discounted based solely on the number of analyses.

Detrital Hornblende $^{40}Ar/^{39}Ar$ for Studies of Iceberg Deposits

Because of their relatively common occurrence in many crystalline and volcanic rocks, the $^{40}Ar/^{39}Ar$ ages of individual detrital hornblende grains in marine sediment cores offshore from current and past ice sheets can provide powerful constraints on the locations from which icebergs calved off ice-sheet margins, and thus they can provide evidence for unstable sectors of past ice sheets. Several studies have used this approach both in the North Atlantic region (for an overview, see Hemming, 2004) and around Antarctica. Uncertainties about how debris gets incorporated into flowing ice and transported, as well as about processes near the terminus of the ice sheet, mean that the interpretations of ice-sheet history from this approach are qualitative. (The processes and approaches to studying glacigenic sediments in Antarctica were reviewed by Licht and Hemming [2017] and Cook et al. [2017].) However, the occurrence of large amounts of ice-rafted detritus (IRD) with provenance requiring long-distance transport requires the coincidence of dramatic iceberg production, extreme sediment entrainment, and increased winds and surface current velocities to move the icebergs more quickly, or cold currents to limit iceberg melting (Cook et al., 2014). All these factors that enhance the abundance of IRD in marine sediments are climate sensitive.

An example of the application of $^{40}Ar/^{39}Ar$ detrital hornblende provenance from Antarctica comes from Ocean Drilling Program (ODP) Site 1165 off Prydz Bay (Fig. 10). A survey of proximal sediment cores around Antarctica (Fig. 10) revealed that there is a distinctive age range on the Wilkes Land margin (the Australian conjugate margin to Antarctica; Roy et al., 2007; Pierce et al., 2011, 2014). At Site 1165, variability in the proportion of locally derived ca. 500 Ma hornblendes and distantly derived ca. 1200 Ma hornblendes (Cook et al., 2014) revealed episodes of large increases of icebergs from the Wilkes Land margin (Williams et al., 2010; Cook et al., 2014) in the late Pliocene. Further, the $^{40}Ar/^{39}Ar$ ages of hornblende and biotite from dropstones found in the Miocene section of Site 1165 also revealed significant occurrences of Wilkes Land–derived icebergs (Pierce et al., 2014).

Detrital Sanidine $^{40}Ar/^{39}Ar$ Studies

Detrital sanidine geochronology has the potential for utilization for many Phanerozoic sedimentary deposits (Copeland and Harrison, 1990; Chetel et al., 2011). Recent applications have mostly focused on Paleocene/Late Cretaceous chronostratigraphic studies and river terrace dating in the southwest United States (Hereford et al., 2016; Karlstrom et al., 2017; Leslie et al., 2018a, 2018b; Aslan et al., 2019; Walk et al., 2019). The power of the method lies in the robustness of sanidine to produce ultraprecise and accurate dates by single-crystal total fusion. Additionally, high throughput is accomplished by multicollection mass spectrometry, where about 200 grains can be dated in ~24 h. This does not reach the throughput of detrital zircon analyses, but sanidine dates are typically 100× more precise than detrital zircon dates, allowing discrete identification of source calderas (e.g., Hereford et al., 2016; Karlstrom et al., 2017). By specifically choosing the sanidine from the bulk K-feldspar population, the chances of finding grains that are subequal to sediment deposition ages are greatly enhanced, especially compared to detrital zircons that are recycled multiple times from older rocks into younger sediments. These young sanidine populations found in terrace deposits of western U.S. river systems are the result of numerous large and young volcanic systems such as Yellowstone and Long Valley. The fact that silicic volcanism has occurred nearly continuously in the western United States during the Cenozoic bodes well for finding juvenile sanidines in most Cenozoic sedimentary rocks and thus makes detrital sanidine $^{40}Ar/^{39}Ar$ dating a potential breakthrough method for chronostratigraphic studies in volcanically active areas. Additionally, Paleozoic and Mesozoic sanidine is found in young sedimentary rocks and thus indicates great potential to apply detrital sanidine geochronology to older systems.

Detrital Mica $^{40}Ar/^{39}Ar$ Studies

$^{40}Ar/^{39}Ar$ dating studies of individual detrital white mica grains are commonly used to track sediment transport during active mountain building. Their resistance to grain-size reduction during erosion and transport, and their platy shapes, which enhance their transport in rivers, have led to their use in provenance studies. Individual grain $^{40}Ar/^{39}Ar$ ages record both midcrustal closure ages (e.g., Carrapa et al., 2003) and (when combined with the age of the enclosing sediment) lag time, indicative of the speed of sediment transport from erosive source to final deposition site (e.g., Szulc et al., 2006). Although the approach is not new (Kelley and Bluck, 1992), it became more commonly used when automated laser systems were able to measure the $^{40}Ar/^{39}Ar$ ages of tens to hundreds of individual grains. The measurements are commonly combined with geochronology of other detrital minerals such as U/Pb of zircon and rutile and apatite fission-track dating (e.g., Najman et al., 2019) to provide an integrated and powerful approach to understanding sediment transport and active orogenic processes.

$^{40}Ar/^{39}Ar$ of Low-Temperature Processes

$^{40}Ar/^{39}Ar$ geochronologic analysis of minerals formed at low temperatures can provide age constraints on the formation of soils, weathering profiles, and caves (e.g., Polyak et al., 1998); it can also provide age/rate constraints on landscape evolution (Vasconcelos et al., 1992; Vasconcelos, 1999) along with shallow-crustal faulting (e.g., van der Pluijm et al., 2001; Yun et al., 2010; van der Pluijm and Hall, 2015) and the timing of mineralization (Harbi et al., 2018).

Fault activity dating relies on analysis of either bulk aliquots of the clay gouge (e.g., illite) from fault rocks (e.g., van der Pluijm and Hall, 2015, and references therein), in situ measurement of fault-zone vein material such as pseudotachylyte (e.g., Kelley et al., 1994) or low-temperature strain fringes (e.g., Sherlock et al., 2003), or precipitated and/or recrystallized minerals during fault fluid flow (Davids et al., 2018). Fault gouge clay is thought to be a mixture of two populations: a detrital ($2M_1$ polytype) wall-rock population, and an authigenic (1 M or $1M_D$ polytype) population formed in the brittle zone coeval with faulting (Vrolijk and van der Pluijm, 1999; Yan et al., 2001; Haines and van der Pluijm, 2008). Distinction between these two populations is achieved by separating clay gouge into three of four size fractions (<0.02 µm to <2 µm) and analyzing each by X-ray diffraction to determine the crystalline size and diagenetic grade (Środoń, 1980; Reynolds and Reynolds, 1996). Either K-Ar or encapsulated $^{40}Ar/^{39}Ar$ analysis is subsequently performed on each aliquot, with the resulting ages forming a mixing line between the fine-grained authigenic population (i.e., the age of the fault) and the relatively coarser detrital population (Fig. 11). This method, called the illite age analysis (IAA), has been routinely applied to clay gouge of brittle fault rocks (e.g., van der Pluijm and Hall, 2015) along with hydrothermally produced clay (Hall et al., 1997, 2000). For detailed reviews of K-Ar and $^{40}Ar/^{39}Ar$ dating of clay minerals see Clauer et al. (2012) and Clauer (2013). Low-temperature minerals may be very fine grained (micro- to cryptocrystalline) with average grain thicknesses far smaller than the average recoil distance (Turner and Cadogan, 1974; Onstott et al., 1995). This makes

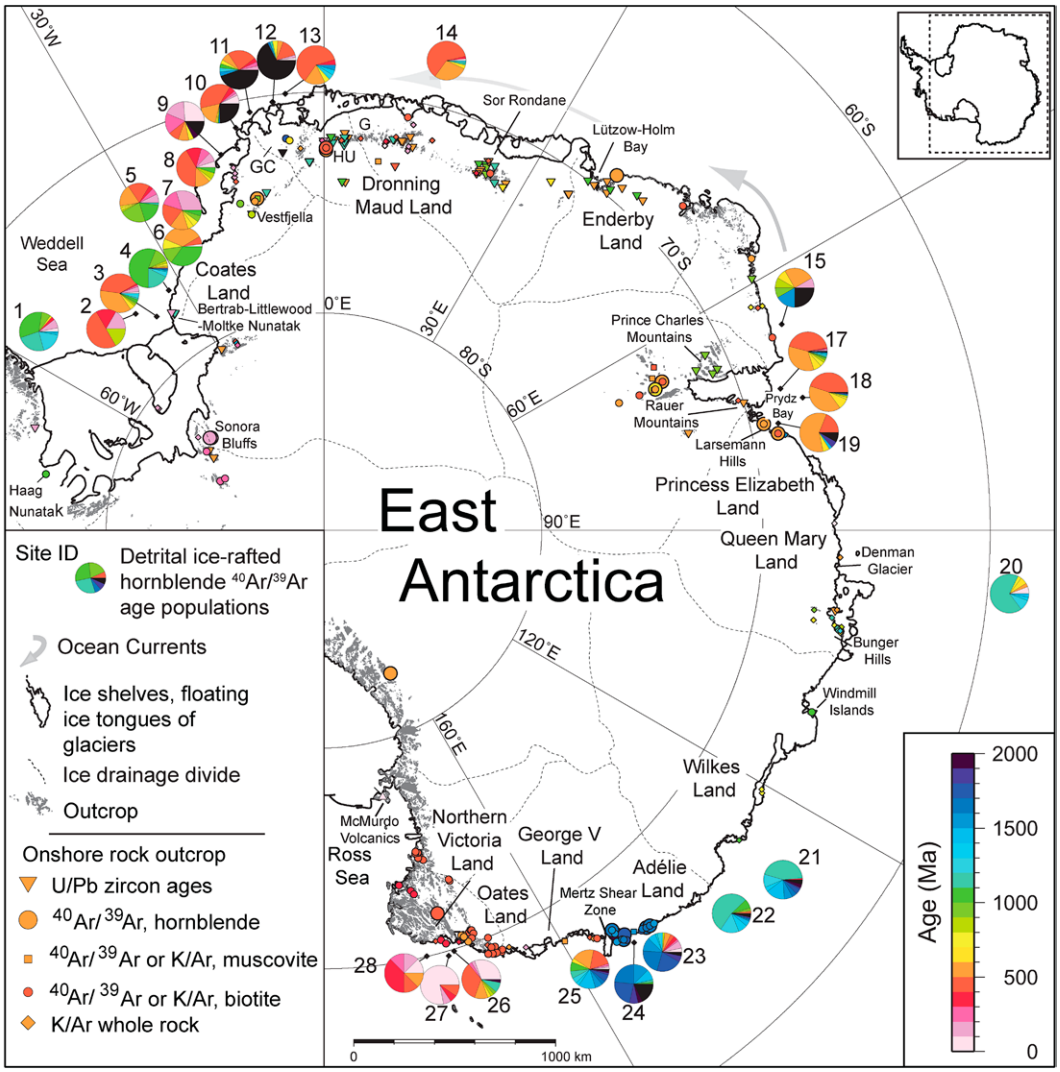

Figure 10. $^{40}Ar/^{39}Ar$ hornblende ice-rafted debris maps of East Antarctica with pie charts showing the distribution of thermochronologic ages by site location along with known onshore ages (modified from Pierce et al., 2014). The color scale corresponds to 100 m.y. increments of time. GC—Grunehogna craton, G—Gjelsvikfjella, H—Haag Nunatak, HU—H.U. Sverdrupfjella, K—Kirwanveggan.

quantification of potential ^{39}Ar and ^{37}Ar recoil from these phases extremely important, as up to 30% ^{39}Ar loss is possible (Hall, 2014). In fine-grained clay minerals, the inevitability of recoil is overcome by encapsulating samples in evacuated fused silica vials prior to irradiation. After irradiation, vials are then cracked or lased within an ultrahigh-vacuum system, and the recoil-lost Ar can be accounted for by mass spectrometry analysis prior to incremental heating of the sample (Hess and Lippolt, 1986; Foland et al., 1992; Smith et al., 1993; Onstott et al., 1995).

Weathering geochronology relies primarily on incremental heating $^{40}Ar/^{39}Ar$ dating of K-bearing Mn oxides, particularly cryptomelane and hollandite, and the alunite-group sulfates alunite and jarosite (Vasconcelos, 1999). The $^{40}Ar/^{39}Ar$ geochronologic method applied to weathering minerals faces some of the same challenges encountered in other applications of the $^{40}Ar/^{39}Ar$ method, such as partial argon loss by diffusion or alteration, extraneous argon hosted in mineral contaminants, etc. Weathering geochronology, however, also suffers from a series of challenges particular to the application. For example, some supergene minerals, such as Mn oxides, may form by colloform growth, where fine-scale (~20-µm-wide) mineral layers precipitate concentrically and progressively through time. A single 1 mm fragment of cryptomelane may contain 50 distinct mineral precipitation events, spanning in excess of 1 m.y. (Vasconcelos et al., 1992; Hénocke et al., 1998). Incremental heating analysis of these phases invariably produces ascending or descending apparent age spectra, depending on the relative Ar retentivity of the various growth bands. Improvements in mass spectrometry make these age progressions more noticeable, and suitable analytical and statistical approaches for retrieving mineral precipitation ages from these phases are required. For example, in situ dating with laser microprobes may resolve ages of precipitation at the microband scale. Minerals precipitated at low temperatures may also be extremely fine grained and suffer from the recoil effects discussed above, and so quantification of potential losses is necessary (Ren and Vasconcelos, 2019a). Finally, minerals generated by low-temperature water-rock interaction may persist on the surface of Earth (e.g., Landis et al., 2005) or Mars for protracted periods of time. Measurements of diffusion parameters and closure temperatures for these phases are needed to determine if they can indeed remain closed to Ar at surface temperatures at billion-year time scales (Kula and Baldwin, 2011; Ren and Vasconcelos, 2019b). Challenges in determining diffusion parameters for hydrous phases include a lack of information on their thermal behavior during heating in vacuum (Gaber et al., 1988; Lee et al., 1991) and the possibility that Ar is released during phase transformation and not by volume diffusion (Vasconcelos et al., 1995). Combining high-resolution $^{40}Ar/^{39}Ar$ geochronology with mineralogical approaches suitable for studying mineral transformation permits the

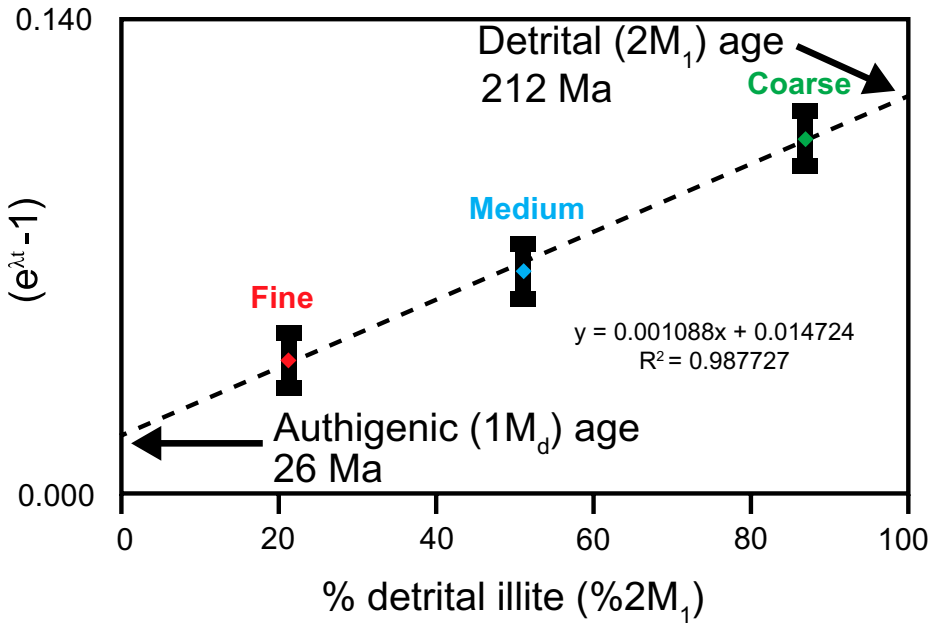

Figure 11. Percentage of detrital illite (2M1) plotted against the $^{40}Ar/^{39}Ar$ age (modified from Haines and van der Pluijm, 2008). The percentage detrital illite is linearly related to the exponential decay of potassium ($e^{\lambda}t$ – 1) rather than chronological time.

mechanisms of Ar release to be determined and the temperature windows when volume diffusion controls noble-gas release to be identified (Ren and Vasconcelos, 2019b).

REMAINING CHALLENGES AND FUTURE DIRECTIONS IN $^{40}Ar/^{39}Ar$ GEOCHRONOLOGY

The impact of the improved sensitivity and/or higher mass resolution of multicollector mass spectrometers has been overwhelmingly positive for $^{40}Ar/^{39}Ar$ geochronology. However, with higher precision come new challenges. As noted in the previous sections, numerous recent $^{40}Ar/^{39}Ar$ studies of volcanic sanidine and other K-bearing minerals have yielded a large range in dates with overdispersion akin to that observed in many U-Pb zircon studies. To fully understand the sources of the overdispersion in $^{40}Ar/^{39}Ar$ dates, to improve the accuracy of the $^{40}Ar/^{39}Ar$ method, and to make more informed decisions regarding the age of a sample, developments must be made in the following areas:

(1) Nuclear reactions: Part of the overdispersion in $^{40}Ar/^{39}Ar$ dates is likely linked to processes that occur in the reactor during irradiation. Studies similar to those of Rutte et al. (2015, 2019), which are focused on careful characterization of fluence gradients, the effects of self-shielding, and interfering reactions, are highly desirable. It is important to better understand how each of these parameters changes as a function of irradiation time and position in the reactor.

(2) Calibration: The accuracy of $^{40}Ar/^{39}Ar$ dating is ultimately limited by uncertainties in the ^{40}K decay constants and the isotopic composition of standards. These two variables are often collectively conflated with the ages of standards, which are dependent on both. Efforts to improve these sources of uncertainty are ongoing, including the intercalibration with the U/Pb system as described by Renne et al. (2010, 2011). An ongoing effort aims to populate a so-called *R*-matrix (e.g., Niespolo et al, 2017), consisting of intercalibration factors between standards defining a geometric age progression. Plans to populate an *R*-matrix in conjunction with an initiative to improve the intercalibration approach of Renne et al. (2010, 2011), involving multiple $^{40}Ar/^{39}Ar$ and U/Pb laboratories, were adopted at an Earthrates workshop in 2018, and this work is ongoing as of this writing.

(3) Ar diffusion kinetics: As noted by Reiners et al. (2018), one of the remaining challenges for $^{40}Ar/^{39}Ar$ geochronology is to improve our understanding of the mechanism(s) for incorporation, uptake, and retention of both radiogenic and nonradiogenic Ar by various materials. Andersen et al. (2017) suggested that production of $^{40}Ar^*$ in sanidine may outpace diffusive loss in a magma at temperatures less than 475 °C, and that crystals stored at 600 °C could retain pre-eruption ages for several millennia. However, these suggestions were based on theoretical modelling. Additional studies of Ar inheritance/uptake (e.g., Singer et al., 1998; Renne et al., 2012) on a variety of K-bearing minerals are needed to address this issue.

(4) $^{40}Ar/^{39}Ar$ petrochronology: Petrochronology is broadly defined as the pairing of isotopic dates with complementary morphological, elemental, or isotopic data from the same volume of sample aliquot (e.g., Schoene et al., 2010; Kylander-Clark et al., 2013, Kohn et al., 2017). The coupled compositional data can further improve the understanding (e.g., petrologic fingerprinting, robust filtering of antecrysts) of isotopic dates, allowing for more advanced age interpretations. One of the most widely employed minerals utilized in U/Pb petrochronology is zircon, because it can persist through multiple igneous events spanning a wide range of pressures and temperatures, and it often grows in response to changes in these parameters. Although more challenging for noble gases, comparable petrochronologic approaches could be employed on K-bearing minerals for $^{40}Ar/^{39}Ar$ analysis (e.g., Ellis et al., 2017).

(5) $^{40}Ar/^{39}Ar$ analysis of nontraditional phases: Recent advances in our understanding of ^{40}Ar diffusion in minerals not traditionally used in $^{40}Ar/^{39}Ar$ chronometry, coupled with analytical advances that permit analysis of minerals that are poor in potassium, are rapidly expanding the spectrum of geologic questions that can be addressed. For example, ^{40}Ar diffusion data for pyroxenes (Cassata et al., 2011) provide new opportunities to use these minerals for the $^{40}Ar/^{39}Ar$ dating of mafic and ultramafic rocks (Ware and Jourdan, 2018; Konrad et al., 2019; Zi et al., 2019) and may provide more robust indications of the crystallization ages for weakly metamorphosed or hydrothermally altered samples than more familiar $^{40}Ar/^{39}Ar$ chronometers. The $^{40}Ar/^{39}Ar$ analyses of K-rich metasomatic and hydrothermal alteration phases (e.g., alunite, jarosite; Vasconcelos et al., 1994; Ren and Vasconcelos, 2019b) and $^{40}Ar/^{39}Ar$ dating of fluid inclusions via mechanical crushing (e.g., Xiao et al 2019) have become more commonplace.

CONCLUDING REMARKS

The abundance of potassium in Earth's crust (several weight percent) makes a large variety of rock-forming K-bearing phases suitable for $^{40}Ar/^{39}Ar$ dating, continuing to ensure the versatility and relevance of this dating technique to a broad range of geologic disciplines. The diversity of data sets produced, and the variety of applications utilized in $^{40}Ar/^{39}Ar$ geochronology are dependent on the geologic question of interest, leading to different approaches and methods of data interpretation. In this contribution, we

have highlighted strategies for the interpretation of several different types of $^{40}Ar/^{39}Ar$ data sets that will continue to evolve as analytical techniques become more advanced. To ensure that both $^{40}Ar/^{39}Ar$ specialists and a variety of end-users can fully evaluate $^{40}Ar/^{39}Ar$ data sets, the full spectrum of isotopic abundance measurements, analytical procedures, monitor ages and constant values, metadata, and geologic context are required to be reported by FAIR standards. Compliance of $^{40}Ar/^{39}Ar$ data sets to the FAIR principles requires community agreement about (1) a common language with which to describe the data, and (2) a common file format that is readable by both humans and computers. In this contribution, we deliver both with the guidelines set forth in Table 4 (see also Supplementary Material DR1). Thus, $^{40}Ar/^{39}Ar$ data maintain viability and longevity both within and outside the literature, enabling interdisciplinary usage and more robust science.

ACKNOWLEDGMENTS

This work was funded in part by a National Science Foundation EARTHCUBE grant, EAR-1740694. Any use of trade, firm, or product names is for descriptive purposes only and does not imply endorsement by the U.S. government. We appreciate constructive comments from Bob Fleck, Jim Ogg, and one anonymous reviewer.

REFERENCES CITED

Alexander, Jr., E.C., and Davis, P.K., 1974, ^{40}Ar-^{39}Ar ages and trace element contents of *Apollo 14* breccias; an interlaboratory cross-calibration of ^{40}Ar-^{39}Ar standards: Geochimica et Cosmochimica Acta, v. 38, p. 911–928, https://doi.org/10.1016/0016-7037(74)90064-7.

Amrhein, V., Greenland, S., and McShane, B., 2019, Retire statistical significance: Nature, v. 567, p. 305–307, https://doi.org/10.1302/0301-620x.101b10.bjj-2019-0890.

Andersen, N.L., Jicha, B.R., Singer, B.S., and Hildreth, W., 2017, Incremental heating of Bishop Tuff sanidine reveals pre-eruptive radiogenic Ar and rapid remobilization from cold magma storage: Proceedings of the National Academy of Science, v. 114, no. 47, p. 12407–12412, https://doi.org/10.1073/pnas.1709581114.

Anderson, A.J., Hodges, K.V., van Soest, M.C., and Hanchar, J.M., 2019, Helium diffusion in natural xenotime: Geochemistry, Geophysics, Geosystems, v. 20, p. 417–433, https://doi.org/10.1029/2018GC007849.

Aslan, A., Karlstrom, K.E., Kirby, E., Heizler, M.T., Granger, D.E., Feathers, J.K., Hanson, P.R., and Mahan, S.A., 2019, Resolving time-space histories of late Cenozoic bedrock incision along the Upper Colorado River, USA: Geomorphology, v. 347, 106855, https://doi.org/10.1016/j.geomorph.2019.106855.

Balbas, A., Koppers, A.A.P., Kent, D. V., Konrad, K., and Clark, P.U., 2016, Identification of the short-lived Santa Rosa geomagnetic excursion in lavas on Floreana Island (Galapagos) by $^{40}Ar/^{39}Ar$ geochronology: Geology, v. 44, p. 359–362, https://doi.org/10.1130/G37569.1.

Batt, G.E., Baldwin, S.L., Cottam, M.A., Fitzgerald, P.G., Brandon, M.T. and Spell, T.L., 2004, Cenozoic plate boundary evolution in the South Island of New Zealand: New thermochronological constraints: Tectonics, v. 23, no. 4, TC4001, https://doi.org/10.1029/2003TC001527.

Beckinsale, R.D., and Gale, N.H., 1969, A reappraisal of decay constants and branching ratio of ^{40}K: Earth and Planetary Science Letters, v. 6, p. 289–294, https://doi.org/10.1016/0012-821X(69)90170-8.

Begemann, F., Ludwig, K.R., Lugmair, G.W., Min, K., Nyquist, L.E., Patchett, P.J., Renne, P.R., Shih, C.-Y., Villa, I.M., and Walker, R.J., 2001, Call for an improved set of decay constants for geochronological use: Geochimica et Cosmochimica Acta, v. 65, no. 1, p. 111–121, https://doi.org/10.1016/S0016-7037(00)00512-3.

Benowitz, J.A., Layer, P.W., Armstrong, P., Perry, S.E., Haeussler, P.J., Fitzgerald, P.G., and VanLaningham, S., 2011, Spatial variations in focused exhumation along a continental-scale strike-slip fault: The Denali fault of the eastern Alaska Range: Geosphere, v. 7, no. 2, p. 455–467, https://doi.org/10.1130/GES00589.1.

Benowitz, J.A., Layer, P.W., and Vanlaningham, S., 2014, Persistent long-term (c. 24 Ma) exhumation in the eastern Alaska Range constrained by stacked thermochronology, *in* Jourdan, F., Mark, D.F., and Verati, C., eds., Advances in $^{40}Ar/^{39}Ar$ Dating: From Archaeology to Planetary Sciences: Geological Society [London] Special Publication 378, p. 225–243, https://doi.org/10.1144/SP378.12.

Benowitz, J.A., Davis, K., and Roeske, S., 2019, A river runs through it both ways across time: $^{40}Ar/^{39}Ar$ detrital and bedrock muscovite geochronology constraints on the Neogene paleodrainage history of the Nenana River system, Alaska Range: Geosphere, v. 15, p. 682–701, https://doi.org/10.1130/GES01673.1.

Blackburn, T., Bowring, S.A., Schoene, B., Mahan, K., and Dudas, F., 2011, U-Pb thermochronology: Creating a temporal record of lithosphere thermal evolution: Contributions to Mineralogy and Petrology, v. 162, no. 3, p. 479–500, https://doi.org/10.1007/s00410-011-0607-6.

Blereau, E., Clark, C., Jourdan, F., Johnson, T.E., Taylor, R.J.M., Kinny, P.D., Danišík, M., Hand, M., and Eroglu, E., 2019, Closed system behaviour of argon in osumilite records protracted high-T metamorphism within the Rogaland–Vest Agder sector, Norway: Journal of Metamorphic Geology, v. 37, no. 5, p. 667–680, https://doi.org/10.1111/jmg.12480.

Blewett, S.C.J., Phillips, D., and Matchan, E.L., 2019, Provenance of Cape Supergroup sediments and timing of Cape Fold Belt orogenesis: Constraints from high-precision $^{40}Ar/^{39}Ar$ dating of muscovite: Gondwana Research, v. 70, p. 201–221, https://doi.org/10.1016/j.gr.2019.01.009.

Bogard, D.D., and Garrison, D.H., 1999, Argon-39–argon-40 "ages" and trapped argon in Martian shergottites, Chassigny, and Allan Hills 84001: Meteoritics & Planetary Science, v. 34, p. 451–473, https://doi.org/10.1111/j.1945-5100.1999.tb01353.x.

Bogard, D.D., and Johnson, P., 1983, Martian gases in an Antarctic meteorite?: Science, v. 221, p. 651–654, https://doi.org/10.1126/science.221.4611.651.

Carrapa, B., Wijbrans, J., and Bertotti, G., 2003, Episodic exhumation in the western Alps: Geology, v. 31, no. 7, p. 601–604, https://doi.org/10.1130/0091-7613(2003)031<0601:EEITWA>2.0.CO;2.

Carrasco-Núñez, G., Bernal, J.P., Dávila, P., Jicha, B., Giordano, G., and Hernández, J., 2018, Reappraisal on the onset of Los Humeros volcanic complex, revealed by new U/Th zircon and $^{40}Ar/^{39}Ar$ dating: Implications for greater geothermal potential: Geochemistry, Geophysics, Geosystems, v. 19, p. 132–149, https://doi.org/10.1002/2017GC007044.

Cassata, W.S., and Borg, L.E., 2016, A new approach to cosmogenic corrections in $^{40}Ar/^{39}Ar$ chronometry: Implications for the ages of Martian meteorites: Geochimica et Cosmochimica Acta, v. 187, p. 279–293, https://doi.org/10.1016/j.gca.2016.04.045.

Cassata, W.S., and Renne, P.R., 2013, Systematic variations of argon diffusion in feldspars and implications for thermochronometry: Geochimica et Cosmochimica Acta, v. 112, p. 251–287, https://doi.org/10.1016/j.gca.2013.02.030.

Cassata, W.S., Shuster, D.L., Renne, P.R., and Weiss, B.P., 2010, Evidence for shock heating and constraints on Martian surface temperatures revealed by $^{40}Ar/^{39}Ar$ thermochronometry of Martian meteorites: Geochimica et Cosmochimica Acta, v. 74, p. 6900–6920, https://doi.org/10.1016/j.gca.2010.08.027.

Cassata, W.S., Renne, P.R., and Shuster, D.L., 2011, Argon diffusion in pyroxenes: Implications for thermochronometry and mantle degassing: Earth and Planetary Science Letters, v. 304, no. 3, p. 407–416, https://doi.org/10.1016/j.epsl.2011.02.019.

Cerling, T.E., Brown, F.H., and Bowman, J.R., 1985, Low-temperature alteration of volcanic glass: Hydration, Na, K, ^{18}O and Ar mobility: Chemical Geology–Isotope Geoscience Section, v. 52, no. 3–4, p. 281–293, https://doi.org/10.1016/0168-9622(85)90040-5.

Chan, Y.-C., Crespi, J.M., and Hodges, K.V., 2000, Dating cleavage formation in slates and phyllites with the $^{40}Ar/^{39}Ar$ laser microprobe; an example from the western New England Appalachians, USA: Terra Nova, v. 12, p. 264–271, https://doi.org/10.1046/j.1365-3121.2000.00308.x.

Chen, Y., Smith, P., Evensen, N., York, D., and Lajoie, K., 1996, The edge of time: Dating young volcanic ash layers with the 40Ar-39Ar laser probe: Science, v. 274, no. 5290, p. 1176–1178, https://doi.org/10.1126/science.274.5290.1176.

Chetel, L.M., Janecke, S.U., Carroll, A.R., Beard, B.L., Johnson, C.M., and Singer, B.S., 2011, Paleogeographic reconstruction of the Eocene Idaho River, North American Cordillera: Geological Society of America Bulletin, v. 123, no. 1–2, p. 71–88, https://doi.org/10.1130/B30213.1.

Clauer, N., Zwingmann, H., Liewig, N., and Wendling, R., 2012, Comparative 40Ar/ 39Ar and K-Ar dating of illite-type clay minerals: A tentative explanation for age identities and differences: Earth-Science Reviews, v. 115, p. 76–96, https://doi.org/10.1016/j.earscirev.2012.07.003.

Clauer, N., 2013, The K-Ar and $^{40}Ar/^{39}Ar$ methods revisited for dating fine-grained K-bearing clay minerals: Chemical Geology, v. 354, p. 163–185, https://doi.org/10.1016/j.chemgeo.2013.05.030.

Coble, M.A., Grove, M., and Calvert, A.T., 2011, Calibration of Nu-Instruments Noblesse multicollector mass spectrometers for argon isotopic measurements using a newly developed reference gas: Chemical Geology, v. 290, p. 75–87, https://doi.org/10.1016/j.chemgeo.2011.09.003.

Condon, D.J., Hodges, K.V., Alsop, G.I., and White, A., 2006, Laser ablation $^{40}Ar/^{39}Ar$ dating of metamorphic fabrics in the Caledonides of north Ireland: Journal of the Geological Society [London], v. 163, p. 337–345, https://doi.org/10.1144/0016-764904-066.

Cook, C.P., Hill, D.J., Flierdt, T., Williams, T., Hemming, S.R., Dolan, A.M., Pierce, E.L., Escutia, C., Harwood, D., Cortese, G., and Gonzales, J.J., 2014, Sea surface temperature control on the distribution of far-traveled Southern Ocean ice-rafted detritus during the Pliocene: Paleoceanography, v. 29, p. 533–548, https://doi.org/10.1002/2014PA002625.

Cook, C.P., Hemming, S.R., van de Flierdt, T., Pierce Davis, E.L., Williams, T., Galindo, A.L., Jiménez-Espejo, F.J., and Escutia, C., 2017, Glacial erosion of East Antarctica in the Pliocene: A comparative study of multiple marine sediment provenance tracers: Chemical Geology, v. 466, p. 199–218, https://doi.org/10.1016/j.chemgeo.2017.06.011.

Copeland, P., and Harrison, T.M., 1990, Episodic rapid uplift in the Himalaya revealed by $^{40}Ar/^{39}Ar$ analysis of detrital K-feldspar and muscovite, Bengal Fan: Geology, v. 18, p. 354–357, https://doi.org/10.1130/0091-7613(1990)018<0354:ERUITH>2.3.CO;2.

Cosca, M., Stunitz, H., Bourgeix, A.L., and Lee, J.P., 2011, $^{40}Ar^*$ loss in experimentally deformed muscovite and biotite with implications for $^{40}Ar/^{39}Ar$ geochronology of naturally deformed rocks: Geochimica et Cosmochimica Acta, v. 75, no. 24, p. 7759–7778, https://doi.org/10.1016/j.gca.2011.10.012.

Cosca, M.A., Caby, R., and Bussy, F., 2005, Geochemistry and $^{40}Ar/^{39}Ar$ geochronology of pseudotachylyte associated with UHP white schists from the Dora Maira massif, Italy: Tectonophysics, v. 402, p. 93–110, https://doi.org/10.1016/j.tecto.2004.12.033.

Coutts, D.S., Matthews, W.A., and Hubbard, S.M., 2019, Assessment of widely used methods to derive depositional ages from detrital zircon populations: Geoscience Frontiers, v. 10, p. 1421–1435, https://doi.org/10.1016/j.gsf.2018.11.002.

Crank, J., 1975, The Mathematics of Diffusion: London, Oxford University Press, 414 p.

Dalrymple, G.B., 1979, Critical tables for conversion of K-Ar ages from old to new constants: Geology, v. 7, no. 11, p. 558–560, https://doi.org/10.1130/0091-7613(1979)7<558:CTFCOK>2.0.CO;2.

Dalrymple, G.B., Alexander, E.C., Lanphere, M.A., and Kraker, G.P., 1981, Irradiation of Samples for $^{40}Ar/^{39}Ar$ Dating Using the Geological Survey TRIGA Reactor: U.S. Geological Survey Professional Paper 1176, 55 p.

Davids, C., Benowitz, J.A., Layer, P.W., and Bergh, S.G., 2018, Direct $^{40}Ar/^{39}Ar$ K-feldspar dating of Late Permian–Early Triassic brittle faulting in northern Norway: Terra Nova, v. 30, no. 4, p. 263–269, https://doi.org/10.1111/ter.12333.

Deino, A., and Potts, R., 1990, Single-crystal $^{40}Ar/^{39}Ar$ dating of the Olorgesailie Formation, southern Kenya Rift: Journal of Geophysical Research–Solid Earth, v. 95, no. B6, p. 8453–8470, https://doi.org/10.1029/JB095iB06p08453.

Dodson, M.H., 1973, Closure temperature in cooling geochronological and petrological systems: Contributions to Mineralogy and Petrology, v. 40, p. 259–274, https://doi.org/10.1007/BF00373790.

Dodson, M.H., 1979, Theory of cooling ages, *in* Jäger, E., and Hunziker, J.C., eds., Lectures in Isotope Geology: Berlin, Springer-Verlag, p. 194–202.

Dodson, M.H., 1986, Closure profiles in cooling systems: Materials Science Forum, v. 7, p. 145–154.

Dutton, A., Rubin, K., Mclean, N., Bowring, J., Bard, E., Edwards, R.L., Henderson, G.M., Reid, M.R., Richards, D.A., Sims, K.W.W., Walker, J.D., and Yokoyama, Y., 2017, Data reporting standards for publication of U-series data for geochronology and timescale assessment in the earth sciences: Quaternary Geochronology, v. 39, p. 142–149, https://doi.org/10.1016/j.quageo.2017.03.001.

Eberhardt, P., Geiss, J., Graf, H., Grögler, N., Krähenbühl, U., Schwaller, H., Schwarzmüller, J., and Stettler, A., 1970, Trapped solar wind noble gases, exposure age and K/Ar-age in Apollo 11 lunar fine material, *in* Levinson, A.A., ed., Proceedings of the Apollo 11 Lunar Science Conference, Volume 2: Chemical and Isotope Analyses: New York, Pergamon Press, p. 1037–1070.

Ellis, B.S., Mark, D.F., Troch, J., Bachmann, O., Guillong, M., Kent, A.J.R., and von Quadt, A., 2017, Split-grain $^{40}Ar/^{39}Ar$ dating: Integrating temporal and geochemical data from crystal cargoes: Chemical Geology, v. 457, p. 15–23, https://doi.org/10.1016/j.chemgeo.2017.03.005.

Fechtig, H., and Kalbitzer, S., 1966, The diffusion of argon in potassium-bearing solids, *in* Schaeffer, O., and Zähringer, J., eds., Potassium-Argon Dating: New York, Springer-Verlag, p. 68–107.

Fleck, R.J., Sutter, J.F., and Elliot, D.H., 1977, Interpretation of discordant $^{40}Ar/^{39}Ar$ age-spectra of Mesozoic tholeiites from Antarctica: Geochimica et Cosmochimica Acta, v. 41, p. 15–32, https://doi.org/10.1016/0016-7037(77)90184-3.

Fleck, R.J., Hagstrum, J.T., Calvert, A.T., Evarts, R.C., and Conrey, R.M., 2014, $^{40}Ar/^{39}Ar$ geochronology, paleomagnetism, and evolution of the Boring volcanic field, Oregon and Washington, USA: Geosphere, v. 10, no. 6, p. 1283–1314, https://doi.org/10.1130/GES00985.1.

Fleck, R.J., Calvert, A.T., Coble, M.A., Wooden, J.L., Hodges, K., Hayden, L.A., van Soest, M.C., du Bray, E.A., and John, D.A., 2019, Characterization of the rhyolite of Bodie Hills and $^{40}Ar/^{39}Ar$ intercalibration with Ar mineral standards: Chemical Geology, v. 525, p. 282–302, https://doi.org/10.1016/j.chemgeo.2019.07.022.

Flude, S., Halton, A.M., Kelley, S.P., Sherlock, S.C., Schwanethal, J., and Wilkinson, C.M., 2014, Observation of centimetre-scale argon diffusion in alkali feldspars: Implications for $^{40}Ar/^{39}Ar$ thermochronology, *in* Jourdan, F., Mark, D.F., and Verati, C., eds., Advances in $^{40}Ar/^{39}Ar$ Dating: From Archaeology to Planetary Science: Geological Society [London] Special Publication 378, p. 265–275, https://doi.org/10.1144/SP378.25.

Foland, K.A., 1994, Argon diffusion in feldspars, *in* Parsons, I., ed., Feldspars and their Reactions: Amsterdam, Netherlands, Kluwer Academic, p. 415–447.

Foland, K.A., Hubacher, F.A., and Arehart, G.B., 1992, $^{40}Ar/^{39}Ar$ dating of very fine-grained samples—An encapsulated-vial procedure to overcome the problem of ^{39}Ar recoil loss: Chemical Geology, v. 102, p. 269–276, https://doi.org/10.1016/0009-2541(92)90161-W.

Fornash, K.F., Cosca, M.A., and Whitney, D.L., 2016, Tracking the timing of subduction and exhumation using $^{40}Ar/^{39}Ar$ phengite ages in blueschist- and eclogite-facies rocks (Sivrihisar, Turkey): Contributions to Mineralogy and Petrology, v. 171, no. 7, p. 67, https://doi.org/10.1007/s00410-016-1268-2.

Gaber, L.J., Foland, K.A., and Corbató, C.E., 1988, On the significance of argon release from biotite and amphibole during $^{40}Ar/^{39}Ar$ vacuum heating: Geochimica et Cosmochimica Acta, v. 52, p. 2457–2465, https://doi.org/10.1016/0016-7037(88)90304-3.

Gansecki, C.A., Mahood, G.A., and McWilliams, M.O., 1996, $^{40}Ar/^{39}Ar$ geochronology of rhyolites erupted following collapse of the Yellowstone caldera, Yellowstone Plateau volcanic field: Implications for crustal contamination: Earth and Planetary Science Letters, v. 142, p. 91–107, https://doi.org/10.1016/0012-821x(96)00088-x.

Garner, E.L., Murphy, T.J., Gramlich, J.W., Paulsen, P.J., and Barnes, I.L., 1975, Absolute isotopic abundance ratios and the atomic weight of a reference sample of potassium: Journal of Research of the National Bureau of Standards, v. 79A, no. 6, p. 713–725.

Gemignani, L., Kuiper, K.F., Wijbrans, J.R., Sun, X., and Santato, A., 2019, Improving the precision of single grain mica $^{40}Ar/^{39}Ar$ dating on smaller and younger muscovite grains: Application to provenance studies: Chemical Geology, v. 511, p. 100–111, https://doi.org/10.1016/j.chemgeo.2019.02.013.

Giletti, B.J., 1974, Studies in diffusion I: Argon in phlogopite mica, *in* Hofmann, A.W., Giletti, B.J., Yoder, H.S., and Yund, R.A., eds., Geochemical Transport and Kinetics: Washington, D.C., Carnegie Institute of Washington, p. 107–115.

Gradstein, F.M, Ogg, J.G., Schmitz, M.D., and Ogg, G.M., 2020, The Geologic Time Scale 2020: Amsterdam, Netherlands, Elsevier, 1300 p.

Grove, M., and Harrison, T.M., 1996, $^{40}Ar^*$ diffusion in Ferich biotite: American Mineralogist, v. 81, p. 940–951.

Gunther, D., Frischknecht, R., Heinrich, C.A., and Kahlert, H.J., 1997, Capabilities of an argon fluoride 193 nm excimer laser for laser ablation inductively coupled plasma mass spectrometry microanalysis of geological materials: Journal of Analytical Atomic Spectrometry, v. 12, no. 9, p. 939–944, https://doi.org/10.1039/A701423F.

Haines, S.H., and van der Pluijm, B.A., 2008, Clay quantification and Ar-Ar dating of synthetic and natural gouge—Application to the Miocene Sierra Mazatán detachment fault, Sonora, Mexico: Journal of Structural Geology, v. 30, p. 525–538, https://doi.org/10.1016/j.jsg.2007.11.012.

Hall, C.M., 2014, Direct measurement of recoil effects on $^{40}Ar/^{39}Ar$ standards, *in* Jourdan, F., Mark, D.F., and Verati, C., eds., Advances in $^{40}Ar/^{39}Ar$ Dating: From Archaeology to Planetary Sciences: Geological Society [London] Special Publication 378, 53 p, http://dx.doi.org/10.1144/SP378.7.

Hall, C.M., Higueras, P., Kesler, S.E., Lunar, R., Dong, H., and Halliday, A.N., 1997, Dating of alteration episodes related to mercury mineralization in the Almadén district, Spain: Earth and Planetary Science Letters, v. 148, p. 287–298, https://doi.org/10.1016/S0012-821X(97)00041-1.

Hall, C.M., Kesler, S.E., Simon, G., and Fortuna, J., 2000, Overlapping Cretaceous and Eocene alteration, Twin Creeks Carlin-type deposit, Nevada: Economic Geology, v. 95, p. 1739–1752, https://doi.org/10.2113/gsecongeo.95.8.1739.

Hames, W.E., and Hodges, K.V., 1993, Laser $^{40}Ar/^{39}Ar$ evaluation of slow cooling and episodic loss of ^{40}Ar from a sample of polymetamorphic muscovite: Science, v. 261, p. 1721–1723, https://doi.org/10.1126/science.261.5129.1721.

Harbi, H.M., Ali, K.A., McNaughton, N.J., and Andresen, A., 2018, U-Pb zircon and $^{40}Ar/^{39}Ar$ geochronology of sericite from hydrothermal alteration zones: New constraints for the timing of Ediacaran gold mineralization in the Sukhaybarat area, western Afif terrane, Saudi Arabia: Mineralium Deposita, v. 53, no. 4, p. 459–476, https://doi.org/10.1007/s00126-017-0751-7.

Harrison, T.M., 1981, Diffusion of ^{40}Ar in hornblende: Contributions to Mineralogy and Petrology, v. 78, p. 324–331, https://doi.org/10.1007/BF00398927.

Harrison, T.M., and Bé, K., 1983, $^{40}Ar/^{39}Ar$ age spectrum analysis of detrital microclines from the southern San Joaquin Basin, California: An approach to determining the thermal evolution of sedimentary basins: Earth and Planetary Science Letters, v. 64, p. 244–256, https://doi.org/10.1016/0012-821X(83)90207-8.

Harrison, T.M., and Lovera, O.M., 2014, The multi-diffusion domain model: Past, present, and future, *in* Jourdan, F., Mark, D.F., and Verati, C., eds., Advances in $^{40}Ar/^{39}Ar$ Dating: From Archaeology to Planetary Science, Geological Society [London] Special Publication 378, p. 91–106, https://doi.org/10.1144/SP378.9.

Harrison, T.M., Grove, M., Lovera, O.M., and Zeitler, P.K., 2005, Continuous thermal histories from inversion of closure profiles, *in* Reiners, P.W., and Ehlers, T.A., eds., Low-Temperature Thermochronology: Techniques, Interpretations, ad Applications: Washington, D.C., Mineralogical Society of America, Reviews in Mineralogy and Geochemistry 58, p. 389–409, https://doi.org/10.2138/rmg.2005.58.15.

Harrison, T.M., Celerier, J., Aikman, A.B., Hermann, J., and Heizler, M.T., 2009, Diffusion of ^{40}Ar in muscovite: Geochimica et Cosmochimica Acta, v. 73, no. 4, p. 1039–1051, https://doi.org/10.1016/j.gca.2008.09.038.

Heath, M., Phillips, D., and Matchan, E.L., 2018, An evidence-based approach to accurate interpretation of $^{40}Ar/^{39}Ar$ ages from basaltic rocks: Earth and Planetary Science Letters, v. 498, p. 65–76, https://doi.org/10.1016/j.epsl.2018.06.024.

Heaton, D.E., and Koppers, A.A.P., 2019, High-resolution $^{40}Ar/^{39}Ar$ geochronology of the Louisville Seamounts IODP Expedition 330 drill sites: Implications for the duration of hot spot–related volcanism and age progressions: Geochemistry, Geophysics, Geosystems, v. 20, p. 1–30, https://doi.org/10.1029/2018GC007759.

Heidorn, P.B., 2008, Shedding light on the dark data in the long tail of science: Library Trends, v. 57, no. 2, p. 280–299, https://doi.org/10.1353/lib.0.0036.

Heizler, M.T., and Harrison, T.M., 1988, Multiple trapped argon isotope components revealed by $^{40}Ar/^{39}Ar$ isochron analysis: Geochimica et Cosmochimica Acta, v. 52, p. 1295–1303, https://doi.org/10.1016/0016-7037(88)90283-9.

Heizler, M.T., and Harrison, T.M., 1991, The heating duration and provenance age of rocks in the Salton Sea geothermal field, southern California: Journal of Volcanology and Geothermal Research, v. 46, p. 73–97, https://doi.org/10.1016/0377-0273(91)90077-D.

Hemming, S.R., 2004, Heinrich events: Massive late Pleistocene detritus layers of the North Atlantic and their global climate imprint: Reviews of Geophysics, v. 42, RG1005, https://doi.org/10.1029/2003RG000128.

Hénocque, O., Ruffet, G., Colin, F., and Féraud, G., 1998, $^{40}Ar/^{39}Ar$ dating of West African lateritic cryptomelanes: Geochimica et Cosmochimica Acta, v. 62, p. 2739–2756, https://doi.org/10.1016/S0016-7037(98)00185-9.

Hereford, R., Beard, S.S., Dickinson, W.R., Karlstrom, K.E., Heizler, M.T., Crossey, L.J., Amoroso, L., House, K.K., and Pecha, M., 2016, Reevaluation of the Crooked Ridge River—Early Pleistocene (ca. 2 Ma) age and origin of the White Mesa alluvium, northeastern Arizona: Geosphere, v. 12, p. 768–789, https://doi.org/10.1130/GES01124.1.

Hess, J.C., and Lippolt, H.J., 1986, Kinetics of Ar isotopes during neutron irradiation: ^{39}Ar loss from minerals as a source of error in $^{40}Ar/^{39}Ar$ dating: Chemical Geology–Isotope Geoscience Section, v. 59, p. 223–236, https://doi.org/10.1016/0168-9622(86)90073-4.

Hodges, K.V., 2014, Thermochronology in orogenic systems, *in* Holland, H.D., and Turekian, K.K., eds., Treatise on Geochemistry, Volume 4: The Crust (2nd ed.): Oxford, UK, Elsevier, p. 281–308.

Hodges, K.V., and Bowring, S.A., 1995, $^{40}Ar/^{39}Ar$ thermochronology of isotopically zoned micas; insights from the southwestern USA Proterozoic orogen: Geochimica et Cosmochimica Acta, v. 59, no. 15, p. 3205–3220, https://doi.org/10.1016/0016-7037(95)00209-I.

Hodges, K.V., Hames, W.E., and Bowring, S.A., 1994, $^{40}Ar/^{39}Ar$ age gradients in micas from a high-temperature–low-pressure metamorphic terrain: Evidence for very slow cooling and implications for the interpretation of age spectra: Geology, v. 22, no. 1, p. 55–58, https://

doi.org/10.1130/0091-7613(1994)022<0055:AAAGIM>2.3.CO;2.

Horstwood, M.S.A., Košler, J., Gehrels, G., Jackson, S.E., Mclean, N.M., Paton, C., Pearson, N.J., Sircombe, K., Sylvester, P., Vermeesch, P., Bowring, J.F., Condon, D.J., and Schoene, B., 2016, Community-derived standards for LA-ICP-MS U-(Th-)Pb geochronology—Uncertainty propagation, age interpretation and data reporting: Geostandards and Geoanalytical Research, v. 40, p. 311–332, https://doi.org/10.1111/j.1751-908X.2016.00379.x.

Humayun, M., and Clayton, R.N., 1995, Precise determination of the isotopic composition of potassium: Application to terrestrial rocks and lunar soils: Geochimica et Cosmochimica Acta, v. 59, p. 2115–2130, https://doi.org/10.1016/0016-7037(95)00131-X.

Huneke, J.C., and Smith, S.P., 1976, The realities of recoil: ^{39}Ar recoil out of small grains and anomalous age patterns in ^{39}Ar-^{40}Ar dating: Lunar and Planetary Science Conference Proceedings, v. 7, p. 1987–2008.

Idleman, B.D., Zeitler, P.K., and McDannell, K.T., 2018, Characterization of helium release from apatite by continuous ramped heating: Chemical Geology, v. 476, p. 223–232, https://doi.org/10.1016/j.chemgeo.2017.11.019.

Ireland, T.R., 2013, Recent developments in isotope-ratio mass spectrometry for geochemistry and cosmochemistry: Review of Scientific Instruments, v. 84, 011101, https://doi.org/10.1063/1.4765055.

Jackson, C.R.M., Parman, S.W., Kelley, S.P., and Cooper, R.F., 2015, Light noble gas dissolution into ring structure–bearing materials and lattice influences on noble gas recycling: Geochimica et Cosmochimica Acta, v. 159, p. 1–15, https://doi.org/10.1016/j.gca.2015.02.036.

Janak, M., Plasienka, D., Frey, M., Cosca, M., Schmidt, S.T., Luptak, B., and Meres, S., 2001, Cretaceous evolution of a metamorphic core complex, the Veporic unit, Western Carpathians (Slovakia): P-T conditions and in situ ^{40}Ar/^{39}Ar UV laser probe dating of metapelites: Journal of Metamorphic Geology, v. 19, no. 2, p. 197–216, https://doi.org/10.1046/j.0263-4929.2000.00304.x.

Jicha, B.R., Singer, B.S., and Sobol, P., 2016, Re-evaluation of the ages of ^{40}Ar/^{39}Ar sanidine standards and supereruptions in the western U.S. using a Noblesse multi-collector mass spectrometer: Chemical Geology, v. 431, p. 54–66, https://doi.org/10.1016/j.chemgeo.2016.03.024.

Jourdan, F., and Renne, P.R., 2007, Age calibration of the Fish Canyon sanidine ^{40}Ar/^{39}Ar dating standard using primary K-Ar standards: Geochimica et Cosmochimica Acta, v. 71, p. 387–402, https://doi.org/10.1016/j.gca.2006.09.002.

Jourdan, F., Féraud, G., Bertrand, H., Kampunzu, A.B., Tshoso, G., Le Gall, B., Tiercelin, J.J., and Capiez, P., 2004, The Karoo triple junction questioned: Evidence from Jurassic and Proterozoic ^{40}Ar/^{39}Ar ages and geochemistry of the giant Okavango dyke swarm (Botswana): Earth and Planetary Science Letters, v. 222, p. 989–1006, https://doi.org/10.1016/j.epsl.2004.03.017.

Jourdan, F., Mark, D.F., and Verati, C., eds., 2014, Advances in ^{40}Ar/^{39}Ar Dating: From Archeology to Planetary Science: Geological Society [London] Special Publication 378.

Karlstrom, K.E., Crossey, L.J., Embid, E., Crow, R., Heizler, M., Hereford, R., Beard, L.S., Ricketts, J.W., Cather, S., and Kelley, S., 2017, Cenozoic incision history of the Little Colorado River: Its role in carving Grand Canyon and onset of rapid incision in the past ca. 2 Ma in the Colorado River system: Geosphere, v. 13, p. 49–81, https://doi.org/10.1130/GES01304.1.

Kelley, S.P., 2002a, K-Ar and Ar-Ar dating: Reviews in Mineralogy and Geochemistry, v. 47, p. 785–818, https://doi.org/10.2138/rmg.2002.47.17.

Kelley, S.P., 2002b, Excess argon in K-Ar and Ar-Ar geochronology: Chemical Geology, v. 188, p. 1–22, https://doi.org/10.1016/S0009-2541(02)00064-5.

Kelley, S.P., and Bluck, B.J., 1992, Laser ^{40}Ar-^{39}Ar ages for individual detrital muscovites in the Southern Uplands of Scotland, UK: Chemical Geology–Isotope Geoscience Section, v. 101, p. 143–156, https://doi.org/10.1016/0009-2541(92)90211-M.

Kelley, S.P., and Turner, G., 1991, Laser probe ^{40}Ar-^{39}Ar measurements of loss profiles within individual hornblende grains from the Giants Range granite, northern Minnesota, USA: Earth and Planetary Science Letters, v. 107, p. 634–648, https://doi.org/10.1016/0012-821X(91)90108-T.

Kelley, S.P., and Wartho, J.-A., 2000, Rapid kimberlite ascent and the significance of Ar-Ar ages in xenolith phlogopites: Science, v. 289, p. 609–611, https://doi.org/10.1126/science.289.5479.609.

Kelley, S.P., Arnaud, N.O., and Turner, S.P., 1994, High spatial resolution ^{40}Ar/^{39}Ar investigations using an ultraviolet laser probe extraction technique: Geochimica et Cosmochimica Acta, v. 58, p. 3519–3525, https://doi.org/10.1016/0016-7037(94)90103-1.

Kohn, M.J., Engi, M., and Lanari, P., 2017, Petrochronology: Methods and Applications, Mineralogical Society of America Reviews in Mineralogy and Geochemistry 83, 575 p.

Konrad, K., Koppers, A.A.P., Balbas, A.M., Miggins, D.P., and Heaton, D.E., 2019, Dating clinopyroxene phenocrysts in submarine basalts using ^{40}Ar/^{39}Ar geochronology: Geochemistry, Geophysics, Geosystems, v. 20, p. 1041–1053, https://doi.org/10.1029/2018GC007697.

Koppers, A.A.P., 2002, ArArCALC—Software for ^{40}Ar/^{39}Ar age calculations: Computers & Geosciences, v. 28, no. 5, p. 605–619, https://doi.org/10.1016/S0098-3004(01)00095-4.

Koppers, A.A.P., Staudigel, H., and Wijbrans, J.R., 2000, Dating crystalline groundmass separates of altered Cretaceous seamount basalts by the ^{40}Ar/^{39}Ar incremental heating technique: Chemical Geology, v. 166, p. 139–158, https://doi.org/10.1016/S0009-2541(99)00188-6.

Kramar, N., Cosca, M.A., and Hunziker, J.C., 2001, Heterogeneous ^{40}Ar* distributions in naturally deformed muscovite: In situ UV-laser ablation evidence for micro structurally controlled intragrain diffusion: Earth and Planetary Science Letters, v. 192, no. 3, p. 377–388, https://doi.org/10.1016/S0012-821X(01)00456-3.

Krantz, J.A., Parman, S.W., and Kelley, S.P., 2019, Recycling of heavy noble gases by subduction of serpentinite: Earth and Planetary Science Letters, v. 521, p. 120–127, https://doi.org/10.1016/j.epsl.2019.06.007.

Kuiper, K.F., Deino, A., Hilgen, F.J., Krijgsman, W., Renne, P.R., and Wijbrans, J.R., 2008, Synchronizing rock clocks of Earth history: Science, v. 320, p. 500–504, https://doi.org/10.1126/science.1154339.

Kula, J., and Baldwin, S.L., 2011, Jarosite, argon diffusion, and dating aqueous mineralization on Earth and Mars: Earth and Planetary Science Letters, v. 310, p. 314–318, https://doi.org/10.1016/j.epsl.2011.08.006.

Kula, J., and Spell, T.L., 2012, Recovery of muscovite age gradients by Ar-40/Ar-39 vacuum furnace step-heating analysis: Chemical Geology, v. 304, p. 166–174, https://doi.org/10.1016/j.chemgeo.2012.02.013.

Kylander-Clark, A.R.C., Hacker, B.R., and Cottle, J.M., 2013, Laser-ablation split-stream ICP petrochronology: Chemical Geology, v. 345, p. 99–112, https://doi.org/10.1016/j.chemgeo.2013.02.019.

Landis, G., Snee, L., and Juliani, C., 2005, Evaluation of argon ages and integrity of fluid-inclusion compositions: Stepwise noble gas heating experiments on 1.87 Ga alunite from Tapajós province, Brazil: Chemical Geology, v. 215, p. 127–153, https://doi.org/10.1016/j.chemgeo.2004.06.036.

Lanphere, M.A., and Dalrymple, G.B., 1976, Identification of excess ^{40}Ar by the ^{40}Ar/^{39}Ar age spectrum technique: Earth and Planetary Science Letters, v. 32, p. 141–148, https://doi.org/10.1016/0012-821X(76)90052-2.

Lee, J.K.W., 1995, Multipath diffusion in geochronology: Contributions to Mineralogy and Petrology, v. 120, p. 60–82, https://doi.org/10.1007/BF00311008.

Lee, J.K.W., Onstott, T.C., Cashman, K.V., Cumbest, R.J., and Johnson, D., 1991, Incremental heating of hornblende in vacuo: Implications for ^{40}Ar/^{39}Ar geochronology and the interpretation of thermal histories: Geology, v. 19, p. 872–876, https://doi.org/10.1130/0091-7613(1991)019<0872:IHOHIV>2.3.CO;2.

Lee, J.-Y., Marti, K., Severinghaus, J.P., Kawamura, K., Yoo, H.-S., Lee, J.B., and Kim, J.S., 2006, A redetermination of the isotopic abundances of atmospheric Ar: Geochimica et Cosmochimica Acta, v. 70, p. 4507–4512, https://doi.org/10.1016/j.gca.2006.06.1563.4.1.

Leslie, C., Peppe, D., Williamson, T., Bilardello, D., Heizler, M., Secord, R., and Leggett, T., 2018a, High-resolution magnetostratigraphy of the upper Nacimiento formation, San Juan Basin, New Mexico, USA: Implications for basin evolution and mammalian turnover: American Journal of Science, v. 318, p. 300–334, https://doi.org/10.2475/03.2018.02.

Leslie, C.E., Peppe, D.J., Williamson, T.E., Heizler, M., Jackson, M., Atchley, S.C., Nordt, L., and Standhardt, B., 2018b, Revised age constraints for Late Cretaceous to early Paleocene terrestrial strata from the Dawson Creek section, Big Bend National Park, west Texas: Geological Society of America Bulletin, v. 130, p. 1143–1163, https://doi.org/10.1130/B31785.1.

Li, S., Li, W., Beard, B.L., Raymo, M.E., Wang, X., Chen, Y., and Chen, J., 2019, K isotopes as a tracer for continental weathering and geological K cycling: Proceedings of the National Academy of Sciences of the United States of America, v. 116, p. 8740–8745, https://doi.org/10.1073/pnas.1811282116.

Licht, K.J., and Hemming, S.R., 2017, Analysis of Antarctic glacigenic sediment provenance through geochemical and petrologic applications: Quaternary Science Reviews, v. 164, p. 1–24, https://doi.org/10.1016/j.quascirev.2017.03.009.

Long, S.P., Heizler, M.T., Thomson, S.N., Reiners, P.W., and Fryxell, J.E., 2018, Rapid Oligocene to early Miocene extension along the Grant Range detachment system, Nevada, USA: Insights from multipart cooling histories of footwall rocks: Tectonics, v. 37, p. 4752–4779, https://doi.org/10.1029/2018TC005073.

Lovera, O.M., Richter, F.M., and Harrison, T.M., 1989, ^{40}Ar/^{39}Ar geochronometry for slowly cooled samples having a distribution of diffusion domain size: Journal of Geophysical Research, v. 94, p. 17917–17936, https://doi.org/10.1029/JB094iB12p17917.

Lovera, O.M., Richter, F.M., and Harrison, T.M., 1991, Diffusion domains determined by ^{39}Ar released during step heating: Journal of Geophysical Research, v. 96, p. 2057–2069, https://doi.org/10.1029/90JB02217.

Lovera, O.M., Heizler, M.T., and Harrison, T.M., 1993, Argon diffusion domains in K-feldspar II: Kinetic properties of MH-10: Contributions to Mineralogy and Petrology, v. 113, p. 381–393, https://doi.org/10.1007/BF00286929.

Lovera, O.M., Grove, M., and Harrison, T.M., 2002, Systematic analysis of K-feldspar ^{40}Ar/^{39}Ar step heating results II: Relevance of laboratory argon diffusion properties to nature: Geochimica et Cosmochimica Acta, v. 66, p. 1237–1255, https://doi.org/10.1016/S0016-7037(01)00846-8.

Mahon, K.I., 1996, The new "York" regression: Application of an improved statistical method in geochemistry: International Geology Review, v. 38, p. 293–303, https://doi.org/10.1080/00206819709465336.

Mark, D.F., Barfod, D., Stuart, F.M., and Imlach, J., 2009, The ARGUS multicollector noble gas mass spectrometer: Performance for ^{40}Ar/^{39}Ar geochronology: Geochemistry, Geophysics, Geosystems, v. 10, p. 1–9, https://doi.org/10.1029/2009GC002643.

Mark, D.F., Stuart, F.M., and de Podesta, M., 2011, New high-precision measurements of the isotopic composition of atmospheric argon: Geochimica et Cosmochimica Acta, v. 75, p. 7494–7501, https://doi.org/10.1016/j.gca.2011.09.042.

Mark, D.F., Renne, P.R., Dymock, R., Smith, V.C., Simon, J.I., Morgan, L.E., Staff, R.A., and Ellis, B.S., 2017, High-precision ^{40}Ar/^{39}Ar dating of Pleistocene tuffs and temporal anchoring of the Matuyama-Brunhes boundary: Quaternary Geochronology, v. 39, p. 1–23, https://doi.org/10.1016/j.quageo.2017.01.002.

Marra, F., Costantini, L., Di Buduo, G.M., Florindo, F., Jicha, B.R., Monaco, L., Palladino, D.M., and Sottili, G., 2019, Combined glacio-eustatic forcing and volcanotectonic uplift: Geomorphological and geochronological constraints on the Tiber River terraces in the eastern Vulsini Volcanic District (central Italy): Global and Planetary Change, v. 182, p. 103009, https://doi.org/10.1016/j.gloplacha.2019.103009.

Matchan, E.L., and Phillips, D., 2014, High precision multi-collector ^{40}Ar/^{39}Ar dating of young basalts: Mount Rouse volcano (SE Australia) revisited: Qua-

ternary Geochronology, v. 22, p. 57–64, https://doi.org/10.1016/j.quageo.2014.02.005.

Matchan, E.L., Phillips, D., Traine, E., and Zhu, D., 2018, $^{40}Ar/^{39}Ar$ ages of alkali feldspar xenocrysts constrain the timing of intraplate basaltic volcanism: Quaternary Geochronology, v. 47, p. 14–28, https://doi.org/10.1016/j.quageo.2018.04.009.

Matchan, E.L., Honda, M., and Kuiper, K.F., 2020, Corrigendum to "Astronomical calibration of $^{40}Ar/^{39}Ar$ reference minerals using high precision, multi-collector (ARGUSVI) mass spectrometry" [Geochim. Cosmochim. Acta 196 (2017) 351–369]: Geochimica et Cosmochimica Acta, v. 273, p. 406–410, https://doi.org/10.1016/j.gca.2020.01.040.

Matsumoto, A., and Kobayashi, T., 1995, KAr age determination of late Quaternary volcanic rocks using the "mass fractionation correction procedure": Application to the Younger Ontake Volcano, central Japan: Chemical Geology, v. 125, p. 123–135, https://doi.org/10.1016/0009-2541(95)00062-Q.

McDannell, K.T., Schneider, D.A., Zeitler, P.K., O'Sullivan, P.B., and Issler, D.R., 2019, Reconstructing deep-time histories from integrated thermochronology: An example from southern Baffin Island, Canada: Terra Nova, v. 31, no. 3, p. 189–204, https://doi.org/10.1111/ter.12386.

McDonald, C.S., Warren, C.J., Mark, D.F., Halton, A.M., Kelley, S.P., and Sherlock, S.C., 2016, Argon redistribution during a metamorphic cycle: Consequences for determining cooling rates: Chemical Geology, v. 443, p. 182–197, https://doi.org/10.1016/j.chemgeo.2016.09.028.

McDonald, C.S., Regis, D., Warren, C.J., Kelley, S.P., and Sherlock, S.C., 2018, Recycling argon through metamorphic reactions: The record in symplectites: Lithos, v. 300, p. 200–211, https://doi.org/10.1016/j.lithos.2017.11.028.

McDougall, I., and Harrison, T.M., 1999, Geochronology and Thermochronology by the $^{40}Ar/^{39}Ar$ Method (2nd ed.): New York, Oxford University Press, 269 p.

McIntyre, G.A., Brooks, C., Compston, W., and Turek, A., 1966, The statistical assessment of Rb-Sr isochrons: Journal of Geophysical Research, v. 71, p. 5459–5468, https://doi.org/10.1029/JZ071i022p05459.

Megrue, G.H., 1973, Spatial distribution of $^{40}Ar/^{39}Ar$ ages in Lunar Breccia 14301: Journal of Geophysical Research, v. 78, p. 3216–3221, https://doi.org/10.1029/JB078i017p03216.

Mercer, C.M., and Hodges, K.V., 2016, ArAR—A software tool to promote the robust comparison of K-Ar and $^{40}Ar/^{39}Ar$ dates published using different decay, isotopic, and monitor-age parameters: Chemical Geology, v. 440, p. 148–163, https://doi.org/10.1016/j.chemgeo.2016.06.020.

Mercer, C.M., Young, K.E., Weirich, J.R., Hodges, K.V., Jolliff, B.L., Wartho, J.-A., and van Soest, M.C., 2015, Refining lunar impact chronology through high spatial resolution $^{40}Ar/^{39}Ar$ dating of impact melts: Science Advances, v. 1, no. 1, p. e1400050, https://doi.org/10.1126/sciadv.1400050.

Mercer, C.M., Hodges, K.V., Jolliff, B.L., van Soest, M.C., Wartho, J.-A., and Weirich, J.R., 2019, Exploring the variability of argon loss in Apollo 17 impact melt rock 77135 using high spatial resolution $^{40}Ar/^{39}Ar$ geochronology: Meteoritics & Planetary Science, v. 54, no. 4, p. 721–739, https://doi.org/10.1111/maps.13240.

Merrihue, C.M., 1965, Trace-element determinations and potassium-argon dating by mass spectroscopy of neutron-irradiated samples: Transactions of the American Geophysical Union, v. 46, p. 125.

Merrihue, C.M., and Turner, G., 1966, Potassium-argon dating by activation with fast neutrons: Journal of Geophysical Research, v. 71, p. 2852–2857, https://doi.org/10.1029/JZ071i011p02852.

Min, K., Mundil, R., Renne, P.R., and Ludwig, K.R., 2000, A test for systematic errors in $^{40}Ar/^{39}Ar$ geochronology through comparison with U/Pb analysis of a 1.1-Ga rhyolite: Geochimica et Cosmochimica Acta, v. 64, p. 73–98, https://doi.org/10.1016/S0016-7037(99)00204-5.

Morgan, L.E., Renne, P.R., Taylor, R.E., and WoldeGabriel, G., 2009, Archaeological age constraints from extrusion ages of obsidian: Examples from the Middle Awash, Ethiopia: Quaternary Geochronology, v. 4, p. 193–203, https://doi.org/10.1016/j.quageo.2009.01.001.

Morgan, L.E., Santiago Ramos, D.P., Davidheiser-Kroll, B., Faithfull, J., Lloyd, N.S., Ellam, R.M., and Higgins, J.A., 2018, High-precision $^{41}K/^{39}K$ measurements by MC-ICP-MS indicate terrestrial variability of $\delta^{41}K$: Journal of Analytical Atomic Spectrometry, v. 33, p. 175–186, https://doi.org/10.1039/c7ja00257b.

Mulch, A., and Cosca, M. A., 2004, Recrystallization or cooling ages: In situ UV-laser $^{40}Ar/^{39}Ar$ geochronology of muscovite in mylonitic rocks: Journal of the Geological Society [London], v. 161, p. 573–582, https://doi.org/10.1144/0016-764903-110.

Mulch, A., Cosca, M.A., and Handy, M.R., 2002, In-situ UV-laser $^{40}Ar/^{39}Ar$ geochronology of a micaceous mylonite: An example of defect-enhanced argon loss: Contributions to Mineralogy and Petrology, v. 142, no. 6, p. 738–752, https://doi.org/10.1007/s00410-001-0325-6.

Mulch, A., Cosca, M.A., Andresen, A., and Fiebig, J., 2005, Time scales of deformation and exhumation in extensional detachment systems determined by high-spatial resolution in situ UV-laser $^{40}Ar/^{39}Ar$ dating: Earth and Planetary Science Letters, v. 233, no. 3–4, p. 375–390, https://doi.org/10.1016/j.epsl.2005.01.042.

Mulder, J.A., Karlstrom, K.E., Fletcher, K., Heizler, M.T., Timmons, J.M., Crossey, L.J., Gehrels, G.E., and Pecha, M., 2017, The syn-orogenic sedimentary record of the Grenville orogeny in southwest Laurentia: Precambrian Research, v. 294, p. 33–52, https://doi.org/10.1016/j.precamres.2017.03.006.

Muller, W., Kelley, S.P., and Villa, I.M., 2002, Dating fault-generated pseudotachylytes: Comparison of $^{40}Ar/^{39}Ar$ stepwise-heating, laser-ablation and Rb-Sr microsampling analyses: Contributions to Mineralogy and Petrology, v. 144, no. 1, p. 57–77, https://doi.org/10.1007/s00410-002-0381-6.

Najman, Y.M.R., Mark, C., Barfod, D., Carter, A., Parrish, R., Chew, D., and Gemignani, L., 2019, Spatial and temporal trends in exhumation of the Eastern Himalaya and syntaxis as determined from a multi-technique detrital thermochronological study of the Bengal Fan: Geological Society of America Bulletin, v. 131, no. 9–10, p. 1607–1622, https://doi.org/10.1130/B35031.1.

Nature, 2019, Announcement: FAIR data in Earth science: Nature, v. 565, p. 134, https://doi.org/10.1038/d41586-019-00075-3.

Naumenko-Dèzes, M.O., Nägler, T.F., Mezger, K., and Villa, I.M., 2017, Constraining the ^{40}K decay constant with ^{87}Rb-^{87}Sr–^{40}K-^{40}Ca chronometer intercomparison: Geochimica et Cosmochimica Acta, v. 220, p. 235–247, https://doi.org/10.1016/j.gca.2017.09.041.

Nelson, B., 2009, Data sharing: Empty archives: Nature, v. 461, no. 7261, p. 160–163. https://doi.org/10.1038/461160a.

Nier, A.O., 1950, A redetermination of the relative abundances of the isotopes of carbon, nitrogen, oxygen, argon, and potassium: Physical Review, v. 77, no. 6, p. 789–793, https://doi.org/10.1103/PhysRev.77.789.

Niespolo, E.M., Rutte, D., Deino, A.L., and Renne, P.R., 2017, Intercalibration and age of the Alder Creek sanidine $^{40}Ar/^{39}Ar$ standard: Quaternary Geochronology, v. 39, p. 205–213, https://doi.org/10.1016/j.quageo.2016.09.004.

Onstott, T.C., Miller, M.L., Ewing, R.C., Arnold, G.W., and Walsh, D.S., 1995, Recoil refinements: Implications for the $^{40}Ar/^{39}Ar$ dating technique: Geochimica et Cosmochimica Acta, v. 59, p. 1821–1834, https://doi.org/10.1016/0016-7037(95)00085-E.

Parsons, I., Brown, W.L., and Smith, J.V., 1999, $^{40}Ar/^{39}Ar$ thermochronology using alkali feldspars: Real thermal history or mathematical mirage of microtexture?: Contributions to Mineralogy and Petrology, v. 136, no. 1–2, p. 92–110, https://doi.org/10.1007/s004100050526.

Peters, S.E., Husson, J.M., and Czaplewski, J., 2018, Macrostrat: A platform for geological data integration and deep-time earth crust research: Geochemistry, Geophysics, Geosystems, v. 19, no. 4, p. 1393–1409, https://doi.org/10.1029/2018GC007467.

Phillips, D., and Onstott, T.C., 1988, Argon isotopic zoning in mantle phlogopite: Geology, v. 16, p. 542–546, https://doi.org/10.1130/0091-7613(1988)016<0542:AIZIMP>2.3.CO;2.

Phillips, D., and Matchan, E.L., 2013, Ultra-high precision $^{40}Ar/^{39}Ar$ ages for Fish Canyon Tuff and Alder Creek Rhyolite sanidine: New dating standards required?: Geochimica et Cosmochimica Acta, v. 121, p. 229–239, https://doi.org/10.1016/j.gca.2013.07.003.

Phillips, D., Matchan, E.L., Honda, M., and Kuiper, K.F., 2017, Astronomical calibration of $^{40}Ar/^{39}Ar$ reference minerals using high-precision, multi-collector (ARGUSVI) mass spectrometry: Geochimica et Cosmochimica Acta, v. 196, p. 351–369, https://doi.org/10.1016/j.gca.2016.09.027.

Phillips, D., Matchan, E.L., Honda, M., and Kuiper, K.F., 2020, Corrigendum to "Astronomical calibration of 40Ar/39Ar reference minerals using high precision, multi-collector (ARGUSVI) mass spectrometry" (Geochimica et Cosmochimica Acta [2017] 196 [351–369], [S0016703716305427], [10.1016/j.gca.2016.09.027]): Geochimica et Cosmochimica Acta, v. 273, p. 406–410, https://doi.org/10.1016/j.gca.2020.01.040.

Pickles, C.S., Kelley, S.P., Reddy, S.M., and Wheeler, J., 1997, Determination of high spatial resolution argon isotope variations in metamorphic biotites: Geochimica et Cosmochimica Acta, v. 61, no. 18, p. 3809–3833, https://doi.org/10.1016/S0016-7037(97)00289-5.

Pierce, E.L., Williams, T., Van De Fliert, T., Hemming, S.R., Goldstein, S.L., and Brachfeld, S.A., 2011, Characterizing the sediment provenance of East Antarctica's weak underbelly: The Aurora and Wilkes sub-glacial basins: Paleoceanography, v. 26, PA4217, https://doi.org/10.1029/2011PA002127.

Pierce, E.L., Hemming, S.R., Williams, T., van de Fliert, T., Thomson, S.N., Reiners, P.W., Gehrels, G.E., Brachfeld, S.A., and Goldstein, S.L., 2014, A comparison of detrital U-Pb zircon, $^{40}Ar/^{39}Ar$ hornblende, $^{40}Ar/^{39}Ar$ biotite ages in marine sediments off East Antarctica: Implications for the geology of subglacial terrains and provenance studies: Earth-Science Reviews, v. 138, p. 156–178, https://doi.org/10.1016/j.earscirev.2014.08.010.

Polyak V.J., McIntosh, W.C., Guven, N., and Provencio, P., 1998, Age and origin of Carlsbad cavern and related caves from $^{40}Ar/^{39}Ar$ of alunite: Science, v. 279, p. 1919–1922, https://doi.org/10.1126/science.279.5358.1919.

Putlitz, B., Cosca, M.A., and Schumacher, J.C., 2005, Prograde mica $^{40}Ar/^{39}Ar$ growth ages recorded in high pressure rocks (Syros, Cyclades, Greece): Chemical Geology, v. 214, no. 1–2, p. 79–98, https://doi.org/10.1016/j.chemgeo.2004.08.056.

Quinn, D.P., Schaen, A.J., Sundell, K.E., Gehrels, G., Goring, S., Marcott, S., Meyers, S.R., Peters, S.E., Ross, J., Schmitz, M.D., Singer, B.S., and Williams, J.W., 2019, Sparrow: A data management system and cyberinfrastructure component targeted at geochronology laboratories Paper No. 79-5: Geological Society of America Abstracts with Programs, v. 51, no. 5, https://doi.org/10.1130/abs/2019AM-340223.

Reiners, P.W., and Brandon, M.T., 2006, Using thermochronology to understand orogenic erosion: Annual Review of Earth and Planetary Sciences, v. 34, p. 419–466, https://doi.org/10.1146/annurev.earth.34.031405.125202.

Reiners, P.W., Carlson, R.W., Renne, P.R., Cooper, K.M., Granger, D.E., McLean, N.M., and Schoene, B., 2018, Geochronology and Thermochronology: Hoboken, New Jersey, John Wiley & Sons, 464 p.

Ren, Z., and Vasconcelos, P.M., 2019a, Argon diffusion in hypogene and supergene alunites: Implications to geochronology and thermochronometry on Earth and Mars: Geochimica et Cosmochimica Acta, v. 262, p. 166–187, https://doi.org/10.1016/j.gca.2019.07.014.

Ren, Z., and Vasconcelos, P.M., 2019b, Quantifying ^{39}Ar recoil in natural hypogene and supergene alunites and jarosites: Geochimica Cosmochimica et Acta, v. 260, p. 84–98, https://doi.org/10.1016/j.gca.2019.06.019.

Renne, P.R., and Norman, E.B., 2001, Determination of the half-life of ^{37}Ar by mass spectrometry: Physical Review C, v. 63, no. 4, p. 047302, https://doi.org/10.1103/PhysRevC.63.047302.

Renne, P.R., Becker, T.A., and Swapp, S.M., 1990, $^{40}Ar/^{39}Ar$ laser-probe dating of detrital micas from the Montgomery Creek Formation: Clues

to provenance, tectonics, and weathering processes: Geology, v. 18, p. 563–566, https://doi.org/10.1130/0091-7613(1990)018<0563:AALPDO>2.3.CO;2.

Renne, P.R., Swisher, C.C., Deino, A.L., Karner, D.B., Owens, T.L., and Depaolo, D.J., 1998, Intercalibration of standards, absolute ages and uncertainties in $^{40}Ar/^{39}Ar$ dating: Chemical Geology, v. 145, p. 117–152, https://doi.org/10.1016/S0009-2541(97)00159-9.

Renne, P.R., Deino, A.L., Hames, W.E., Heizler, M.T., Hemming, S.R., Hodges, K.V., Koppers, A.P., Mark, D.F., Morgan, L.E., Phillips, D., Singer, B.S., Turrin, B.D., Villa, I.M., Villeneuve, M., and Wijbrans, J.R., 2009, Data reporting norms for $^{40}Ar/^{39}Ar$ geochronology: Quaternary Geochronology, v. 4, p. 346–352, https://doi.org/10.1016/j.quageo.2009.06.005.

Renne, P.R., Mundil, R., Balco, G., Min, K., and Ludwig, K.R., 2010, Joint determination of ^{40}K decay constants and $^{40}Ar^*/^{40}K$ for the Fish Canyon sanidine standard, and improved accuracy for $^{40}Ar/^{39}Ar$ geochronology: Geochimica et Cosmochimica Acta, v. 74, no. 18, p. 5349–5367, https://doi.org/10.1016/j.gca.2010.06.017.

Renne, P.R., Balco, G., Ludwig, K.R., Mundil, R., and Min, K., 2011, Response to the comment by W.H. Schwarz et al. on "Joint determination of ^{40}K decay constants and $^{40}Ar^*/^{40}K$ for the Fish Canyon sanidine standard, and improved accuracy for $^{40}Ar/^{39}Ar$ geochronology" by P. R. Renne et al., 2010: Geochimica et Cosmochimica Acta, v. 75, no. 17, p. 5097–5100, https://doi.org/10.1016/j.gca.2011.06.021.

Renne, P.R., Mulcahy, S.R., Cassata, W.S., Morgan, L.E., Kelley, S.P., Hlusko, L.J., and Njau, J.K., 2012, Retention of inherited Ar by alkali feldspar xenocrysts in a magma: Kinetic constraints from Ba zoning profiles: Geochimica et Cosmochimica Acta, v. 93, p. 129–142, https://doi.org/10.1016/j.gca.2012.06.029.

Renne, P.R., Deino, A.L., Hilgen, F.J., Kuiper, K.F., Mark, D.F., Mitchell, W.S., Morgan, L.E., Mundil, R., and Smit, J., 2013, Time scales of critical events around the Cretaceous-Paleogene boundary: Science, v. 339, p. 684–687, https://doi.org/10.1126/science.1230492.

Reynolds, R., Jr., and Reynolds, R., III, 1996, NEWMOD-for-Windows: The Calculation of One-Dimensional X-ray Diffraction Patterns for Mixed-Layered Clay Minerals: Hanover, New Hampshire.

Rivera, T.A., Storey, M., Zeeden, C., Hilgen, F.J., and Kuiper, K., 2011, A refined astronomically calibrated $^{40}Ar/^{39}Ar$ age for Fish Canyon sanidine: Earth and Planetary Science Letters, v. 311, no. 3–4, p. 420–426, http://doi.org/10.1016/j.epsl.2011.09.017.

Rivera, T.A., Storey, M., Schmitz, M.D., and Crowley, J.L., 2013, Age intercalibration of $^{40}Ar/^{39}Ar$ sanidine and chemically distinct U/Pb zircon populations from the Alder Creek Rhyolite Quaternary geochronology standard: Chemical Geology, v. 345(C), p. 87–98, http://doi.org/10.1016/j.chemgeo.2013.02.021.

Rivera, T.A., Schmitz, M.D., Jicha, B.R., and Crowley, J.L., 2016, Zircon petrochronology and $^{40}Ar/^{39}Ar$ sanidine dates for the Mesa Falls Tuff: Crystal-scale records of magmatic evolution and the short lifespan of a large Yellowstone magma chamber: Journal of Petrology, v. 57, p. 1677–1704, https://doi.org/10.1093/petrology/egw053.

Rivera, T.A., Furlong, R., Vincent, J., Gardiner, S., Jicha, B.R., Schmitz, M.D., and Lippert, P.C., 2018, Volcanism at 1.45 Ma within the Yellowstone volcanic field, United States: Journal of Volcanology and Geothermal Research, v. 357, p. 224–238, https://doi.org/10.1016/j.jvolgeores.2018.04.030.

Rose, J., and Koppers, A.A.P., 2019, Simplifying age progressions within the Cook-Austral Islands using ARGUS-VI high-resolution $^{40}Ar/^{39}Ar$ incremental heating ages: Geochemistry, Geophysics, Geosystems, v. 20, p. 4756–4778, https://doi.org/10.1029/2019GC008302.

Ross, J., 2019, NMGRL/pychron v18.2: Zenodo, https://doi.org/10.5281/zenodo.3237834.

Roy, M., van de Flierdt, T., Hemming, S.R., and Goldstein, S.L., 2007, $^{40}Ar/^{39}Ar$ ages of hornblende grains and bulk Sm/Nd isotopes of circum-Antarctic glacio-marine sediments: Implications for sediment provenance in the southern ocean: Chemical Geology, v. 244, p. 507–519, https://doi.org/10.1016/j.chemgeo.2007.07.017.

Rutte, D., Pfänder, J.A., Koleška, M., Jonckheere, R., and Unterricker, S., 2015, Radial fast-neutron fluence gradients during rotating $^{40}Ar/^{39}Ar$ sample irradiation recorded with metallic fluence monitors and geological age standards: Geochemistry, Geophysics, Geosystems, v. 16, p. 336–345, https://doi.org/10.1002/2014GC005611.

Rutte D., Renne, P.R., Morrell, J., Qui, L., Ayllon, M., van Bibber, K., Wilson, J., Becker, T.A., Batchelder, J., Bersntein, L.A., Lebois, M., James, J., Chong, S.-A., Heriot, W.L., Wallace, M., Marcial, A., Johnson, C., Woolley, G., and Adams, P.A., 2019, Boutique neutrons advance $^{40}Ar/^{39}Ar$ geochronology: Science Advances, v. 5, no. 9, p. eaaw5526, https://doi.org/10.1126/sciadv.aaw5526.

Schaen, A.J., Jicha, B.R., Kay, S.M., Singer, B.S., and Tibbetts, A., 2016, Eocene to Pleistocene magmatic evolution of the Delarof Islands, Aleutian Arc: Geochemistry, Geophysics, Geosystems, v. 17, p. 1086–1108, https://doi.org/10.1002/2015GC005918.

Schaen, A.J., Cottle, J.M., Singer, B.S., Keller, C.B., and Garibaldi, N., 2017, Complementary crystal accumulation and rhyolite melt segregation in a late Miocene Andean pluton: Geology, v. 45, p. 835–838, https://doi.org/10.1130/G39167.1.

Schaen, A.J., Singer, B.S., Cottle, J.M., Garibaldi, N., Schoene, B., Satkoski, A.M., and Fournelle, J., 2018, Textural and mineralogical record of low pressure melt extraction and silicic cumulate formation in the late Miocene Risco Bayo–Huemul plutonic complex, southern Andes: Journal of Petrology, v. 59, p. 1991–2016, https://doi.org/10.1093/petrology/egy087.

Schmitz, M.D., 2012, Radiogenic isotope geochronology, *in* Gradstein, F.M., Ogg, J.G., Schmitz, M.D., and Ogg, G.M., The Geologic Time Scale 2012: Boston, Massachusetts, Elsevier, p. 115–126, https://doi.org/10.1016/B978-0-444-59425-9.00006-8.

Schoene, B., Latkoczy, C., Schaltegger, U., and Günther, D., 2010, A new method integrating high-precision U-Pb geochronology with zircon trace element analysis (U-Pb TIMS-TEA): Geochimica et Cosmochimica Acta, v. 74, no. 24, p. 7144–7159, https://doi.org/10.1016/j.gca.2010.09.016.

Sharp, W.D., and Renne, P.R., 2005, The $^{40}Ar/^{39}Ar$ dating of core recovered by the Hawaii Scientific Drilling Project (phase 2), Hilo, Hawaii: Geochemistry, Geophysics, Geosystems, v. 6, Q04G17, https://doi.org/10.1029/2004GC000846.

Sherlock, S.C., Kelley, S.P., Zalasiewicz, J.A., Schofield, D.I., Evans, J.A., Merriman, R.J., and Kemp, S.J., 2003, Precise dating of low-temperature deformation: Strain-fringe analysis by Ar-40-Ar-39 laser microprobe: Geology, v. 31, no. 3, p. 219–222, https://doi.org/10.1130/0091-7613(2003)031<0219:PDOLTD>2.0.CO;2.

Sherlock, S.C., Lucks, T., Kelley, S.P., and Barnicoat, A., 2005, A high resolution record of multiple diagenetic events: Ultraviolet laser microprobe Ar/Ar analysis of zoned K-feldspar overgrowths: Earth and Planetary Science Letters, v. 238, no. 3–4, p. 329–341, https://doi.org/10.1016/j.epsl.2005.07.018.

Singer, B.S., and Pringle, M.S., 1996, Age and duration of the Matuyama-Brunhes geomagnetic polarity reversal from $^{40}Ar^{39}Ar$ incremental heating analyses of lavas: Earth and Planetary Science Letters, v. 139, no. 1–2, p. 47–61, https://doi.org/10.1016/0012-821X(96)00003-9.

Singer, B.S., Wijbrans, J.R., Nelson, S.T., Pringle, M.S., Feeley, T.C., and Dungan, M.A., 1998, Inherited argon in a Pleistocene andesite lava: $^{40}Ar/^{39}Ar$ incremental-heating and laser-fusion analyses of plagioclase: Geology, v. 26, p. 427–430, https://doi.org/10.1130/0091-7613(1998)026<0427:IAIAPA>2.3.CO;2.

Singer, B.S., Jicha, B.R., Mochizuki, N., and Coe, R.S., 2019, Synchronizing volcanic, sedimentary, and ice core records of Earth's last magnetic polarity reversal: Science Advances, v. 5, no. 8, p. eaaw4621, https://doi.org/10.1126/sciadv.aaw4621.

Skipton, D.R., Schneider, D.A., Kellett, D.A., and Joyce, N.L., 2017, Deciphering the Paleoproterozoic cooling history of the northeastern Trans-Hudson orogen, Baffin Island (Canada), using $^{40}Ar/^{39}Ar$ step-heating and UV laser thermochronology: Lithos, v. 284, p. 69–90, https://doi.org/10.1016/j.lithos.2017.03.023.

Smith, P.E., Evensen, N.M., and York, D., 1993, First successful ^{40}Ar-^{39}Ar dating of glauconies: Argon recoil in single grains of cryptocrystalline material: Geology, v. 21, p. 41–44, https://doi.org/10.1130/0091-7613(1993)021<0041:FSAADO>2.3.CO;2.

Smith, S.R., Kelley, S.P., Tindle, A.G., and Breaks, F.W., 2005, Compositional controls on $^{40}Ar/^{39}Ar$ ages of zoned mica from a rare-element pegmatite: Contributions to Mineralogy and Petrology, v. 149, no. 5, p. 613–626, https://doi.org/10.1007/s00410-005-0674-7.

Sprain, C.J., Renne, P.R., Wilson, G.P., and Clemens, W.A., 2015, High-resolution chronostratigraphy of the terrestrial Cretaceous-Paleogene transition and recovery interval in the Hell Creek region, Montana: Geological Society of America Bulletin, v. 127, p. 393–409, https://doi.org/10.1130/B31076.1.

Sprain, C.J., Renne, P.R., Clemens, W.A., and Wilson, G.P., 2018, Calibration of chron C29r: New high-precision geochronologic and paleomagnetic constraints from the Hell Creek region, Montana: Geological Society of America Bulletin, v. 130, p. 1615–1644, https://doi.org/10.1130/B31890.1.

Środoń, J., 1980, Precise identification of illite/smectite interstratifications by X-ray powder diffraction: Clays and Clay Minerals, v. 28, p. 401–411, https://doi.org/10.1346/CCMN.1980.0280601.

Steiger, R.H., and Jäger, E., 1977, Subcommission on Geochronology: Convention on the use of decay constants in geo- and cosmochronology: Earth and Planetary Science Letters, v. 36, p. 359–362, https://doi.org/10.1016/0012-821X(77)90060-7.

Stelten, M.E., Cooper, K.M., Vazquez, J.A., Calvert, A.T., and Glessner, J.J.G., 2015, Mechanisms and timescales of generating eruptible rhyolitic magmas at Yellowstone caldera from zircon and sanidine geochronology and geochemistry: Journal of Petrology, v. 56, p. 1607–1642, https://doi.org/10.1093/petrology/egv047.

Stoenner, R., Schaffer, O., and Katcoff, S., 1965, Half-lives of Argon-37, Argon-39, and Argon-42: Science, v. 148, no. 3675, p. 1325–1328, https://doi.org/10.1126/science.148.3675.1325.

Swisher, C.C., III, Swisher, C.C., Grajales-Nishimura, J.M., Montanari, A., Margolis, S.V., Claeys, P., Alvarez, W., Renne, P., Cedillo-Pardo, E., Maurrasse, F.J-M.R., Curtis, G.H., Smit, J., and McWilliams, M.O., 1992, Coeval $^{40}Ar/^{39}Ar$ ages of 65.0 million years ago from Chicxulub crater melt rock and Cretaceous-Tertiary boundary tektites: Science, v. 257, p. 954–958, https://doi.org/10.1126/science.257.5072.954.

Swisher, C.C., III, Dingus, L., and Butler, R.F., 1993, $^{40}Ar/^{39}Ar$ dating and magnetostratigraphic correlation of the terrestrial Cretaceous-Paleogene boundary and Puercan Mammal Age, Hell Creek-Tullock formations, eastern Montana: Canadian Journal of Earth Sciences, v. 30, p. 1981–1996, https://doi.org/10.1139/e93-174.

Szulc, A., Najman, Y., Sinclair, H., Pringle, M., Bickle, M., Chapman, H., Garzanti, E., Ando, S., Huyghe, P., Mugnier, J., Ojha, T., and DeCelles, P., 2006, Tectonic evolution of the Himalaya constrained by detrital ^{40}Ar-^{39}Ar, Sm-Nd and petrographic data from the Siwalik foreland basin succession, SW Nepal: Basin Research, v. 18, no. 4, p. 375–391, https://doi.org/10.1111/j.1365-2117.2006.00307.x.

Ton-That, T., Singer, B., and Paterne, M., 2001, $^{40}Ar/^{39}Ar$ dating of latest Pleistocene (41 ka) marine tephra in the Mediterranean Sea: Implications for global climate records: Earth and Planetary Science Letters, v. 184, no. 3–4, p. 645–658, https://doi.org/10.1016/S0012-821X(00)00358-7.

Tuller-Ross, B., Savage, P.S., Chen, H., and Wang, K., 2019, Potassium isotope fractionation during magmatic differentiation of basalt to rhyolite: Chemical Geology, v. 525, p. 37–45, https://doi.org/10.1016/j.chemgeo.2019.07.017.

Turner, G., 1971, ^{40}Ar-^{39}Ar dating: The optimization of irradiation parameters: Earth and Planetary Science Letters, v. 10, p. 227–234, https://doi.org/10.1016/0012-821X(71)90010-0.

Turner, G., and Cadogan, P., 1974, Possible effects of ^{39}Ar recoil in $^{40}Ar/^{39}Ar$ dating: Proceedings of the Lunar and Planetary Science Conference, v. 5, p. 1601–1615.

Turrin, B.D., Swisher, C.C., III, and Deino, A.L., 2010, Mass discrimination monitoring and intercalibration of dual collectors in noble gas mass spectrometer systems: Geochemistry, Geophysics, Geosystems, v. 11, Q0AA09, https://doi.org/10.1029/2009GC003013.

Valkiers, S., Vendelbo, D., Berglund, M., and de Podesta, M., 2010, Preparation of argon primary measurement standards for the calibration of ion current ratios measured in argon: International Journal of Mass Spectrometry, v. 291, p. 41–47, https://doi.org/10.1016/j.ijms.2010.01.004.

van der Pluijm, B.A., and Hall, C.M, 2015, Fault zone (thermochronology), *in* Rink, J.W., and Thompson, J.W., eds., Encyclopedia of Scientific Dating Methods: Dordrecht, Netherlands, Springer, p. 269–273, https://doi.org/10.1007/978-94-007-6304-3.

van der Pluijm, B.A., Hall, C.M., Vrolijk, P.J., Pevear, D.R., and Covey, M.C., 2001, The dating of shallow faults in the Earth's crust: Nature, v. 412, p. 172–175, https://doi.org/10.1038/35084053.

van Soest, M.C., Monteleone, B.D., Hodges, K.V., and Boyce, J.W., 2011, Laser depth profiling studies of helium diffusion in Durango fluorapatite: Geochimica et Cosmochimica Acta, v. 75, p. 2409–2419, https://doi.org/10.1016/j.gca.2011.02.008.

Vasconcelos, P.M., 1999, K-Ar and $^{40}Ar/^{39}Ar$ geochronology of weathering processes: Annual Review of Earth and Planetary Sciences, v. 27, p. 183–229, https://doi.org/10.1146/annurev.earth.27.1.183.

Vasconcelos, P.M., Becker, T.A., Renne, P.R., and Brimhall, G.H., 1992, Age and duration of weathering by K-Ar and $^{40}Ar/^{39}Ar$ analysis of K-Mn oxides: Science, v. 258, p. 451–455, https://doi.org/10.1126/science.258.5081.451.

Vasconcelos, P.M., Renne, P.R., Becker, T.A., and Wenk, H.R., 1995, Mechanisms and kinetics of atmospheric, radiogenic, and nucleogenic argon release from cryptomelane during $^{40}Ar/^{39}Ar$ analysis: Geochimica et Cosmochimica Acta, v. 59, p. 2057–2070, https://doi.org/10.1016/0016-7037(95)00126-3.

Verati, C., and Jourdan, F., 2014, Modelling effect of sericitization of plagioclase on the $^{40}K/^{40}Ar$ and $^{40}Ar/^{39}Ar$ chronometers: Implication for dating basaltic rocks and mineral deposits, *in* Jourdan, F., Mark, D.F., and Verati, C., eds., Advances in $^{40}Ar/^{39}Ar$ Dating: From Archaeology to Planetary Sciences: Geological Society [London] Special Publication 378, p. 155–174, https://doi.org/10.1144/SP378.14.

Vermeesch, P., 2015, Revised error propagation of $^{40}Ar/^{39}Ar$ data, including covariances: Geochimica et Cosmochimica Acta, v. 171, p. 325–337, https://doi.org/10.1016/j.gca.2015.09.008.

Vermeesch, P., 2018, IsoplotR: A free and open toolbox for geochronology: Geoscience Frontiers, v. 9, p. 1479–1493, https://doi.org/10.1016/j.gsf.2018.04.001.

Villa, I.M., 2006, From nanometer to megameter: Isotopes, atomic-scale processes, and continent-scale tectonic models: Lithos, v. 87, no. 3–4, p. 155–173, https://doi.org/10.1016/j.lithos.2005.06.012.

Villa, I.M., and Hanchar, J.M., 2013, K-feldspar hygrochronology: Geochimica et Cosmochimica Acta, v. 101, p. 24–33, https://doi.org/10.1016/j.gca.2012.09.047.

Villa, I.M., Huneke, J.C., and Wasserburg, G.J., 1983, ^{39}Ar recoil losses and presolar ages in Allende inclusions: Earth and Planetary Science Letters, v. 63, p. 1–12, https://doi.org/10.1016/0012-821X(83)90017-1.

Vrolijk, P., and van der Pluijm, B.A., 1999, Clay gouge: Journal of Structural Geology, v. 21, p. 1039–1048, https://doi.org/10.1016/S0191-8141(99)00103-0.

Walk, C.J., Karlstrom, K.E., Crow, R.S., and Heizler, M.T., 2019, Birth and evolution of the Virgin River fluvial system: ~1 km of post–5 Ma uplift of the western Colorado Plateau: Geosphere, v. 15, p. 759–782, https://doi.org/10.1130/GES02019.1.

Walton, E.L., Kelley, S.P., and Spray, J.G., 2007, Shock implantation of Martian atmospheric argon in four basaltic shergottites: A laser probe Ar-40/Ar-39 investigation: Geochimica et Cosmochimica Acta, v. 71, no. 2, p. 497–520, https://doi.org/10.1016/j.gca.2006.09.004.

Wang, K., and Jacobsen, S.B., 2016, An estimate of the bulk silicate earth potassium isotopic composition based on MC-ICPMS measurements of basalts: Geochimica et Cosmochimica Acta, v. 178, p. 223–232, https://doi.org/10.1016/j.gca.2015.12.039.

Ware, B., and Jourdan, F., 2018, $^{40}Ar/^{39}Ar$ geochronology of terrestrial pyroxene: Geochimica et Cosmochimica Acta, v. 230, p. 112–136, https://doi.org/10.1016/j.gca.2018.04.002.

Warren, C.J., Sherlock, S.C., and Kelley, S.P., 2011, Interpreting high-pressure phengite $^{40}Ar/^{39}Ar$ laserprobe ages: An example from Saih Hatat, NE Oman: Contributions to Mineralogy and Petrology, v. 161, no. 6, p. 991–1009, https://doi.org/10.1007/s00410-010-0576-1.

Warren, C.J., Hanke, F., and Kelley, S.P., 2012a, When can muscovite $^{40}Ar/^{39}Ar$ dating constrain the timing of metamorphic exhumation?: Chemical Geology, v. 291, p. 79–86, https://doi.org/10.1016/j.chemgeo.2011.09.017.

Warren, C.J., Kelley, S.P., Sherlock, S.C., and McDonald, C.S., 2012b, Metamorphic rocks seek meaningful cooling rate: Interpreting $^{40}Ar/^{39}Ar$ ages in an exhumed ultra-high pressure terrane: Lithos, v. 155, p. 30–48, https://doi.org/10.1016/j.lithos.2012.08.011.

Wartho, J.-A., Kelley, S.P., Brooker, R.A., Carroll, M.R., Villa, I.M., and Lee, M.R., 1999, Direct measurement of Ar diffusion profiles in a gem-quality Madagascar K-feldspar using the ultra-violet laser ablation microprobe (UVLAMP): Earth and Planetary Science Letters, v. 170, p. 141–153, https://doi.org/10.1016/S0012-821X(99)00088-6.

Wasserstein, R.L., and Lazar, N.A., 2016, The ASA's statement on p-values: Context, process, and purpose: The American Statistician, v. 70, no. 2, p. 129–133, https://doi.org/10.1080/00031305.2016.1154108.

Wendt, I., and Carl, C., 1991, The statistical distribution of the mean squared weighted deviation: Chemical Geology–Isotope Geoscience Section, v. 86, p. 275–285, http://dx.doi.org/10.1016/0168-9622(91)90010-T.

Wilkinson, M.D., et al., 2016, The FAIR guiding principles for scientific data management and stewardship: Scientific Data, v. 3, p. 160018, https://doi.org/10.1038/sdata.2016.18.

Williams, T., van de Flierdt, T., Hemming, S.R., Chung, E., Roy, M., and Goldstein, S.L., 2010, Evidence for iceberg armadas from East Antarctica in the Southern Ocean during the late Miocene and early Pliocene: Earth and Planetary Science Letters, v. 290, p. 351–361, https://doi.org/10.1016/j.epsl.2009.12.031.

Xiao, M., Qiu, H.N., Jiang, Y.D., Cai, Y., Bai, X.J., Zhang, W.F., Liu, M., and Qin, C.J., 2019, Gas release systematics of mineral-hosted fluid inclusions during stepwise crushing: Implications for $^{40}Ar/^{39}Ar$ geochronology of hydrothermal fluids: Geochimica et Cosmochimica Acta, v. 251, p. 36–55, https://doi.org/10.1016/j.gca.2019.02.016.

Yan, Y., van der Pluijm, B.A., and Peacor, D.R., 2001, Deformation microfabrics of clay gouge, Lewis thrust, Canada: A case for fault weakening from clay transformation: Geological Society [London] Special Publication 186, p. 103–112, https://doi.org/10.1144/GSL.SP.2001.186.01.07.

Yancey, T.E., Heizler, M.T., Miller, B.V., and Guillemette, R.N., 2018, Eocene–Oligocene chronostratigraphy of ignimbrite flareup volcanic ash beds on the Gulf of Mexico coastal plains: Geosphere, v. 14, p. 1232–1252, https://doi.org/10.1130/GES01621.1.

Yaniv, A., and Heymann, D., 1972, Atmospheric Ar^{40} in lunar fines: Lunar and Planetary Science Conference Proceedings, v. 2, p. 1967–1990.

York, D., Hall, C.M., Yanase, Y., Hanes, J.A., and Kenyon, W.J., 1981, $^{40}Ar/^{39}Ar$ dating of terrestrial minerals with a continuous laser: Geophysical Research Letters, v. 8, p. 1136–1138, https://doi.org/10.1029/GL008i011p01136.

Yun, J.-B., Shi, H.-S., Zhu, J.-Z., Zhao, L.-H., and Qiu, H.-N., 2010, Dating petroleum emplacement by illite $^{40}Ar/^{39}Ar$ laser stepwise heating: American Association of Petroleum Geologists Bulletin, v. 94, p. 759–771, https://doi.org/ https://doi.org/10.1306/10210909102.

Zeitler, P.K., 1987, Argon diffusion in partially outgassed alkali feldspars: Insights from $^{40}Ar/^{39}Ar$ analysis: Chemical Geology–Isotope Geoscience Section, v. 65, p. 167–181, https://doi.org/10.1016/0168-9622(87)90071-6.

Zi, J., Jourdan, F., Wang, X.-C., Haines, P.W., Rasmussen, B., Halverson, G.P., and Sheppard, S., 2019, Pyroxene $^{40}Ar/^{39}Ar$ dating of basalt and applications to large igneous provinces and Precambrian stratigraphic correlations: Journal of Geophysical Research–Solid Earth, v. 124, no. 8, p. 8313–8330, https://doi.org/10.1029/2019JB017713.

Science Editor: Rob Strachan
Associate Editor: Michael Smith

Manuscript Received 17 November 2019
Revised Manuscript Received 23 March 2020
Manuscript Accepted 7 May 2020

Printed in the USA